



Universidade do Minho
Escola de Engenharia

Pedro André Gonçalves Morais

**Cardiac Motion and Deformation
estimation in tagged Magnetic
Resonance Imaging**

Dissertação de Mestrado
Mestrado em Engenharia Biomédica

Trabalho realizado sob a orientação de:
Professor Doutor Jaime Fonseca
Professor Doutor Jan D'hooge

Declaração

Nome: Pedro André Gonçalves Morais

Endereço electrónico: a57113@alunos.uminho.pt

Telefone: (+351) 916077002

Número do Cartão de Cidadão: 13715779

Título da dissertação:

Cardiac Motion and Deformation estimation in tagged Magnetic Resonance Imaging

Estudo do movimento e deformação cardíaca em imagens de ressonância magnética marcadas.

Orientadores:

Professor Doutor Jaime Francisco Cruz Fonseca

Professor Doutor Jan D'hooge

Ano de conclusão: 2013

Designação do Mestrado: Mestrado Integrado em Engenharia Biomédica

Área de Especialização: Electrónica Médica

Escola: de Engenharia

**É AUTORIZADA A REPRODUÇÃO PARCIAL DESTA TESE, APENAS
PARA EFEITOS DE INVESTIGAÇÃO, MEDIANTE DECLARAÇÃO
ESCRITA DO INTERESSADO, QUE A TAL SE COMPROMETE.**

Universidade do Minho, ____/____/____

Assinatura: _____

À Ana Silva, que te sirva de inspiração:
“Uma amizade pode ter vírgulas, nunca um ponto final.”

Acknowledgements/Agradecimentos

This master thesis symbolizes the end of a cycle, where important intellectual and life experiences contributed to the final definition of my own identity. After these 5 years, in the amazing city of Braga, together with wonderful persons that always helped me, I am ready to start a new journey with more experience and self-knowledge. Starting from today, I want to show the best of me, without the fears of the past.

First of all, I want to thank Professor Jan D'hooge, the promoter of the current thesis. All your interest during the last year was amazing, and your opinions during the meetings were essential to improve the final work. During the thesis, I always felt your support, even when I returned to Portugal. I expect to keep our collaborations in future works, and I expect in a future PhD project. I also want to thank Piet Claus for the collaboration in image analysis and support about the clinical relevance of the results.

I need to thank my daily supervisor, Brecht Heyde, for all the support, ideas, and discussions to improve the final work. The new proposed methodologies were impossible without your experience. You have helped me to grow in the area of imaging processing, where, in my opinion, you are a reference.

Ao professor Jaime Fonseca, tenho de agradecer pelo apoio que obtive para manter o projecto que iniciei em Leuven, assim como por todas as opiniões durante a elaboração do mesmo. Agradeço também pela total disponibilidade durante a tese.

Para o Daniel Barbosa, tenho de te agradecer por todas as reuniões, por todo o *feedback* que obtive e suporte na elaboração da tese. Eu também vejo em ti uma referência na área, um modelo a seguir. Tenho também de agradecer a ti e à Dalila Roupar, por todo o apoio extra tese, durante e após o *ERASMUS*.

Ao professor João Vilaça, tenho que agradecer pela oportunidade que me deu de entrar no mundo da investigação antes da minha tese. Agradeço por toda a colaboração durante a realização desta tese, por todas as discussões, formas de validação, métodos para apresentação dos temas da tese e por todo o equipamento que me disponibilizou.

Ao Sandro Queirós, tenho que agradecer por todo o acompanhamento na tese e pela amizade. Já trabalhamos juntos há muitos anos e espero continuar com esta ligação. As discussões que tivemos foram essenciais para desenvolver os métodos. Tenho também que agradecer aos restantes membros do gabinete: António Moreira, João Fonseca, João Spranger, Nuno Rodrigues, Mafalda Couto e Pedro Rodrigues.

Agradeço também à Teresa Pinto pelo suporte na escrita da tese em inglês e à professora Ana Cristina Braga pelo apoio na análise estatística.

Tenho também que agradecer a toda a minha família, aos meus pais José Morais e Joaquina Gonçalves, irmão Jorge Morais, cunhada Catarina Moreira, avós, tios, primos e padrinhos por todo o apoio. Vocês são as pessoas que sempre estiveram presentes e que sempre quiseram que eu alcançasse todas as metas que ia traçando, sem nunca desistir. Todos vocês foram essenciais durante a elaboração desta tese de mestrado. Quero também agradecer à minha família académica, família Teixeira, com particular ênfase ao meu “afilhado” João Meireles e “netos” Francisco Lobo, Márcia Costa e Vitor Faria. Vocês são uma fonte de orgulho e de motivação, espero que daqui a alguns anos esteja a assistir às vossas dissertações e que consigam muito mais do que eu. Eu acredito no vosso valor e vão ter sempre o meu apoio em tudo.

À Cristiana Fernandes tenho que agradecer por todo o apoio durante a escrita da tese, por me teres acompanhado nos momentos em que me senti mais frágil psicologicamente, por todas as opiniões e imparcialidade. Foste a pessoa que me ajudou a crescer dizendo para desistir de viver num mundo que não existe e deixar de pensar em tudo ao detalhe, seguindo em frente. Se eu acabei esta tese, foi tudo graças a ti.

À Ana Silva, penso que a dedicatória inicial diz tudo. Tu foste a pessoa que marcou a mudança em mim. Quando uma pessoa sente-se perdida e não sabe o que mais fazer, receber um apoio como tu fizeste, provocou uma mudança tão grande em mim. Passaram tantos anos, e mesmo assim tu foste capaz de me apoiar quando eu mais precisei. Estes últimos meses foram tão desgastantes, não só para mim mas também para ti, mas encontrei em ti a fonte de suporte e motivação que precisava para terminar tudo. Espero que em breve, também consiga ver-te a terminar tudo. Nunca desistas.

Por fim, existe um último agradecimento que quero fazer. Quero agradecer a quem me ajudou a elaborar todos os métodos e os vários resultados apresentados. Agradeço à pessoa que me dizia “*eu sei que vais conseguir, porque sei o enorme valor que tens*”. Todos os métodos aqui propostos não são só meus, mas também de quem me apoiou a este ponto. Todas as linhas presentes na tese foram feitas com o teu apoio. Um dia gostava de poder colocar aqui o teu nome, porque em parte, esta tese também é tua.

Thank you. Dank u wel. Obrigado a todos,

Pedro Morais

17/09/2013

Summary

Cardiovascular diseases are the main cause of death in Europe, with an estimate of 4.3 million deaths each year. The assessment of the regional wall deformation is a relevant clinical indicator, and can be used to detect several cardiac lesions. Nowadays, this study can be performed using several image modalities. In the current thesis, we focus on tagged Magnetic Resonance imaging (t-MRI) technique. Such technique allows acquiring images with tags on the myocardium, which deform with the muscle.

The present thesis intends to assess the left ventricle (LV) deformation using radial and circumferential strain. To compute such strain values, both endo- and epicardial contours of the LV are required.

As such, a new framework to automatically assess the LV function is proposed. This framework presents: (i) an automatic segmentation technique, based on a tag suppression strategy followed by an active contour segmentation method, and (ii) a tracking approach to extract myocardial deformation, based on a non-rigid registration method. The automatic segmentation uses the B-spline Explicit Active Surface framework, which was previously applied in ultra-sound and cine-MRI images. In both cases, a real-time and accurate contour was achieved. Regarding the registration step, starting from a state-of-art approach, termed sequential 2D, we suggest a new method (termed sequential 2D+t), where the temporal information is included on the model.

The tracking methods were first tested on synthetic data to study the registration parameters influence. Furthermore, the proposed and original methods were applied on porcine data with myocardial ischemia. Both methods were able to detect dysfunctional regions. A comparison between the strain curve in the sequential 2D and sequential 2D+t strategies was also shown. As conclusion, a smoothing effect in the strain curve was detected in the sequential 2D+t strategy. The validation of the segmentation approach uses a human dataset. A comparison between the manual contour and the proposed segmentation method results was performed. The results, suggest that proposed method has an acceptable performance, removing the tedious task related with manual segmentation and the intra-observer variability. Finally, a comparison between the proposed framework and the currently available commercial software was performed. The commercial software results were obtained from core-lab analysis. An acceptable result ($r = 0.601$) was achieved when comparing the strain peak values. Importantly, the proposed framework appears to present a more acceptable result.

Resumo

As doenças cardiovasculares são a principal causa de morte na Europa, com aproximadamente 4.7 milhões de mortes por ano. A avaliação da deformação do miocárdio a um nível local é um importante indicador clínico e pode ser usado para a detecção de lesões cardíacas. Este estudo é normalmente realizado usando várias modalidades de imagem médica. Nesta tese, a Resonância Magnética (RM) marcada foi a técnica selecionada. Estas imagens têm marcadores no músculo cardíaco, os quais se deformam com o miocárdio e podem ser usados para o estudo da deformação cardíaca.

Nesta tese, pretende-se estudar a deformação radial e circunferencial do ventrículo esquerdo (VE). Assim, um contorno do endo- e epicárdio no VE é essencial.

Desta forma, uma ferramenta para o estudo da deformação do VE foi desenvolvida. Esta possui: (i) um método de segmentação automático, usando uma estratégia de supressão dos marcadores, seguido de uma segmentação com um contorno ativo, e (ii) um método de *tracking* para determinação da deformação cardíaca, baseado em registo não rígido. A segmentação automática utiliza a ferramenta *B-spline Explicit Active Surface*, que foi previamente aplicada em imagens de ultrassons e cine-RM. Em ambos os casos, uma segmentação em tempo real e com elevada exatidão foi alcançada. Vários esquemas de registo foram apresentados. Neste ponto, começando com uma técnica do estado da arte (designada de sequencial 2D), uma nova metodologia foi proposta (sequencial 2D+t), onde a informação temporal é incorporada no modelo.

De forma a analisar a influência dos parâmetros do registo, estes foram estudados num *dataset* sintético. De seguida, os diferentes esquemas de registo foram testados num *dataset* suíno com isquemia. Ambos os métodos foram capazes de detetar as regiões disfuncionais. De igual forma, utilizando as curvas de deformação obtidas para cada um dos métodos propostos, foi possível observar uma suavização na direção temporal para o método sequencial 2D+t. Relativamente à segmentação, esta foi validada com um *dataset* humano. Um contorno manual foi comparado com o obtido pelo método proposto. Os resultados sugerem que a nova estratégia é aceitável, sendo mais rápida do que a realização de um contorno manual e eliminando a variabilidade entre observadores. Por fim, realizou-se uma comparação entre a ferramenta proposta e um *software* comercial (com análise de *core-lab*). A comparação entre os valores de pico da deformação exhibe uma correlação plausível ($r=0.601$). Contudo, é importante notar, que a nova ferramenta tende a apresentar um resultado mais aceitável.

Contents

Acknowledgements/Agradecimientos	v
Summary.....	vii
Resumo	ix
Abbreviations.....	xv
Figures list	xvii
Tables list.....	xxiv
1. Introduction.....	3
1.1. Cardiac anatomy and physiology.....	3
1.2. Cardiac motion.....	4
1.2.1. Cardiovascular diseases	4
1.2.2. Regional heart deformation.....	5
1.2.3. Tagged Magnetic Resonance Imaging	6
1.3. Medical Image Processing	10
1.3.1. Medical Image Segmentation.....	10
1.3.2. Medical Image Registration	12
1.4. Motivation.....	15
1.5. Aim	16
1.6. Thesis outline.....	17
2. LV tracking and segmentation in t-MRI images	21
2.1. LV tracking methods	21
2.2. LV segmentation methods	26
2.2.1. LV segmentation after un-tagging t-MRI images.....	26
2.2.2. LV segmentation on the original t-MRI image.....	29
2.3. Summary.....	30
3. Mathematical Background.....	33
3.1. Motion estimation: Non rigid image registration.....	33

3.1.1.	Transformation Model	33
3.1.2.	Cost function	35
3.1.3.	Similarity Metrics	35
3.1.4.	Regularization Term	39
3.1.5.	Optimization.....	39
3.1.6.	Image interpolators	40
3.1.7.	Traditional motion estimation scheme: sequential 2D FFD formulation	41
3.2.	Image Segmentation	42
3.2.1.	Active Contours	42
3.2.2.	B-spline Explicit Active Surfaces	44
3.3.	Improving the initialization: template matching.....	46
3.4.	Application: the BEAS threshold algorithm	47
3.5.	Evaluating image segmentation quality	48
3.6.	Strain estimation	49
4.	Methodology.....	55
4.1.	Overview.....	55
4.2.	Automatic myocardial segmentation	55
4.2.1.	Overview	55
4.2.2.	Automatic detection of the LV.....	57
4.2.3.	Image detagging	59
4.2.4.	Automatic Initialization	63
4.2.5.	Segmentation propagation.....	66
4.3.	Cardiac Motion estimation.....	67
4.3.1.	Sequential 2D+t FFD formulation	67
4.3.2.	Fixed 2D+t FFD formulation	69
4.4.	Strain estimation	70

4.4.1. Strain estimation in the sequential 2D+t and fixed 2D+t FFD formulation	70
4.4.2. Contours definition on the ED frame	70
5. Methods	75
5.1. Datasets	75
5.2. Experiments	77
5.2.1. Parameter tuning	77
5.2.2. Detection of (dys)functional regions.....	77
5.2.3. Validation of the (semi-) automatic segmentation approach	77
5.2.4. Validation of the proposed sequential 2D+t FFD formulation	78
5.2.5. Comparison of the proposed algorithm with a commercial state-of-the art solution	79
6. Results	83
6.1. Parameter tuning	83
6.2. Detection of (dys)functional regions	86
6.3. Validation of the (semi-) automatic segmentation approach	88
6.4. Validation of the proposed sequential 2D+t FFD formulation	89
6.5. Comparison of the proposed algorithm with a commercial state-of-the art solution	91
7. Discussion.....	99
7.1. Parameter tuning	99
7.2. Detection of (dys)functional regions	100
7.3. Validation of the (semi-) automatic segmentation approach	101
7.4. Validation of the proposed sequential 2D+t FFD formulation	102
7.5. Comparison of the proposed algorithm with a commercial state-of-the art solution	104
8. Conclusions and contributions.....	111
8.1 Conclusions.....	111

8.2 Contributions	112
9. References.....	117
10. Appendix I – Details about the automatic segmentation method.....	127
11. Appendix II – Number of correction in the automatic contour	129
12. Appendix III – LV tracking and segmentation results.....	130
13. Appendix IV – Validation of the proposed sequential 2D+t FFD formulation using a published result	132
14. Appendix V – Global strain curve obtained in proposed framework and in commercial software.....	133
15. Appendix VI – Results obtained in each slice for the proposed framework and commercial software.....	134
16. Appendix VII – Validation of the proposed framework using the commercial software results as ground truth.....	137
17. Appendix VIII – Details about the ANOVA table	139

Abbreviations

2D	two-dimensional
2D+t	two-dimensional plus time
3D	three-dimensional
4D	four-dimensional
APD	average perpendicular distance
BE	bending energy
BEAS	B-spline Explicit Active Surfaces
CHDs	Coronary Heart Diseases
CSPAMM	Complementary spatial modulization of magnetization
CT	Computed Tomography
CVDs	Cardiovascular Diseases
DANTE	Delays alternating with nutations for tailored excitations
DE-MRI	delay-enhancement Magnetic Resonance Imaging
DICOM	Digital Imaging and communication in Medicine
DOF	Degrees of freedom
ECG	electrocardiogram
ED	end-diastole
EES	Error at end-systole
ES	end-systole
FFD	free form deformation
FFT	Fast Fourier Transform
HARP	Harmonic phase
ITK	Insight Segmentation and Registration Toolkit
LA	long-axis
LBFGBS	limited memory Broyden Fletcher Goldforb Shannon
LOA	limits of agreement
LV	left ventricle
MR	Magnetic Resonance
MRI	Magnetic Resonance Imaging
MI	Mutual Information
MMI	Mattes Mutual Information
NMI	Normalized Mutual Information
NRR	Non-Rigid Registration
NURBS	NonUniform Rational B-splines
PCA	Principal Component Analysis
PET	Positron Emission Tomography
RF	Radio-frequency
RMSE	Root mean square error
ROI	region of interest
RV	right ventricle
SA	short-axis
SM	Similarity Metric
SNR	Signal Noise Ratio
SPAMM	Spatial modulization of magnetization

SPECT	Single Photon Emission Computed Tomography
SSD	sum of squared differences
SSFP	Steady-State Free Precession
t-MRI	tagged Magnetic Resonance Imaging
TPF	true positive fraction
US	ultrasound
VHDs	valvular heart diseases

Figures list

Figure 1.1 - The heart anatomy. Adapted from [6].	3
Figure 1.2 – Distribution of the blood output from the LV [2].	4
Figure 1.3 - Five t-MRI sequences.	7
Figure 1.4 - Schematic about the SPAMM tagging pulse methodology. Adapted from [26].	9
Figure 1.5 - Definition of the SA and LA views. Adapted from [28].	9
Figure 1.6 - 3D tagging structure visualized by isosurface rendering of the 3D dataset [29].	10
Figure 1.7 - 3D endocardium segmentation in echocardiography image [44].	11
Figure 1.8 – Registration problem. Searching for the best transformation (T) capable to map the moving image on the fixed image with minimum error.	12
Figure 1.9 - Registration problem scheme.	13
Figure 1.10 – Transformation models used by (a) rigid registration, (b) affine registration, and, (c) non-rigid registration [46].	13
Figure 1.11 - Example of thorax tumor staging from PET and CT [46].	14
Figure 1.12 - Example of fusion data from MR and CT by image registration. (left) MR overlaid on CT and (right) CT overlaid on MR [46].	14
Figure 1.13 - (a) Deaths by cause in Europe (b) Death rates from cardiovascular problem in each country of Europe [48].	15
Figure 2.1 - Block scheme of strain estimation using tracking landmarks.	22
Figure 2.2 - Block scheme of strain estimation using HARP.	23
Figure 2.3 - Block scheme of strain estimation using gabor filter bank.	23
Figure 2.4 - Block scheme of strain estimation using deformable models.	24
Figure 2.5 - Block scheme of strain estimation using optical flow methodology.	24
Figure 2.6 - Block scheme of strain estimation using non-rigid registration.	24
Figure 2.7 - Different registrations schemes: a) pairwise 2D [68], (b) fixed 2D+t alignment [70], (c) joint 2D+t alignment [10].	25
Figure 2.8 - Methods to segment t-MRI images.	26
Figure 2.9 - Block scheme for segmentation in t-MRI using the strategy proposed in [76].	27
Figure 2.10 - Block scheme for segmentation in t-MRI using the strategy proposed in [77].	28

Figure 2.11 - Block scheme for segmentation in t-MRI using the strategy proposed in [78].	28
Figure 2.12 - Block scheme for segmentation in t-MRI using the strategy proposed in [83].	29
Figure 2.13 - Block scheme for segmentation in t-MRI using the strategy proposed in [89].	29
Figure 2.14 - Block scheme for segmentation in t-MRI using the strategy proposed in [80].	30
Figure 2.15 - Block scheme for segmentation in t-MRI using the strategy proposed in [75].	30
Figure 3.1 - The basic components of the registration framework.	33
Figure 3.2- B-spline mesh overlaid over the reference image. The transformation parameters μ are only defined on the mesh knot κ [47].	34
Figure 3.3 - Conceptual representation of the multi-resolution registration process [85].	35
Figure 3.4 - Binary synthetic image. The black squares represent 0, and the white represent 1.	36
Figure 3.5 - Joint histogram used in a registration problem between a CT and MR example [87].	37
Figure 3.6 - Parzen Window (blue), constructed by superimposing kernel functions centered on the samples of the image [85].	38
Figure 3.7 - Regularization effect. (a) Normal registration result, (b) Non-physical deformation.	39
Figure 3.8 - Interpolators. a) Nearest neighbor, b) Linear, c) B-spline.	40
Figure 3.9 - Sequential 2D formulation [96].	41
Figure 3.10 - Active contours propagation. The dashed yellow line is the initialization.	42
Figure 3.11 - a) Gradient of the image used in edge based approach, b) Regional assessment of the intensity for the definition of the statistically model used in region based methods [97].	43
Figure 3.12 - Synthetic image presented in [97] . (a) initialization, (b) unsuccessful result of region-based segmentation, (c) successful result of edge-based segmentation technique [97].	44

Figure 3.13 - Template matching methodology proposed in [33]. (a) Creation of various kernels to use as templates, (b) optimization problem to detect the optimal template, (c) original image and optimal template, (d) original image and first estimation of the contours.	47
Figure 3.14 - Region growing based on BEAS framework. (a) Initialization of the algorithm using a pre-defined center position, (b) Contour evolution, (c) Optimal solution, where is possible to see a difference between the initial center position (blue point) and the new center position (green point), (d) optimal solution.	48
Figure 3.15 - Estimation of the radial and circumferential strain.....	50
Figure 3.16 - Displacement computation from the frame f to ED based on the optimal alignment.	50
Figure 3.17 - Strain of a one-dimensional object is limited to lengthening or shortening. Strain is the deformation of an object relative to its original shape [107].....	51
Figure 3.18 – Definition of the segments in the base, mid and apical slice [111].....	51
Figure 4.1 – Proposed automatic framework to study cardiac deformation. “T” means tracking.	55
Figure 4.2 - Scheme used for automatic segmentation of LV in t-MRI images.....	56
Figure 4.3 - Methodology used to determine the center of the myocardium.	57
Figure 4.4 - Definition of the LV, RV and septum after the binarization step.....	58
Figure 4.5 - (a) Binary image, (b) Virtual circle in some white points of (a), (c) result of the Hough transform method.....	59
Figure 4.6 - Method used to suppress the tags in the t-MRI images.	60
Figure 4.7 - Differences in spectrum between two t-MRI images with different tag orientations.	60
Figure 4.8 - Binary polar image used to define the cutoff frequency.....	61
Figure 4.9 - (a) - Low pass filter, (b) - Profile of low pass filter in the red line position.	61
Figure 4.10 - Peak filter design. (a) Detection of 8 candidates with restrictions in terms of distance, (b) the 8 candidates pixels (white points), the blue lines represent the method used to compute the difference to the center of the image (red point), c) The perfect square used in the method, (d) Filter design, application of a morphological dilate in (c) and convolution with a Gaussian filter, (e) Profile of the filter using as a reference the red line present in the figure (d).....	62
Figure 4.11 - 3D profile of the filter design to suppress the tags.	63

Figure 4.12 - Methodology used to automatically initialize the BEAS framework.	63
Figure 4.13 - Region growing based on BEAS framework. (a) Initialization of the algorithm, (b) Contour evolution, (c) Contour evolution with a result similar to the optimal solution, where is possible to see a difference between the initial center position (red point) and the new center position (green point), (d) optimal solution.....	64
Figure 4.14 - Estimation of the minimum radius. (a) Image in polar space, and (b) number of points from the myocardium in each line of the polar image.	65
Figure 4.15 – 3D methodology used to propagate the LV center position.....	66
Figure 4.16 - Schematic used for the proposed sequential 2D+t FFD.	67
Figure 4.17 - Schematic used for the fixed 2D+t FFD.	69
Figure 4.18 – Cumulating the displacement field in the proposed sequential 2D+t.	70
Figure 4.19 - Strategy used to pass the contours from the frame number 4 for the ED frame.....	71
Figure 5.1 - Synthetic images with (a) SNR = 18db and (b) SNR = 6dB [49].....	75
Figure 5.2 - Registration validation using t-MRI and DE-MRI images.....	76
Figure 5.3 - t-MRI acquired in two different centers.	76
Figure 5.4 - Interface developed for assess the automatic segmentation of the LV in t-MRI.....	78
Figure 6.1 - Influence of the ω_{BE} weight in image with SNR =18dB [49]. The vertical axis represents the error in pixels. The results with sequential 2D (red) and the proposed sequential 2D+t (blue) approaches are presented, in terms of RMSE (solid line) and EES (dashed line), using different metrics and different final grid spacing (FGS) values.	83
Figure 6.2 - Influence of the ω_{BE} weight in image with SNR =18dB [49] using 4 scales. The vertical axis represents the error in pixels. The results with sequential 2D (red) and the proposed sequential 2D+t (blue) approaches are presented, in terms of RMSE (solid line) and EES (dashed line), using different metrics and different final grid spacing (FGS) values.....	84
Figure 6.3 - Influence of the ω_{BE} weight in image with SNR =18dB [49] using 64 bins to compute the joint histogram. The vertical axis represents the error in pixels. The results with sequential 2D (red) and the proposed sequential 2D+t (blue) approaches are presented, in terms of RMSE (solid line) and EES (dashed line), using different metrics and different final grid spacing (FGS) values.	84

Figure 6.4 - Influence of the ω_{BE} weight in image with SNR =6dB [49]. The vertical axis represents the error in pixels. The results with sequential 2D (red) and the proposed sequential 2D+t (blue) approaches are presented, in terms of RMSE (solid line) and EES (dashed line), using different metrics and different final grid spacing (FGS) values 85

Figure 6.5 - Influence of the ω_{BE} weight in image with SNR =6dB [49] using 4 scales. The vertical axis represents the error in pixels. The results with sequential 2D (red) and the proposed sequential 2D+t (blue) approaches are presented, in terms of RMSE (solid line) and EES (dashed line), using different metrics and different final grid spacing (FGS) values 85

Figure 6.6 - (Dys)functional regions detection using different methodologies. (a) t-MRI at end-systole, (d) DE-MRI, (b/e) radian strain map and (c/f) circumferential strain map using the sequential 2D (top) and the proposed sequential 2D+t (bottom). The arrows represent the borders of the dysfunctional region. 86

Figure 6.7 - (Dys)functional regions detection using different methodologies. In this situation a normal dataset is used. (a) t-MRI at end-systole, (d) DE-MRI, (b/e) radian strain map and (c/f) circumferential strain map using the sequential 2D (top) and the proposed sequential 2D+t (bottom). 87

Figure 6.8 - Capability to distinguish between dysfunctional and normal regions by assessing (a) radial and (b) circumferential strain. The different bars indicate the respective functional regions: (blue) infarct, (green) adjacent and (red) normal. * $p < 0.05$, ** $p < 0.001$ 87

Figure 6.9 - Validation of the (semi-) automatic segmentation technique. First line, test the intra-observer variability, the second line compare the first observer with the proposed method, the third line present the result between the second observer and the (semi-)automatic approach and the last line shows the results between a mean contour and the (semi-) automatic approach. The comparison was performed in terms of APD (average perpendicular distance) – first column, dice value – second column, and Hausdorff value – third column. 89

Figure 6.10 - (a) Global radial (red) and circumferential (blue) strain by using different methodologies: (solid line) the sequential 2D, (dotted line) sequential 2D+t using equation (4.7) and (dashed line) sequential 2D+t using equation (4.10) [proposed]. (b) Tag trajectory examples showing the difference between (blue) sequential 2D and (red) the sequential 2D+t approach. 90

Figure 6.11 - (a) Global radial (red) and circumferential (blue) strain by using different spacing in time direction: (dotted line) $\sigma t=3$, (dashed line) $\sigma t=2$ and (solid line) $\sigma t=1$. (b) Tag trajectory examples showing the difference between the proposed 2D+t approach with (blue) $\sigma t=1$, (red) $\sigma t=2$ and (green) $\sigma t=3$	90
Figure 6.12 - (a) Global radial (red) and circumferential (blue) strain using different methodologies; (solid line) proposed sequential 2D+t approach, (dashed line) fixed 2D+t approach using <i>NMI</i> and (dotted line) fixed 2D+t approach using <i>SSD</i> as metric.	91
Figure 6.13 - Validation of the methodology proposed for the fixed 2D+t FFD formulation presented in [70]. The first line shows the results using <i>SSD</i> and in the second line we present the results in terms of contour propagation using the <i>NMI</i> . In each line, the third and fourth columns are consecutive frames. The red arrow represents the “jump” of one frame between consecutive frames.	91
Figure 6.14 - (a) Linear regression, and (b) Bland-Altman Analysis in terms of global circumferential strain.	92
Figure 6.15 - (a) Linear regression, and (b) Bland-Altman Analysis in terms of segmental circumferential strain.	93
Figure 6.16 - (a) Linear regression, and (b) Bland-Altman Analysis in terms of global circumferential strain.	94
Figure 6.17 - (a) Linear regression, and (b) Bland-Altman Analysis in terms of segmental circumferential strain.	95
Figure 6.18 - Estimated Marginal Means values for each slice. The blue line represents the commercial software, and the red line the proposed methodology based on registration.	96
Figure 10.1 - Differences of tags inside the blood pool between the 1 st frame and 4 th frame.	127
Figure 10.2 - Polar image used to compute the low pass filter.	128
Figure 10.3 - Differences in the detagged image using a filter where the 1st harmonic of the tag frequencies is removed (first line) and the 1 st and 2 nd harmonics of the tags frequencies are removed.	128
Figure 12.1 - Tag tracking result of the proposed sequential 2D+t methodology in five human datasets.	130

Figure 12.2 - (Semi) Automatic segmentation result. In the image we present five different situations, with images from different slices, obtained from different centers.	131
Figure 13.1 - (a) Global radial (red) and circumferential (blue) strain by using different methodologies: (solid line) the sequential 2D, (dotted line) sequential 2D+t using equation (4.7) and (dashed line) sequential 2D+t using equation (4.10) [proposed]. (b) Tag trajectory examples showing the difference between (blue) sequential 2D and (red) the sequential 2D+t approach [117].	132
Figure 14.1 - Comparison between the software commercial (red line) with the proposed approach (blue line) in different cases.....	133
Figure 15.1 - (a) Linear regression, and (b) Bland-Altman Analysis in terms of global circumferential strain for the apical slice.	134
Figure 15.2 - (a) Linear regression, and (b) Bland-Altman Analysis in terms of global circumferential strain for the mid slice.....	135
Figure 15.3 - (a) Linear regression, and (b) Bland-Altman Analysis in terms of global circumferential strain for the basal slice.....	136
Figure 16.1 - (a) Linear regression, and (b) Bland-Altman Analysis in terms of global circumferential strain.....	138
Figure 16.2- (a) Linear regression, and (b) Bland-Altman Analysis in terms of segmental circumferential strain.....	138
Figure 17.1 - Boxplot of samples distribution.....	139

Tables list

Table 1.1 - Tagging pulses acquisition protocols [16]	8
Table 2.1 - Advantages and problems of the different methodologies for LV tracking.	21
Table 2.2 - Comparison between different methods available in literature for LV segmentation.....	27
Table 6.1 - Dice value, average perpendicular distance (APD), Hausdorff value for the endocardium using different comparisons between the non-experts (E1 and E2), the (semi-) automatic approach (Auto) and the mean contour (MC) obtained from E1 and E2. At same time, we compute the area of the endocardium and determine correlation coefficient (r) and BIAS. *Statistically significant (p<0.05)	88
Table 6.2 - Dice value, average perpendicular distance (APD), Hausdorff value for the epicardium using different comparisons between the non-experts (E1 and E2), the (semi-) automatic approach (Auto) and the mean contour (MC) obtained from E1 and E2. At same time, we compute the area of the epicardium and determine correlation coefficient (r) and BIAS. *Statistically significant (p<0.05)	88
Table 6.3 - Results from Doppler CIP study, in terms of global circumferential strain, using different methodologies. *Statistically significant (p<0.05)	92
Table 6.4 - Results from Doppler CIP study, in terms of segmental circumferential strain, using different methodologies. *Statistically significant (p<0.05).....	93
Table 6.5 - Results from Doppler CIP study, in terms of global circumferential strain, using different methodologies. *Statistically significant (p<0.05)	94
Table 6.6 - Results from Doppler CIP study, in terms of segmental circumferential strain, using different methodologies. *Statistically significant (p<0.05).....	94
Table 6.7 – Mean strain value in terms of global circumferential strain. The mean result for the commercial software and the proposed approach (NRR) are shown.....	95
Table 6.8 – Mean strain value in each slice for the different segments (S1, S2, S3, S4, S5, S6). The segmental peak results are used. In each slice we present the strain result for the commercial software and the proposed approach (NRR)	96
Table 6.9 - ANOVA table using the segmental peak strain results in each slice for the different software's presented	96
Table 11.1 - Number of cases where the user input was used. We count the number of slices where the user need to change the first estimation of the LV center position (Center Correction), the number of slices where the user change one point in the	

automatic initialization method (One Point Correction) and the number of cases where the apical slice was not segmented (Apical Contour fail)	129
Table 15.1 - Results from Doppler CIP study, in terms of global circumferential strain in the apical slice, using different methodologies. *Statistically significant ($p < 0.05$) using a paired t-test.....	134
Table 15.2 - Results from Doppler CIP study, in terms of global circumferential strain in the mid slice, using different methodologies. *Statistically significant ($p < 0.05$) using a paired t-test	135
Table 15.3 - Results from Doppler CIP study, in terms of global circumferential strain in the base slice, using different methodologies. *Statistically significant ($p < 0.05$) using a paired t-test	135
Table 16.1 - Results from Doppler CIP study, in terms of global circumferential strain, using different methodologies. *Statistically significant ($p < 0.05$) using a paired t-test	137
Table 16.2 - Results from Doppler CIP study, in terms of segmental circumferential strain, using different methodologies. *Statistically significant ($p < 0.05$) using a paired t-test.....	137
Table 17.1 - Residual values table.....	139

Introduction

1. Introduction

1.1. Cardiac anatomy and physiology

The heart is an intermittent pump that propels blood throughout the body [1]. This pump behavior is possible due to the characteristics of the cardiac muscle, also called the myocardium. The myocardium is composed of millions of small muscular cells with a specific organization. The inner surface is called the endocardium, while the outer surface is designated as the epicardium [2].

Anatomically, the heart has four chambers (Figure 1.1), the right and left atrium and the right and left ventricle (RV and LV). The atrioventricular valves (tricuspid and mitral valve) open passively, allowing the transfer of blood between the atria and the ventricles, and prevent backflow. To prevent the prolapse of the atrioventricular valves, the ventricles have structures called papillary muscles. There are five papillary muscles on the ventricles, three in the RV and two in the LV. These structures are connected to the atrioventricular valves [1, 3, 4].

Regarding the blood circulation, the atrium ejects the blood into the ventricle, which will further expel the blood towards the rest of the body. The activity of these chambers is similar to two pumps in series. The two ventricles are responsible for the blood flow between two systems, the systemic and pulmonary [2, 5]. In the pulmonary circulation, the right ventricle drives deoxygenated blood to the lungs. In the lungs, an

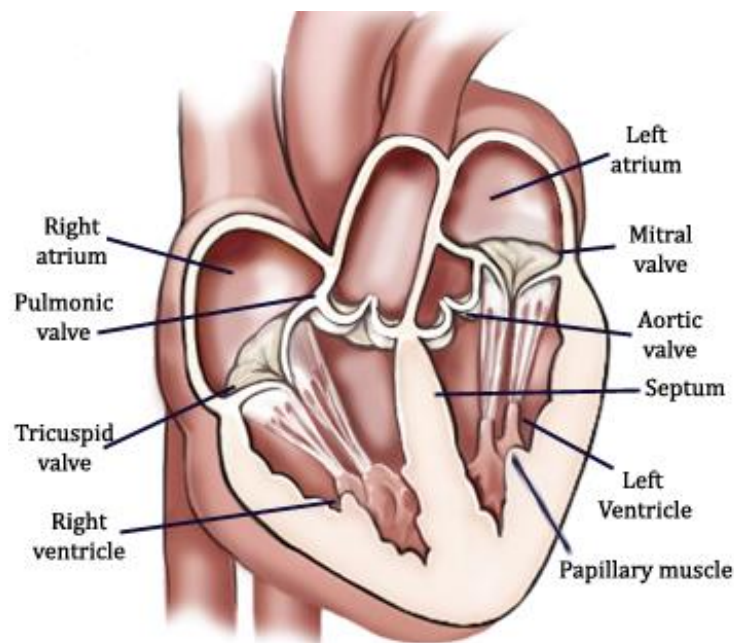


Figure 1.1 - The heart anatomy. Adapted from [6].

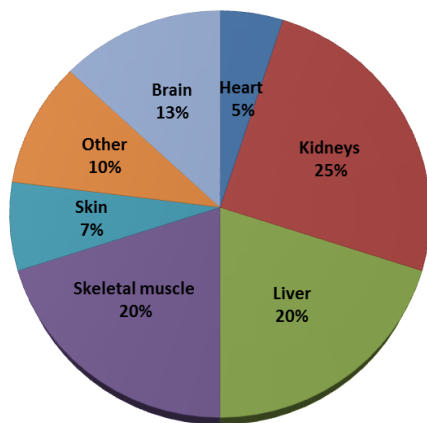


Figure 1.2 – Distribution of the blood output from the LV [2].

LV has a mass which is approximately three times higher than the RV and the myocardial wall is twice as thick. The pressure in this chamber (LV) is also typically three times higher than the RV. In resting conditions, each ventricle pumps approximately 5 l/min. During exercise, this value can increase up to 5 times [1, 3].

The heart function is a complex process, where the different cavities interact and the cardiac contraction should occur in a rhythmic and coordinated fashion [1]. The cardiac cycle can be divided into diastole and systole. End-diastole (ED) occurs when the ventricles are relaxed and marks the phase when they are maximally expanded. End-systole (ES) is characterized by the maximum contraction of the heart [2].

The heart contraction is regulated by electric pulses that propagate throughout the myocardium. The electrocardiogram (ECG) is a system used to record electric activity of the heart from the surface of the body. The ECG signal can be divided into: the P wave caused by the activity of the atrium, resulting in a transport of blood towards the ventricles; the QRS complex, which originates from the contraction of the ventricles. This complex defines the ED moment; and the T wave represents the onset of ventricular relaxation [5].

1.2. Cardiac motion

1.2.1. Cardiovascular diseases

Cardiovascular diseases (CVDs) contain the heart and circulatory system anomalies, and include for example coronary heart diseases, cardiomyopathies, heart failure and valvular heart diseases.

oxygenation process occurs. Next, the blood continues to the left part of the heart, where the left ventricle pumps blood towards the rest of the body (Figure 1.2) [2].

In terms of structure, each chamber has different properties of the walls. The ventricles, which develop much higher pressures compared to the atria, have thicker muscular walls. The

Coronary heart diseases (CHDs) are associated with a reduced blood supply of the myocardial tissue, which can lead to ischemia and cause damage or death of the cardiac cells. Consequently, the wall loses the capability to contract, and a regional dysfunction occurs. This reduction can originate from atherosclerosis of the artery, or an accumulation of lipids in the vessel wall, or complete occlusion of the artery [7].

Cardiomyopathies are diseases that primarily affect the myocardium. They are related with asymmetric growth of the heart muscle, which will affect the normal ventricular structure and function [2]. In hypertrophic cardiomyopathy, the thickness of the ventricular wall is locally enlarged, e.g. septal hypertrophy. The asymmetric growth will affect the normal heart function, and in severe cases can obstruct the ventricular output. This disease can be detected with ECG, since the thickened septum will affect the ventricular and atrial contraction. This anomaly can lead to heart failure with an increased end-diastolic volume and reduced ejection fraction from both ventricles [2].

Heart failure corresponds to the loss of pumping performance by the heart. This problem will reduce the quantity of blood ejected into the aorta or the pulmonary artery. As such, the heart contraction is negatively affected due to the increased afterload. Heart failure can be caused by several causes, e.g. mitral stenosis, hypertrophic cardiomyopathy and aortic stenosis [1].

Finally, valvular heart diseases (VHDs) are related with the cardiovascular valves. When they function normally, they open passively during the heart contraction, and are responsible for a proper blood transfer between the cavities and the rest of the body. Malfunctioning can occur due to a (aortic and mitral valve) stenosis and leads to regurgitation. This will affect the heart pump activity, and the myocardial muscle typically enlarges and thickens [3, 8].

1.2.2. Regional heart deformation

The CVDs typically manifest themselves during the heart contraction. Since many CHDs result in local myocardial dysfunction, research on local wall motion and deformation has gained considerable attention over the last decade and is currently one of the main research topics.

To quantify the heart function, mechanical principles can be used, such as strain. The strain value is an indicator about the deformation in a certain direction. This mechanical quantitative parameter can quantify the heart contraction at global and regional levels.

Studying heart function is not straightforward due to the difficult access to this organ. Invasive surgeries for visualizing the heart presents several drawbacks, and in the last years some methods based on medical imaging techniques were therefore proposed.

Initially, the ventricular wall motion quantification was realized using implanted radiopaque markers and tracking them with X-ray in canine hearts [9]. However, these techniques are invasive and not feasible in clinical practice. To solve these problems, several studies were presented [10-15], where different methodologies were developed using echocardiographic imaging, cine magnetic resonance imaging (cine-MRI) and tagged MRI (t-MRI). The conventional image modalities, such as echocardiography and cine-MRI are useful to assess global cardiac function, but the assessment of the regional wall function can be challenging. t-MRI is an interesting technique for global and regional assessment of the heart's mechanics. In section 1.2.3, a description about this technique will be presented. Finally, in section 1.3 an explanation about the medical image processing methods will be performed.

1.2.3. Tagged Magnetic Resonance Imaging

Tagged Magnetic Resonance Imaging is an imaging technique that induces a spatial line or grid pattern in the tissue of interest by spatially presaturating the tissue magnetization (Figure 1.3). This image modality differs from the other MRI acquisitions in the combination of radio-frequency (RF) and gradient pulses in order to define a regular pattern on the image. These patterns are called tags and they move and deform with the myocardium. The tags can be used to locally study the heart deformation. As advantages, the presence of tags on the myocardium wall makes studying the regional wall deformation easier and simplifies the assessment of certain motion components, such torsion. Nevertheless, the analysis of these datasets is challenging due to tag fading, the relatively low spatial resolution and the big variability in terms of tag properties between datasets, making it hard to delineate the cardiac anatomy (Figure 1.3) [16-18].

To produce the tag patterns several popular imaging sequences can be used, for example: the spatial modulation of magnetization (SPAMM) [19], delays alternating with nutations for tailored excitations (DANTE) [20], radial tags [21], hybrid SPAMM/DANTE [22], complementary spatial modulation of magnetization (CSPAMM) [23], sinc-modulated DANTE [24] and 3D-CSPAMM [25]. The advantages and disadvantages of these acquisition protocols are shown in Table 1.1.

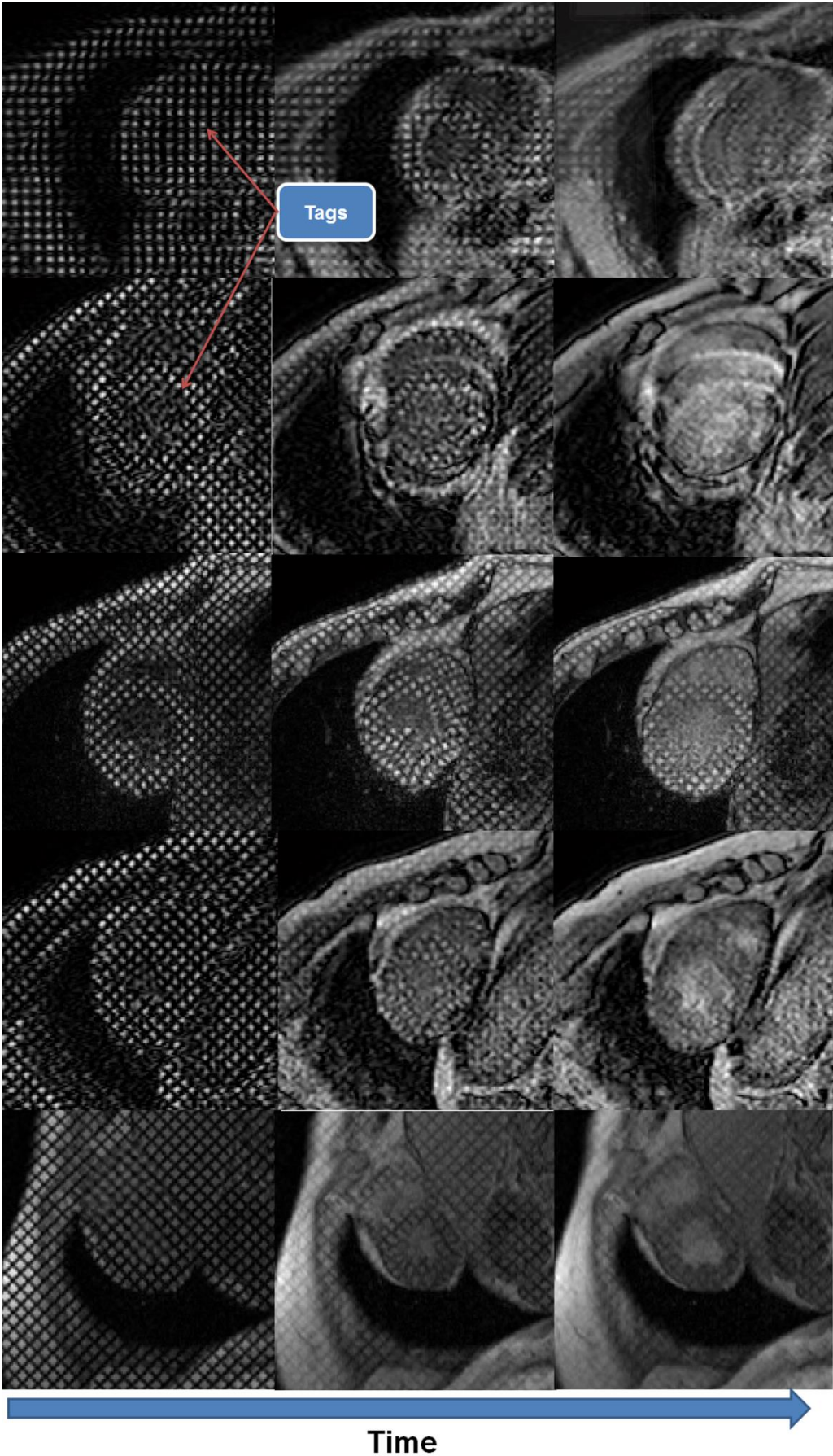


Figure 1.3 - Five t-MRI sequences.

Table 1.1 - Tagging pulses acquisition protocols [16]

Method	Advantages	Disadvantages
SPAMM [19]	Fast, efficient.	Sensitive to tag fading.
CSPAMM [23]	Longer net tag persistence; suppresses untagged blood.	Longer image acquisition.
DANTE [20]	Faster than SPAMM.	The RF technique is difficult to implement.
Sinc-DANTE [24]	Sharper tags.	The RF technique is difficult to implement.
SPAMM/DANTE [22]	Less demanding on RF than full DANTE; Less demanding on gradient than SPAMM.	Less benefits than either alone.
Radial [21]	Better performance in the circumferential direction.	Inefficient to implement.
3D CSPAMM [25]	Real 3D tagging.	Difficult to implement.

The differences between the acquisition protocols are related to the tag properties, such as the sharpness of the tag pattern, the contrast-to-noise ratio of the tag compared to the myocardium and the tag persistence during the acquisition. The sharpness of the tag pattern is not an essential factor, but the myocardium tag contrast-to-noise ratio should be high enough to allow detecting the heart motion [26].

In the current master thesis, the t-MRI images used are acquired with the SPAMM protocol. As such, an explanation about this technique will be presented next.

Regarding the SPAMM technique, initial work was performed by Zerhouni *et al.*, in which a method for tagging a few parallel planes within the heart wall using selective RF excitation was suggested [26]. In 1989, Axel and Dougherty introduced the SPAMM technique to produce saturated parallel planes throughout the entire volume [18]. Figure 1.4 shows the method typically used by SPAMM. The tagging sequence is triggered by the upslope of the QRS from the ECG. After the trigger signal, image acquisition is performed and a magnetization storing sequence, composed of a crusher gradient and tagging pulse trains, is applied. The crusher gradient is used to dephase any transverse magnetization and the tagging pulse trains will define the tag pattern. Tagging pulse sequences are usually imposed at ED. Typically the grid is created based

on the combination of horizontal and vertical stripes. After the tagging step, a new RF pulse will restore the magnetization back to its steady-state position [16, 17, 22]. The main drawbacks of SPAMM are its fast tag fading and the requirement of repeated RF excitations during imaging.

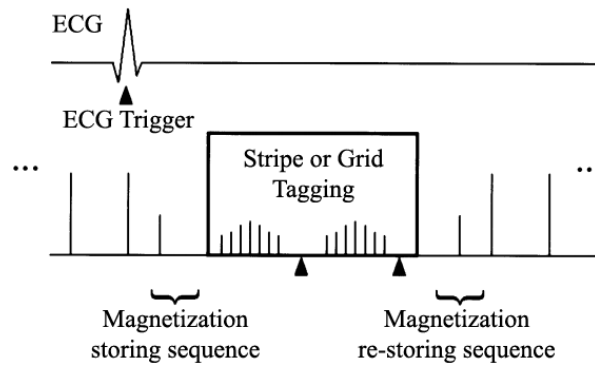


Figure 1.4 - Schematic about the SPAMM tagging pulse methodology. Adapted from [26].

In 1993, Fischer *et al.*, suggested a new approach to minimize tag fading using a complementary SPAMM (CSPAMM). In this case, two tagged SPAMM images, 180° out of phase with each other are acquired. The CSPAMM is then created by subtracting both images. The main disadvantage is the increased image acquisition time [23].

Please note, these images allow assessing motion in-plane by following the tag deformation, but do not allow estimating the out-of-plane components. Given the three-dimensional complex heart motion, the assessment of the strain using a 3D model would be beneficial. Some strategies have been proposed to solve this problem by combining short axis (SA) and long axis (LA) views (see Figure 1.5) [27].

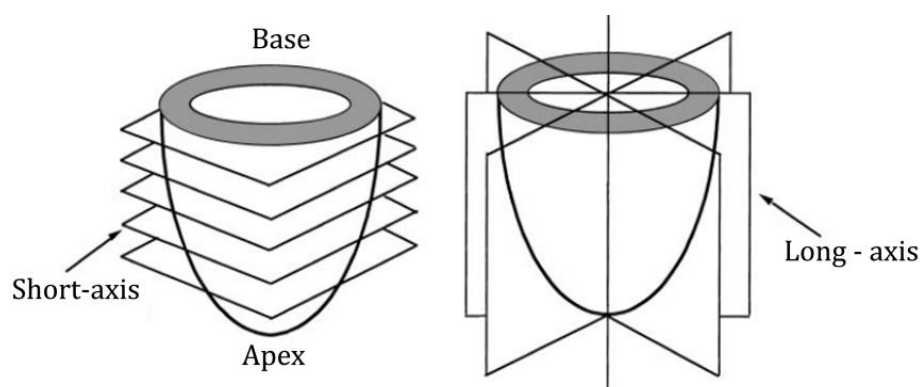


Figure 1.5 - Definition of the SA and LA views. Adapted from [28].

As an alternative, Ryf *et al.*, proposed a real 3D tagging sequence (3D CSPAMM - Figure 1.6). The images are acquired with two 90° block pulses, interspersed by a dephasing gradient. A strategy similar to SPAMM is used, where a sinusoidal modulation of magnetization is used to create a shaped tag pattern. To create

a 3D grid, the modulation is repeated in all three spatial directions. The second 90° pulse is used to create the complementary image, but in this case the modulation is inverted. The subtraction between the two images in each direction reduces the tag fading in the 3D tagging acquisition. As such, this technique can estimate the 3D motion, without the misalignment problems related with the combination of different SA and LA views [25].

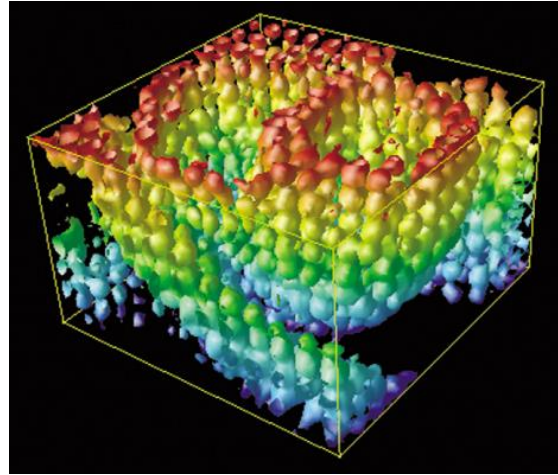


Figure 1.6 - 3D tagging structure visualized by isosurface rendering of the 3D dataset [29].

1.3. Medical Image Processing

Medical image processing focuses on the manipulation and analysis of medical images to enhance and illuminate important structures inside the data stream [30]. This research field is applied in clinical practice to improve diagnosis and monitor disease progression.

Medical images can be acquired using a wide array of image modalities such as ultrasound (US), single photon emission computed tomography (SPECT), positron emission tomography (PET), computed tomography (CT) or MRI [31].

The main topics of research and challenges are: image enhancement and restoration, to improve the image quality; automated and accurate segmentation, to delineate anatomical structures; image fusion using registration, to combine information from different image modalities; disease progression studies, and, image tracking.

1.3.1. Medical Image Segmentation

Segmentation can be defined simply as the partitioning of a dataset into contiguous regions whose pixels/voxels have common and cohesive properties [30]. In medical imaging, this is commonly used to delineate important structures, e.g. pathologies, organs and tumors (Figure 1.7). The principal challenges are the image quality (noise, limited contrast), the large diversity of objects and images, the large variability in size and shape, and the unknown ground truth [30].

The segmentation can be done using manual, semi-automated or automatic approaches [32]. Manual segmentation is a tedious, time consuming and subjective task.

Semi-automated and automated approaches aim to solve these issues. The development of these methods is not straightforward and can be difficult to implement within clinical practice. The semi-automated segmentation requires a user dependent framework. In terms of final output, high efficiency and large applicability can be achieved, but variability between observers is expected. The automatic approaches are only based on the input image, and no user input is required. With these approach, the final result is independent of the variability and clinical experts [33].

Segmentation methods can be classified into image-based, model-based and hybrid methods [32]. The image-based methods only rely on image data and include the following techniques: thresholding [34], region growing [35], mathematical morphological operations [36], active contours [37], level sets [38], live wire [39] and watershed [40]. These methods typically achieve a high performance in high quality images. Model segmentation methods exploit object shape and/or appearance through the use of atlases [41], statistical active shape models [42] or statistical active appearance models [43]. These models can segment bad quality images and can contour correctly even if information is missing on the image [32].

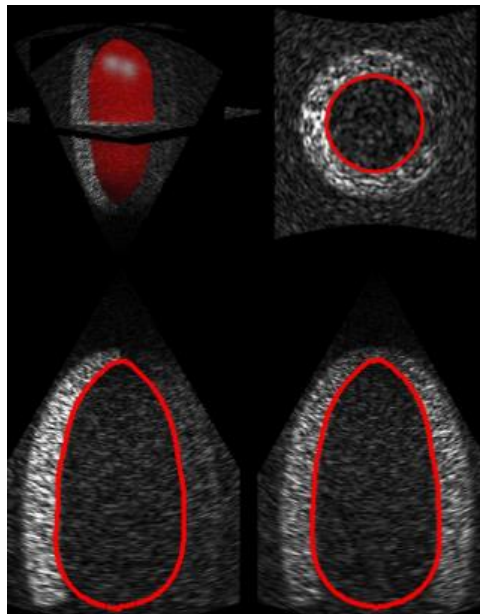


Figure 1.7 - 3D endocardium segmentation in echocardiography image [44].

The hybrid methods use the properties of the last two classes to develop more powerful segmentation tools, with superior performance and robustness over the individual methods [32].

1.3.2. Medical Image Registration

Medical image registration is the process of finding the spatial transform that maps the points from one image to the corresponding points in another image (Figure 1.8) [30]. Typically, the moving image represents the image where the transformation is applied, and the fixed image the reference for the alignment. The registration problem will search for the best transformation capable to map the moving image onto the fixed image. This transformation will minimize the differences between the two images.

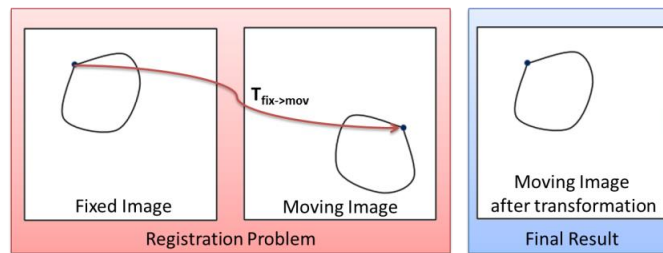


Figure 1.8 – Registration problem. Searching for the best transformation (T) capable to map the moving image on the fixed image with minimum error.

Normally, the registration problem has a scheme similar to the Figure 1.9, where an iterative process is used to detect the optimal transformation between the two images. In each iteration, a different transformation is applied on the moving image, and a metric is used to compare the two images. The optimal transformation describes one image in terms of the other with the minimum error [45].

Several transformation classes can be defined, depending on the number of parameters to be optimized and the amount of deformation they can model, e.g. rigid, affine and non-rigid. The amount of parameters to be optimized will affect the computation time [45].

Rigid transformation has 6 degrees of freedom (DOFs), where translation and rotation are the only transformations allowed to be applied on the two images during the alignment (see Figure 1.10a). The affine transformation has 12 DOFs, and uses all the transformation from the rigid transformation plus scaling and skew between the two cases (Figure 1.10b). Finally, non-rigid transformation, also known as elastic image registration, is a more complex process, where more DOFs are available to detect and describe local deformations between the two images (Figure 1.10c) [30]. Obviously, in terms of computational time, the non-rigid registration has the highest value, and the rigid transformation the lowest one.

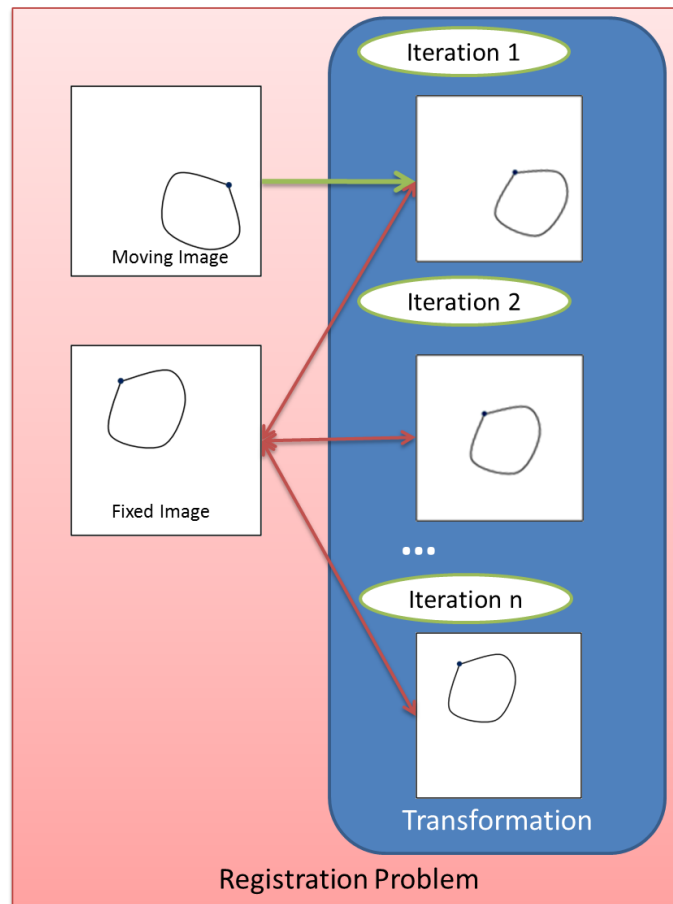


Figure 1.9 - Registration problem scheme.

Three classes of registration can be distinguished: point-based, – minimizes the averages distance between corresponding points; surface-based, - minimizes the average distance between the surfaces; and, voxel-based registration, – minimizes the differences in terms of intensities between the two images. In the current work, we focus on voxel-based registration methodology.

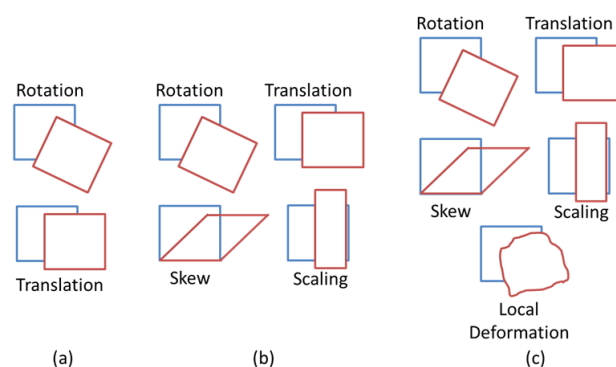


Figure 1.10 – Transformation models used by (a) rigid registration, (b) affine registration, and, (c) non-rigid registration [46].

Multimodal and unimodal registration are two different problems of registration. The multimodal registration occurs between images acquired from different medical devices (e.g. MR and CT), where the images present different properties, for example intensity. Unimodal registration uses images acquired from the same image modality, with similar properties between them. In each situation, different registration configurations should be used. For example, in a multimodal registration we can not use a similarity metric based on intensities, since there are no relation between the intensities in the two cases. A metric only based on the difference in terms of intensity is typically used in a unimodal registration problem.

Nowadays, image registration is useful within clinical practice and can be applied in several scenarios. For example, it can be used to assess disease progression by aligning multiple images acquired at different time instances (Figure 1.11) [30, 47].

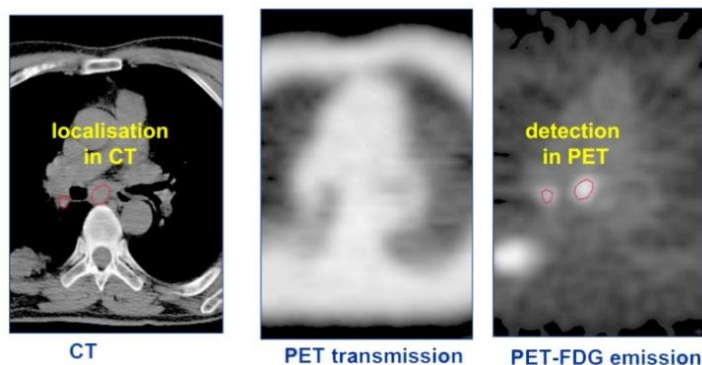


Figure 1.11 - Example of thorax tumor staging from PET and CT [46].

Another example is related with image fusion to combine the advantages from different modalities (e.g. CT and PET). In this case, an image with more information, compared to the individual images, can be created. For example, MR images have good soft tissue discrimination for lesion identification, while CT images provide good bone localization, which is useful for surgical guidance (see Figure 1.12) [47].

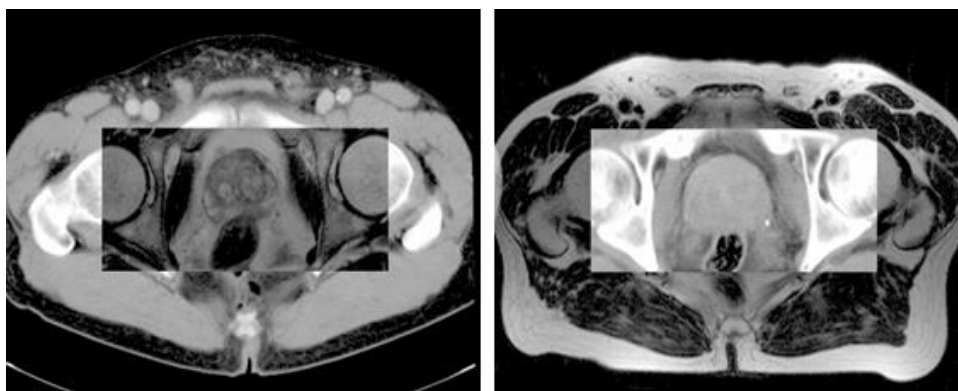


Figure 1.12 - Example of fusion data from MR and CT by image registration. (left) MR overlaid on CT and (right) CT overlaid on MR [46].

1.4. Motivation

In 2008, a European study showed that cardiovascular diseases (CVDs) and circulatory system diseases are the main cause of death in Europe (Figure 1.13a). Each year, CVDs cause 4.3 million deaths in Europe and over 2.0 million deaths in the European Union. Overall, CVDs have a financial impact of €192 billion a year [48].

Figure 1.13b shows the CHDs prevalence in each country. The image indicates that the number of deaths is generally higher in Central and Eastern Europe than Northern, Southern and Western Europe [48].

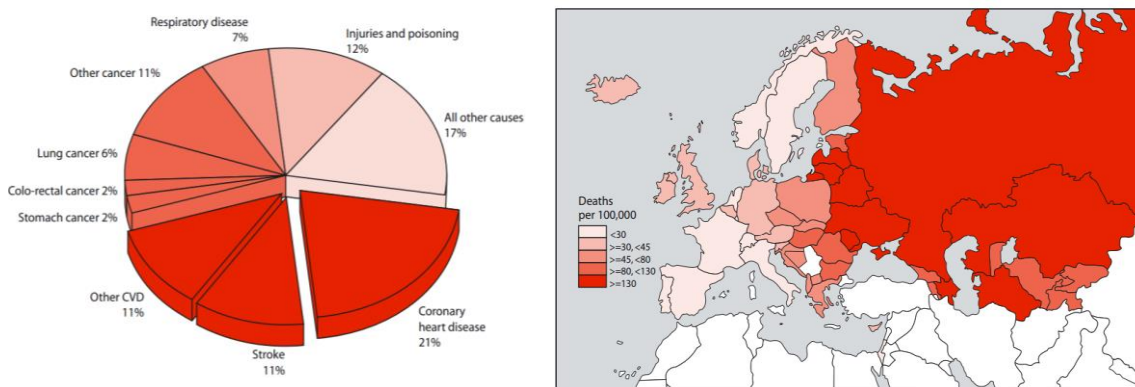


Figure 1.13 - (a) Deaths by cause in Europe (b) Death rates from cardiovascular problem in each country of Europe [48].

A variety of diseases can affect the heart function and it is important to study wall motion and deformation. These two factors are important clinical indicators on regional heart function.

Since the LV is responsible to pump the blood to the whole body, the biggest pressures occurs inside this cavity. Based on this fact, a large number of diseases will be detected on the left ventricular wall. It is important to mention that all the heart cavities do not work independently, and a problem in one structure will influence the others. A complete study about the myocardial wall in all the cavities will be an important indicator to detect dysfunctional regions. In the present work, we focus only on studying the left ventricular wall, due to the biggest pressures, the large area and importance of this cavity during the cardiac cycle.

Finally, it is important to mention that a regional quantitative assessment of the LV wall deformation is not straightforward, due the difficult to quantify the cardiac motion without specific software.

1.5. Aim

In this project, we intend to develop a method to automatically assess the LV wall deformation using t-MRI. The t-MRI images are commonly used, due to the accurate results achieved in the computation of regional heart deformation and the possibility to study torsion effects [17].

To automatically extract myocardial strain, we focus on both tracking the myocardium, as well as, automating the definition of the region-of-interest (ROI) by developing a segmentation algorithm for the endo- and epicardium.

Smal *et al.* [49] compared four frequently used MRI tracking methodologies: optical flow, harmonic phase, B-spline snake grids and non-rigid registration based on free-form deformation (FFD) transformation model. Based on their results, non-rigid image registration was selected to be developed in this thesis. The registration problem was reformulated to include temporal information on the transformation model used. We expect to develop a more coherent tracking methodology, with high accuracy, and, able to estimate the motion field on a large number of images, available in different clinical t-MRI datasets.

Segmentation of t-MRI images is a challenging task due to the high variability of t-MRI images properties. We therefore first propose a detagging step by filtering in the Fourier domain. Next, a B-Spline Explicit Active Surface (BEAS) framework is used to segment the myocardium and indicate a ROI for strain estimation. This framework has already been proven successful for the segmentation of the LV in US [44] and cine-MRI [33]. In the end of this task, we intend to develop an automated framework for LV segmentation in a large number of t-MRI images (with different image properties, e.g. image intensities, tag orientation).

1.6. Thesis outline

The second chapter describes the methodologies available in literature, for LV tracking, detagging and segmentation of t-MRI images.

In the third chapter, an explanation about the fundamentals of the registration problem, image segmentation using active contours models and strain estimation is given. This chapter is essential as a rationale and basis for all the innovations that will be proposed in the next chapter.

The fourth chapter describes all the methods developed during the master thesis. All the techniques indicated in this chapter are not available in literature, and a detailed description about the implementation and limitations is presented. This chapter focuses on the tracking problem, using a non-rigid registration method with a new formulation of the transformation model, and in a new methodology for detagging and segmenting t-MRI images.

In the fifth chapter we describe the datasets and the experiments used to validate the different steps of the developed framework.

In the sixth chapter, we show the validation results for all the proposed methods. This is achieved by a direct comparison between the proposed methods and the available commercial software package.

The seventh chapter discusses the results obtained in the previous chapter.

Finally, in the eighth chapter, the main conclusion of the thesis, the limitations of the present framework, the contributions and possible future work are presented.

LV tracking and segmentation in t-MRI images

2. LV tracking and segmentation in t-MRI images

In this chapter, a description about the methods available in the literature for LV tracking, LV detagging and LV segmentation in t-MRI is presented. Initially, all the tracking categories used for these images are explained. During this explanation we will emphasize the available non-rigid registration methodologies, due the importance for the current work. In a second part of this chapter, the available detagging and segmentation methods are presented.

2.1. LV tracking methods

Techniques to track the myocardium within t-MRI images can be grouped into: tracking landmarks, harmonic phase (HARP), local sine wave modeling, gabor filter banks, deformable models, optical flow methods and registration based methods [18]. A comparison between the different methods is available on the Table 2.1.

Table 2.1 - Advantages and problems of the different methodologies for LV tracking

Method	Advantages	Disadvantages
Tracking Landmarks	The method uses only information based on the tag positions;	Sensitive to the tag fading and dependent of the image properties;
HARP	The motion field is estimated in the frequency domain; The method is fast;	Can fail in the presence of a large amount of motion;
Local sine wave modeling	Less sensitive to artifacts, faster, better noise reduction and with higher accuracy when compared with HARP;	Fail in the presence of a large amount of motion; More difficult to implement when compared with HARP; Few works using this methodology;
Gabor Filter Banks	More adaptive to large tag deformation;	More dependent of the images properties, when compared with HARP;
Deformable Model	High feasibility to estimate the motion field.	Some approaches use a tag extraction step; High computational time;
Optical Flow	Does not require explicit modeling of the tags.	Fail in the presence of a large amount of motion; Sensitive to the tag fading;
Non rigid registration	High accuracy; Less sensitive to tag fading;	Intensive computation required;

The tracking landmarks method directly uses the tags position present in the image to estimate the displacement field (see Figure 2.1) [18]. Kerwin and Prince estimate the 3D displacement field using this technique. In their approach, each tracked point is located at the intersection of the three tag surfaces, which is estimated using splines and an iterative approach [50]. Amini *et al.* proposed a similar technique, where B-splines are used to estimate the displacement and create a parametric representation of the tags with a low computation time [51].

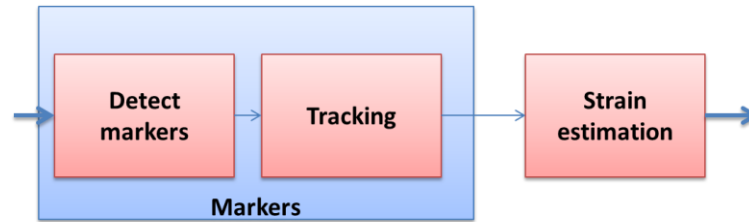


Figure 2.1 - Block scheme of strain estimation using tracking landmarks.

HARP is an image processing technique, where the original image is analyzed in the frequency domain, using a fast Fourier transform (FFT). In the frequency domain, the t-MRI images show distinct spectral peaks, each of which containing information about the motion. The inverse Fourier transform of a single peak, extracted using a bandpass filter, is a complex image whose phase is linearly proportional to a directional component of the motion (see Figure 2.2). These algorithms are typically fast and automatic, but have a lower performance when large motions occur [18]. Ryf *et al.* improved the HARP technique, using the positive and negative tag peak to increase the accuracy [29]. On the other hand, Sampath *et al.* created a new pulse sequence method to acquire only a small region around the selected spectral peak. This allowed to reduce the acquisition time considerably and assess the heart motion in real-time [52]. Previous approaches only measure the motion in 2D, as such Pan *et al.* extended the traditional HARP method to 3D. This 3D analysis uses a stack of SA and LA images [53]. Another technique capable to estimate the 3D motion was proposed by Abd-Elmoniem *et al.* [54]. Here, the Z-HARP pulse sequence method estimates motion in-plane and through-plane from a single image plane [54]. Liu *et al.* suggested a new refinement method to improve the robustness of the 3D estimation algorithm. In this case, the method searches the optimal motion for each pixel in the original image by solving a single shortest path problem. They showed that errors could be reduced in images with large motion [55]. Additionally, it is important to mention that the HARP is used in current commercial packages for motion estimation in t-MRI images [56].

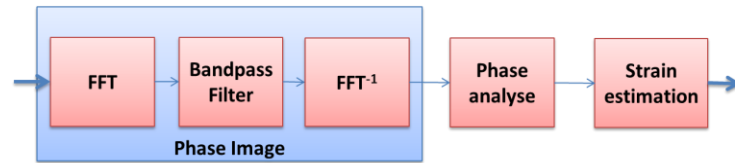


Figure 2.2 - Block scheme of strain estimation using HARP.

The local sine wave modeling is a frequency-based method similar to the HARP methodology. In this method, the phase and frequency of each pixel are directly estimated from the frequency domain. Then, the displacement is calculated from the ratio of phase difference and local frequency. Arts *et al.* shows that the proposed technique is as fast as HARP but with higher accuracy, noise reduction and lack of artifacts [57].

Another commonly used technique to estimate the motion field, is based on gabor filter banks. This technique uses a band-pass filter with a gaussian form multiplied by a complex sinusoid. The phase response can then be used to track the tags and heart motion (see Figure 2.3) [18]. Montillo *et al.* presented a work using this technique to estimate motion in a 2D approach and proposed the parameters that maximize the filter response [58]. Qian *et al.* extended the previous work to 3D [59]. Chen *et al.* proposed a new technique to estimate motion in 3D with high accuracy, combining the response of the gabor filters, gradient information of the original images, an intensity probabilistic model and a spatio-temporal smoothness constraint [60].

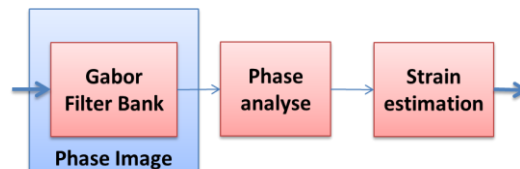


Figure 2.3 - Block scheme of strain estimation using gabor filter bank.

Deformable models typically use a model to fit the data using energy minimization criteria (see Figure 2.4) [18]. Clarysse *et al.* proposed a cosine series based model to get a mathematical expression of the reconstructed displacement field for 2D t-MRI images. The coefficients of the cosine model were obtained by minimizing the distance between the projection of deformed tag lines and undeformed ones [61]. Other methods using 3D or 4D B-splines were suggested later in, e.g. [62, 63]. In these works, the model fitting is expressed as an energy minimization problem, where the objective is the optimization of the cost function which encodes the distance between the isoparametric planes and MRI tags planes. In these cases, the output was a time-varying B-spline solid whose knot planes reconstructed the tag surfaces in the

three orthogonal directions for all the points. Tustison *et al.* further improved this approach using a new internal energy, based on the information over the entire 4D space [64]. The same authors proposed an alternative transformation model based on Non-Uniform Rational B-splines (NURBS) model. This model was implemented in polar and cylindrical coordinates and restricted to the ventricular wall [65].



Figure 2.4 - Block scheme of strain estimation using deformable models.

Optical flow techniques track tissue based on a differential analysis of motion. The spatial gradient and spatial time derivative at each pixel is used during the computation. The method assumes that the image intensity remains constant between consecutive frames (see Figure 2.5). This assumption may be violated in t-MRI, due to the tag fading during the cardiac cycle [18]. Prince and McVeigh overcame this limitation by proposing a term in the optical flow formulation which accounts for the variable brightness of the tag lines [66]. Dougherty *et al.* used a similar method, but in this case a Laplacian filter was used to compensate intensity differences [67].

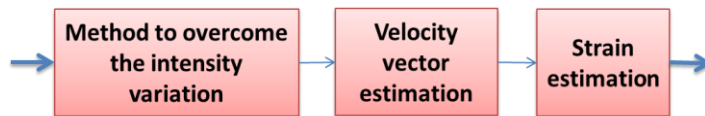


Figure 2.5 - Block scheme of strain estimation using optical flow methodology.

The registration based method uses an iterative process to determine the optimal transformation between two images. The optimal transformation is used to estimate the strain between each frame (see Figure 2.6).

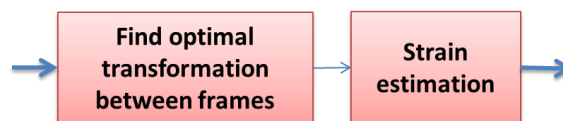


Figure 2.6 - Block scheme of strain estimation using non-rigid registration.

Chandrashekhara *et al.* adopted a non-rigid image registration framework for t-MRI [68]. It was inspired by the work of Rueckert *et al.* [69], which was previously applied on breast MR images. In the original work of Rueckert *et al.*, Mutual information (MI) was used as a similarity metric and an initial global transformation is firstly found followed by a local transformation to refine motion [69]. On the other hand, Chandrashekhara *et al.* omitted this initial global transformation since no large motion differences were expected over the cardiac cycle. The normalized mutual

information (*NMI*) was selected [68] as a similarity metric and the reference image was always the ED frame (in this thesis termed “pairwise 2D alignment”, see Figure 2.7a). In the same year, Chandrashekara *et al.* proposed another approach, where the temporal information was included in the registration [70]. In this case, the registration problem was defined between two image sequences: a fixed image sequence with a repeated ED frame, and a moving image sequence containing the actual cardiac sequence (termed “fixed 2D+t alignment”, see Figure 2.7b). The proposed method was compared with the first approach in [68], and the results suggested that the fixed 2D+t alignment [70] allowed estimating the motion with a higher accuracy compared to a traditional pairwise strategy. Inspired by the approach of Rueckert *et al.* [69], Oubel *et al.* adopted the same image registration scheme (“pairwise 2D alignment”, Figure 2.7a) [71, 72] but with a new similarity metric, α -MI. In 2007, they extended their work from 2D to 3D, by combining information from the SA and LA views [73]. In 2011, Oubel *et al.* proposed an alternative registration scheme. Instead of the typical pairwise registration, a set of transformations were first defined with the reference image always being the ED frame. All the transformation were then optimized simultaneously to minimize α -Entropy (“joint 2D+t alignment”, Figure 2.7c) [10]. This new technique was compared with the pairwise 2D alignment approach of Chandrashekara *et al.* [68], and a higher accuracy was obtained. Lastly, Shi *et al.* described a new idea, where cardiac motion was estimated using information from t-MRI and non-tagged MRI. Their results suggest that combining t-MRI with untagged MRI may leads to a higher accuracy compared to registration methods solely based on t-MRI or cine-MRI [74].

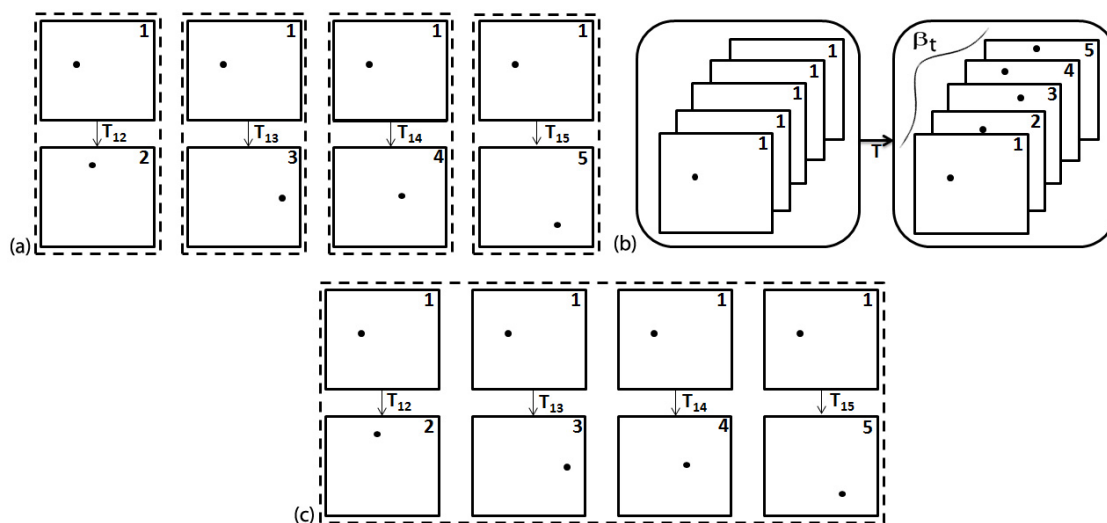


Figure 2.7 - Different registrations schemes: a) pairwise 2D [68], (b) fixed 2D+t alignment [70], (c) joint 2D+t alignment [10].

2.2. LV segmentation methods

The main problems to segment t-MRI images are typically related with the tag properties: myocardial boundaries are often obscured or corrupted by the tagging lines; increase of the intensity contrast between tagged and un-tagged tissues with a lower contrast between the myocardium and the blood pool; and, myocardium and blood pool intensities varies during the cardiac cycle due to the tag lines fading in the myocardium and being flushed away in the blood [75].

To cope with some of these challenges, several methods have been developed (Figure 2.8).

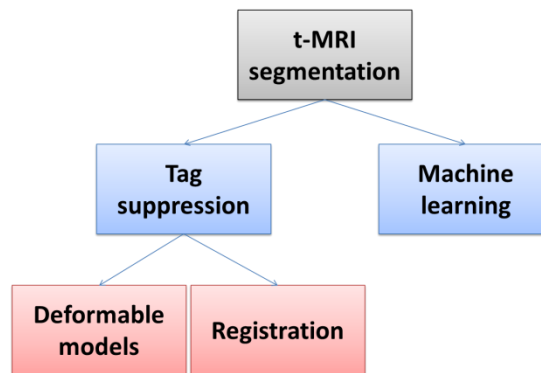


Figure 2.8 - Methods to segment t-MRI images.

One group of those has focused on suppressing the tags first, followed by a segmentation based on deformable models, or, by image registration with other MRI-image (see section 2.2.1). The main drawback of these methods is the detagging step, where a filter is used to remove the tag frequencies, which result in a blurred and low contrast image. The other group of methods is based on machine learning. However, the segmentation result is largely dependent on the images used (number of cases and variability between images) during the training step of the algorithm (see section 2.2.2).

A comparison between the different methods proposed in the literature for LV segmentation in t-MRI is showed in the Table 2.2.

2.2.1. LV segmentation after un-tagging t-MRI images

In 1994, Guttman *et al.* used a morphological closing operation to remove the presence of tag lines in a ROI defined by the user. The Sobel filter was then applied on the closed image and the result in terms of magnitude and angle was used to detect the concentric circles. Since the Sobel filter will detect several boundaries on the image, dynamic programming is used to detect the optimal contour, using the method proposed

Table 2.2 - Comparison between different methods available in literature for LV segmentation

Authors	Advantages	Disadvantages
Guttman et al. [76]	The first work proposed for LV segmentation in t-MRI, using only classical operations;	The method was validated in a few number of images; The method was only applied in line tag pattern images;
Manglik et al. [77]	A more adequate suppression technique is used. Better results are expected when compared with [76];	The method was only applied in line tag pattern images;
Milles et al. [78]	Less dependent of the image properties;	The method was validated in a few number of images;
Zhen et al. [59]	The window of the filter is adapted to the tag frequencies.	The method was only applied in line tag pattern images;
Camara et al. [79]	High accuracy for the estimation of LV contour;	The registration can introduce some errors; High computational time;
Huang et al. [80]	The method was applied in a large number of images, with a high TPF;	The method was only applied in line tag pattern images; High computational time; Dependent of the images used during the test phase;
Qian et al. [75]	High accuracy is expected;	The method was only applied in line tag pattern images; High computational time; Dependent of the images used during the test phase; A small number of images were used during the validation;

in [81]. Furthermore, the cavity is assumed to be darker than the myocardium (see Figure 2.9). The method was applied in 8 images, and the authors suggest a good correspondence, by visual assessment, between the detected contours and the cardiac boundaries [76].

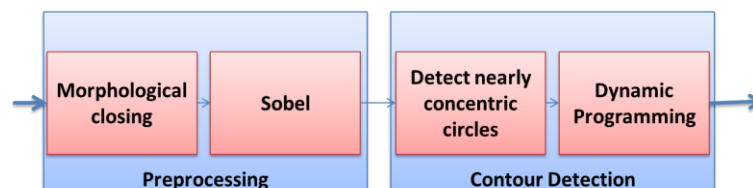


Figure 2.9 - Block scheme for segmentation in t-MRI using the strategy proposed in [76].

Manglik *et al.* used a 2D Gabor filter (a band-pass filter) to remove the tags, with the central spatial frequency of the filter set equal to the frequency of the tags on the image. The proposed filter only removes the tags, while keeping the lower or higher spatial frequency components of the image. After the tag suppression, the contours for the LV and RV are obtained using an active contour methodology. The method was compared with a ground truth (obtained using a manual segmentation), and the error was of 8% (see Figure 2.10) [77].

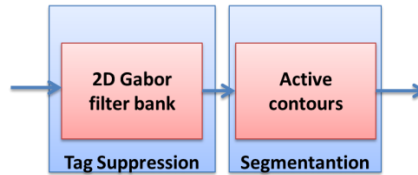


Figure 2.10 - Block scheme for segmentation in t-MRI using the strategy proposed in [77].

Milles *et al.* suggested a three steps technique to automatically segment the LV from a t-MRI sequence using motion information (Figure 2.11). The preprocessing step is used to compute motion fields using a methodology similar to HARP. A band-pass filter centered on the tag frequency is used to create an envelope of the tags. The last two steps are the template initialization and a segmentation of the LV based on the deformable template model proposed in [82]. The method was tested on simulated and in vivo datasets, with 2 pigs dataset, 1 health volunteer dataset and 2 pathologic dataset. A manual contour of each dataset was developed. A true positive fraction (TPF) of 88.0 ± 6.8 , 82.0 ± 8.5 , 83.0 ± 4.6 , and 83.3 ± 7.3 was obtained for the simulated, pig, normal volunteer and pathologic datasets, respectively [78].

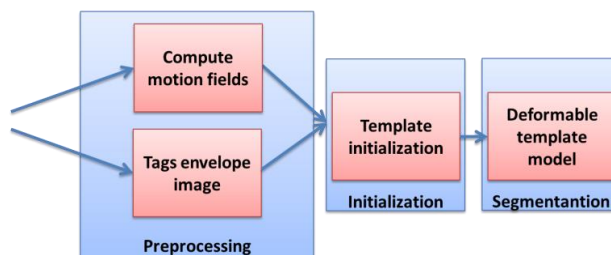


Figure 2.11 - Block scheme for segmentation in t-MRI using the strategy proposed in [78].

Qian *et al.* described another method for tag suppression based on a 2D band-stop filtering technique (Figure 2.12) [83]. The purpose of the band-stop filtering is to attenuate the tag frequency components in the 2D spectrum. The region of the band-stop filtering was designed in such way that it completely suppresses the tags components, but preserves the low and high frequencies as much as possible. To define the filter region, the spectrum is partitioned into several regions around the energy peaks

corresponding to the tag frequencies. A Principle Component Analysis (PCA) is then used to detect the optimal sized 2D asymmetric Gaussian to model the harmonic region. The segmentation is obtained using the deformable model proposed in [84]. The proposed method was applied successfully on more than 150 clinical tagged cardiac MR images acquired with different imaging settings, suggesting this technique to be robust.

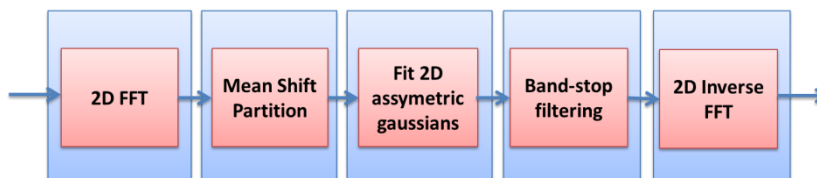


Figure 2.12 - Block scheme for segmentation in t-MRI using the strategy proposed in [83].

Camara *et al.* fuse information from cine-MRI images and t-MRI using image registration (Figure 2.13) [79]. The LV is first segmented on the cine-MRI images as it is easier to detect. The contours are then propagated to the t-MRI image sequence by image registration. In order to successfully register both sequences, the tags in the t-MRI image are first suppressed. The tag suppression is done using a steerable pyramid image decomposition methodology. This type of methods allows a multi-resolution and multi-orientation image decomposition where the analysis could be realized using different supports and orientations. The authors suggest the use of five orientation bands. The oblique orientation coefficients with magnitude above a given threshold are set to zero. The authors compare the presented technique with the methodology based on band stop filters, and conclude that the new strategy leads to a lower computational cost, and is more robust to noise and scale invariant due to the multi-resolution strategy [79].

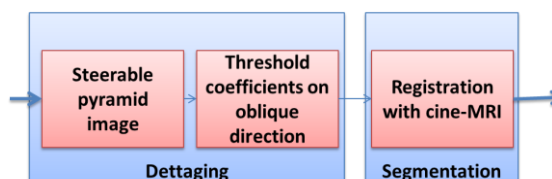


Figure 2.13 - Block scheme for segmentation in t-MRI using the strategy proposed in [89].

2.2.2. LV segmentation on the original t-MRI image

Huang *et al.* developed a framework for learning a joint shape and appearance model for segmentation in t-MRI (see Figure 2.14). The algorithm starts with a global alignment of the training examples under a reference frame. A local registration using *MI* and a gradient descent optimization was applied to solve the dense correspondence problems. To define the features of the statistic shape and appearance model, a PCA

method was applied on the FFD control lattices to capture variations in shape and intensity. The method was applied on 320 images from two 4D t-MRI datasets. A TPF of 97.9% and 96.2% was obtained for the first and second dataset, respectively [80].

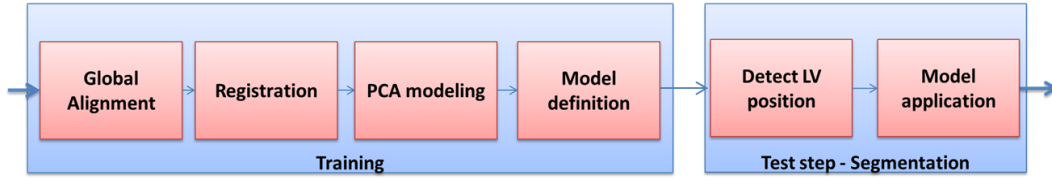


Figure 2.14 - Block scheme for segmentation in t-MRI using the strategy proposed in [80].

Qian *et al.* implemented an active shape model to introduce a priori knowledge in the method (Figure 2.15). An Adaboost classifier was used for the learning step of the segmentation. The method was applied on three datasets acquired from three different patients. The method does not require any human interaction and the authors claim that it is highly accurate [75].

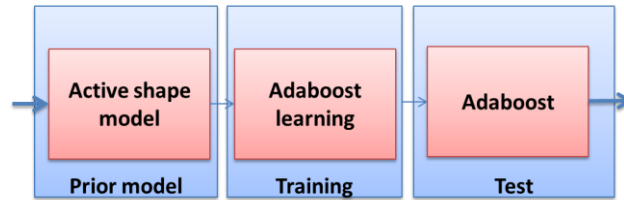


Figure 2.15 - Block scheme for segmentation in t-MRI using the strategy proposed in [75].

2.3. Summary

During this chapter, we explained and discussed the different methods available in literature for LV tracking and segmentation in t-MRI. Based in all the tracking techniques, we focused on image registration approaches, due the high accuracy and high feasibility to estimate the motion field, independently of image properties. It is important to mention, that there are image registration methods where the temporal information is incorporated on the transformation model. The results suggested that these formulations appear to be more accurate.

Regarding the segmentation problem, we can see that some works were proposed during the last years. The comparison between the different techniques is not straightforward, due the difference between the images, the low number of images used during the validation, and the lack of a benchmark datasets. At same time, we observed that a method based on tag suppression followed by a deformable model appear to be the most commonly used technique to segment the LV cavity.

Mathematical Background

3. Mathematical Background

In this chapter, we provide the mathematical background for several topics that will be developed further in the upcoming chapters.

3.1. Motion estimation: Non rigid image registration

Non-rigid registration is an imaging technique that estimates the optimal transformation $T_{fix \rightarrow mov}(\mathbf{r})$ to align each point $\mathbf{r} = [x, y]$ in the moving image (\mathbf{I}_{mov}) with the fixed image (\mathbf{I}_{fix}). Image registration can be defined as a minimization problem:

$$\hat{\mu} = arg \min_{\mu} E(\mu; \mathbf{I}_{fix}; \mathbf{I}_{mov}) \quad (3.1)$$

where E is the cost function and μ is the parameter vector that defines the transformation. To estimate the optimal transformation an iterative process is used, where different parameters are tested (see Figure 3.1). The individual components will be introduced in the next subsections.

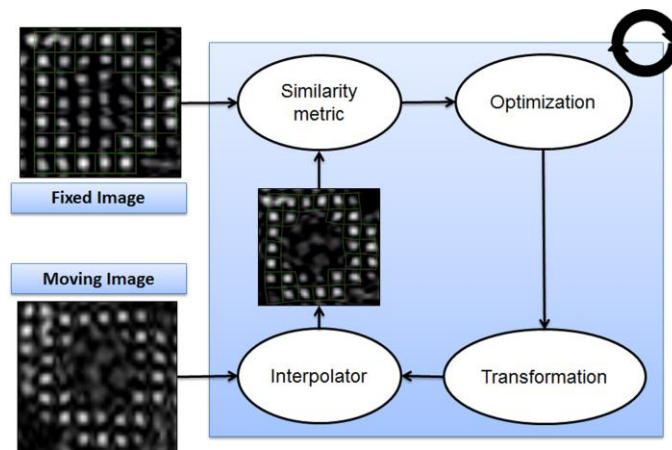


Figure 3.1 - The basic components of the registration framework.

3.1.1. Transformation Model

The transformation model will define all the parameters that describe the motion during the iterative process. In each iteration, a different transformation is applied on the moving image. Since we are using a non-rigid registration methodology, a high number of parameters will be used for the definition of the transformation between the fixed and moving image.

Mathematically, the transformation model (T) represents the displacement field (\mathbf{u}) that we need to apply to the initial position (\mathbf{r}) to achieve the optimal result, and can be formulated as:

$$\mathbf{T}(\mathbf{r}) = \mathbf{r} + \mathbf{u}_{fix \rightarrow mov}(\mathbf{r}) \quad (3.2)$$

In the present work, the displacement field (\mathbf{u}) is described with a two-dimensional third order B-spline tensor-product:

$$\mathbf{u}_{fix \rightarrow mov}(\mathbf{r}) = \sum_{i \in \mathfrak{N}_x} \sum_{j \in \mathfrak{N}_y} \boldsymbol{\mu}^{ij} \beta_x^3 \left(\frac{x - \kappa_x^i}{\sigma_x} \right) \beta_y^3 \left(\frac{y - \kappa_y^j}{\sigma_y} \right) \quad (3.3)$$

with κ_ξ and σ_ξ the control point location and spacing respectively, $\boldsymbol{\mu} = [\mu_x, \mu_y]$ are the parameters of the transformation field and \mathfrak{N}_ξ is the set of control points within the compact support of the B-spline $\beta_\xi(\xi \in [x, y])$. The B-spline tensor product has a local support, which means that the transformation of a point can be computed only from a limited amount of surrounding control points (Figure 3.2). This leads to a computationally efficient algorithm. Additionally, the interpolation nature of the tensor-product B-spline transformation model enforces continuity during the motion estimation, and this naturally leads to an additional smoothness constraint.

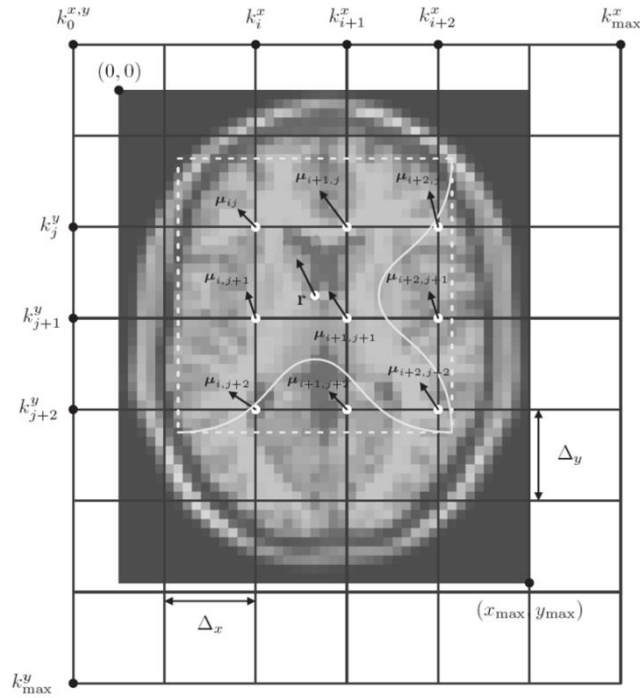


Figure 3.2- B-spline mesh overlaid over the reference image. The transformation parameters $\boldsymbol{\mu}$ are only defined on the mesh knot $\boldsymbol{\kappa}$ [47].

In order to efficiently estimate the optimal transformation, a multi-resolution approach is commonly used (Figure 3.3). In the first level, i.e. at the coarsest level, the transformation uses a high value for the spacing between the control points (σ_ξ). In the

subsequent levels, the value of σ_{ξ} is gradually refined. By using the information from the previous levels, the local deformation can be efficiently defined [85].

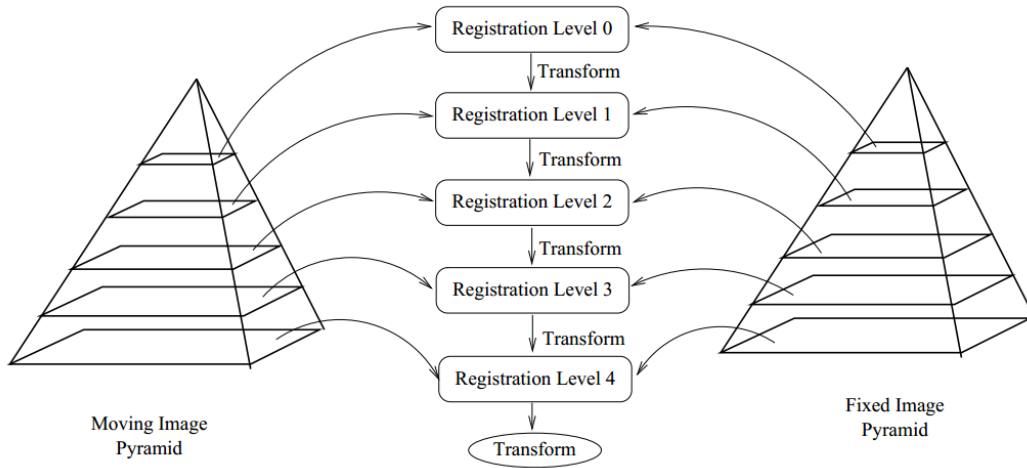


Figure 3.3 - Conceptual representation of the multi-resolution registration process [85].

3.1.2. Cost function

The cost function, which is calculated in each iteration, determines the quality of alignment after applying the current transform on the moving image.

Typically the cost function (E) is defined as:

$$E = SM + \omega R \quad (3.4)$$

where SM is a similarity metric, R a regularization term and ω a term to modulate the influence of the regularization factor.

The SM is the factor responsible to compare the two images and to quantify the differences between them. The metric “drives” the optimization and should be chosen properly based on the properties of the images to be registered. Many metrics exist in literature [85] but in the present work we will focus on the sum-of-square differences (SSD) and mutual information (MI).

3.1.3. Similarity Metrics

Sum-of-squared differences (SSD)

SSD is an intensity-based metric which assumes a linear relationship between the gray levels in the fixed and in the moving image [86]:

$$SSD = \frac{1}{d} \sum_{r \in I_{fix}} [I_{fix}(r) - I_{mov}(T(r))]^2 \quad (3.5)$$

This metric is particularly suited for unimodal image registration problems.

Mutual Information (MI)

MI is a more complex metric based on the calculation of the joint histogram of the images and is useful for both unimodal and multimodal registration problems [86].

MI measures the statistical dependence between two images or equivalently the amount of information that one image contains about the other, without any assumption regarding the relationship between the gray levels in both images [87]. Mathematically, this method computes the statistical dependence between the actual joint intensity probability $p(\mathbf{r}, T(\mathbf{r}))$, in the fixed image (I_{fix}) and moving image (I_{mov}), and the intensity distribution probability in the case of complete independence (marginal distributions) $p(\mathbf{r}) \cdot p(T(\mathbf{r}))$, using the follow expression: [88]

$$MI(I_{fix}, I_{mov}) = \sum_{\mathbf{r} \in I_{fix}} \sum_{T(\mathbf{r}) \in I_{mov}} p(\mathbf{r}; T(\mathbf{r})) \log_2 \frac{p(\mathbf{r}, T(\mathbf{r}))}{p(\mathbf{r}) \cdot p(T(\mathbf{r}))} \quad (3.6)$$

Contrarily to the SSD, where we intend to minimize intensity differences, in the MI approach the optimal transformation is determined when the metric reaches its maximum value. In this case, the equation (3.1) is not applied, and the image registration problem should be formulated as a maximization problem:

$$\hat{\mu} = arg \max_{\mu} E(\mu; I_{fix}; I_{mov}) \quad (3.7)$$

To easily understand how this statistical measure is computed, consider Figure 3.4 where two binary synthetic images A and B are shown (with black corresponding to intensity 0, and white to intensity 1). In this case, the probability of a voxel have a gray level will be $p_A(a)$ and $p_B(b)$, and the joint probability will be defined as $p_{AB}(a; b)$ [86].

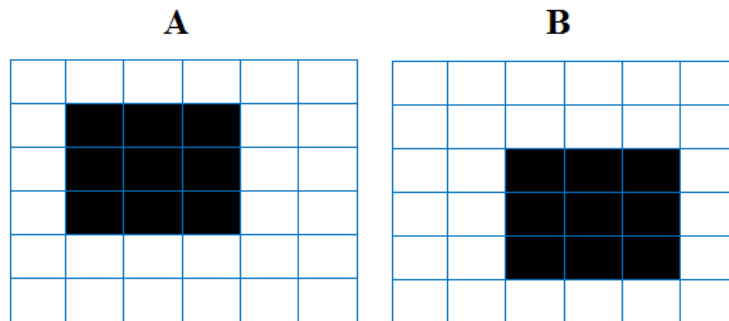


Figure 3.4 - Binary synthetic image. The black squares represent 0, and the white represent 1.

In this specific case, $p_A(0) = \frac{1}{4}$, $p_A(1) = \frac{3}{4}$, and $p_B(0) = \frac{1}{4}$, $p_B(1) = \frac{3}{4}$. In terms of joint probabilities $p_{AB}(0; 0) = \frac{4}{36}$, $p_{AB}(1; 0) = \frac{5}{36}$, $p_{AB}(0; 1) = \frac{5}{36}$ and

$p_{AB}(1; 1) = \frac{22}{36}$. Based on these values, and using equation (3.6), the value of MI for this pair of images will be:

$$MI = \frac{4}{36} \log_2 \frac{4/36}{1/4 * 1/4} + \frac{5}{36} \log_2 \frac{5/36}{3/4 * 1/4} + \frac{5}{36} \log_2 \frac{5/36}{3/4 * 1/4} + \frac{22}{36} \log_2 \frac{22/36}{3/4 * 3/4} = 0.045$$

In practice, the joint probability distribution $p(\mathbf{r}; \mathbf{T}(\mathbf{r}))$ is estimated using the joint histogram (Figure 3.5). The joint histogram can be defined as a function of two variables, where one variable/axis represents the gray levels intensity in the fixed image and the other, the gray levels intensity in the moving image. Each coordinate on the histogram represents the number of points with the same pair of intensities in the fixed and the moving image [89].

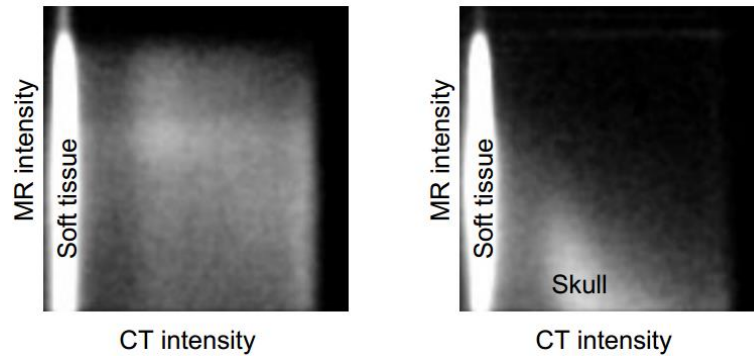


Figure 3.5 - Joint histogram used in a registration problem between a CT and MR example [87].

Typically, for a more efficient computation, the joint histogram uses ranges to combine the different gray levels (termed bins). This process is essential due the high number of intensities commonly presented in medical imaging. A large number of different intensities will generate quite large matrices, which would imply a high computational cost. At the same time, the bins approach prevents a quite sparse histogram, which will affect the performance of the metric. During the current master thesis, 32 bins are used to compute the joint histogram.

Based on the initial formulation of the mutual information in [87], other related metrics where proposed. In this project, we will focus on the Mattes Mutual Information (MMI) [90] and the Normalized Mutual Information (NMI) [91].

Mattes Mutual Information (MMI)

MMI computes the metric based on the equation (3.6), but the computation of the joint and marginal probabilities are based on a B-spline parzen window. The B-spline parzen window is defined as [92]:

$$p(\mathbf{r}, \mathbf{T}(\mathbf{r})) = \frac{1}{N} \sum_{\mathbf{x}_i \in N} \omega_F(\mathbf{r}/\sigma_F - \mathbf{I}_{fix}(\mathbf{x}_i)/\sigma_F) \times \omega_M(\mathbf{T}(\mathbf{r})/\sigma_M - \mathbf{I}_{mov}(\mathbf{T}(\mathbf{x}_i))/\sigma_M) \quad (3.8)$$

with N the number total of pixels, ω_F and ω_M representing the fixed and moving B-spline parzen windows; σ_F and σ_M scaling factors that must be equal to the intensity bin widths.

The B-spline parzen window (Figure 3.6) is essentially a data interpolation technique to estimate a continuous probability density function from which the samples were derived. This methodology is typically used to reduce the high computational time associated with the joint histogram calculation [85].

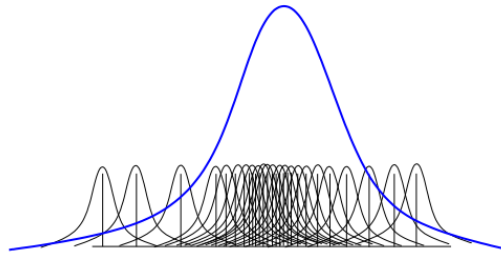


Figure 3.6 - Parzen Window (blue), constructed by superimposing kernel functions centered on the samples of the image [85].

Normalized Mutual Information (NMI)

The *NMI* uses the principles proposed in [87], but with a different formulation during the computation of the metric (see equation 3.9). As in *MMI*, to improve the computation time, a B-spline parzen window is used to compute the joint and marginal probabilities [92].

Mathematically, the *NMI* is defined as [92]:

$$\begin{aligned} NMI(\mathbf{I}_{fix}, \mathbf{I}_{mov}) &= \frac{\sum_{\mathbf{r} \in \mathbf{I}_{fix}} p(\mathbf{r}) \log_2(p(\mathbf{r})) + \sum_{\mathbf{T}(\mathbf{r}) \in \mathbf{I}_{mov}} p(\mathbf{T}(\mathbf{r})) \log_2(p(\mathbf{T}(\mathbf{r})))}{\sum_{\mathbf{T}(\mathbf{r}) \in \mathbf{I}_{mov}} \sum_{\mathbf{r} \in \mathbf{I}_{fix}} p(\mathbf{r}, \mathbf{T}(\mathbf{r})) \log_2(p(\mathbf{r}, \mathbf{T}(\mathbf{r})))} \\ &= \frac{\sum_{\mathbf{T}(\mathbf{r}) \in \mathbf{I}_{mov}} \sum_{\mathbf{r} \in \mathbf{I}_{fix}} p(\mathbf{r}, \mathbf{T}(\mathbf{r})) \log_2(p(\mathbf{r}) \cdot p(\mathbf{T}(\mathbf{r})))}{\sum_{\mathbf{T}(\mathbf{r}) \in \mathbf{I}_{mov}} \sum_{\mathbf{r} \in \mathbf{I}_{fix}} p(\mathbf{r}, \mathbf{T}(\mathbf{r})) \log_2(p(\mathbf{r}, \mathbf{T}(\mathbf{r})))} \end{aligned} \quad (3.9)$$

3.1.4. Regularization Term

As indicated in equation (3.4), the cost function is based on a similarity measure and a regularization factor.

The regularization term is used to prevent non-physical deformation (Figure 3.7). Due to the high number of DOFs, this constraint should be used to guarantee a smooth motion. It is important to mention that the B-spline tensor transformation model already imposes a certain degree of smoothness in the transformation field.

Several regularization techniques are available in the literature [85, 92], but in the present work we focus on the bending energy (BE) method proposed by Rueckert *et al.* [69]. It is based on the bending energy of a thin sheet of metal and is defined as:

$$\left\| \frac{\partial^2 \mathbf{T}(\mathbf{r})}{\partial(\mathbf{r})^2} \right\| = \sum_{\xi \in (x,y)} \left(\frac{\partial^2 T_\xi}{\partial x^2}(\mathbf{r}) \right)^2 + \left(\frac{\partial^2 T_\xi}{\partial y^2}(\mathbf{r}) \right)^2 + 2 \left(\frac{\partial^2 T_\xi}{\partial x \partial y}(\mathbf{r}) \right)^2 \quad (3.10)$$

with $\mathbf{T}=[T_x, T_y]$ the transformation vector and \mathbf{r} representing each point in the reference image and $\xi \in [x, y]$.

Equation (3.10) will sum all the components of the Jacobian in all the directions. Since we aim for a smooth motion, this value should be always low. In case of a non-physical deformation (Figure 3.7b) the value of the regularization will be high. This will result in a high value of the cost function. As such, this solution will be discarded, since we intend to minimize the cost function (in the case of *SSD*).

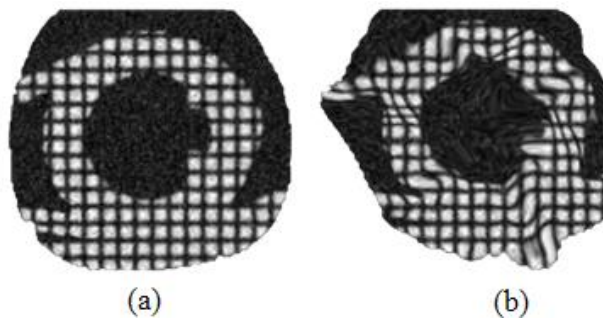


Figure 3.7 - Regularization effect. (a) Normal registration result, (b) Non-physical deformation.

3.1.5. Optimization

Ideally, all parameters combinations should be tested to identify the optimal solution, but in practice this is not possible, due to the large set of possibilities. To solve this limitation, optimizers are typically used.

The optimization block will lead the iterative process to minimize the cost function, and define the changes that should be applied on the parameters to rapidly

detect the optimal result. In general, the optimizer will update the parameters using the following strategy [93]:

$$\boldsymbol{\mu}^{k+1} = \boldsymbol{\mu}^k + a^k \mathbf{d}^k \quad (3.11)$$

where \mathbf{d}^k is the search direction at iteration k , and a^k is a scalar gain factor controlling the step size along the search direction.

Based on this description, it is evident that an intensive computation time is associated with the optimizer block. Optimizers can be categorized into non-gradient methods (Powell and simplex methods) and gradient approaches (gradient descent, conjugate gradient, quasi-newton and Levenberg-Marquardt methods) [85, 93]. In the current work, we chose the limited memory Broyden Fletcher Goldfarb Shannon optimizer with simple bounds (LBFGSB), because of its good performance for optimize a large amount of parameters while also eliminate the need for storing the inverse of the Hessian matrix during the routine [94]. The optimization step of the LBFGSB optimizer can be defined by adapting equation (3.11) to:

$$\boldsymbol{\mu}^{k+1} = \boldsymbol{\mu}^k - a^k L^k \frac{\partial E}{\partial \boldsymbol{\mu}^k} \quad (3.12)$$

where a^k is a scalar gain factor controlling the step size along the search direction and L^k is an approximation to the inverse of the Hessian matrix.

3.1.6. Image interpolators

During the iterative process and based on the transformation applied on the images, some points can be mapped to a non-grid position. In this case, an interpolation method is used to assess the image intensity and map the point to a valid position. The interpolation method, affects the overall computation time, given that this interpolation step is executed thousands of times during each iteration [85].

The most common interpolation schemes are nearest neighbor, linear interpolation and B-spline interpolation (Figure 3.8) [85].

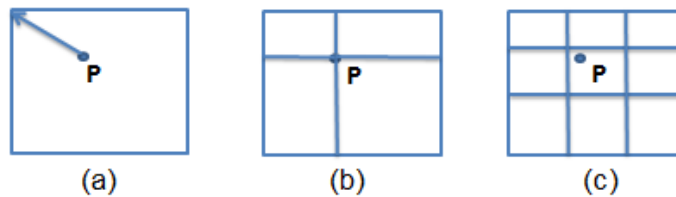


Figure 3.8 - Interpolators. a) Nearest neighbor, b) Linear, c) B-spline.

The nearest neighbor simply uses the intensity of the nearest grid position to calculate the intensity of the point. It is fast in terms of computational time, but assumes that the image intensity is constant [85].

The linear interpolation scheme assumes that the intensity varies linearly between the grid positions [85].

The B-spline interpolator represents the image intensity using B-spline basis functions. The intensity at non-grid positions is computed by multiplying the B-spline coefficients with shifted B-spline kernels within a small support region of the request position. Since the smoothing effect is intrinsic to B-splines, this approach assures a higher smoothing effect during the computation of the intensity of the point, but with a higher computational cost compared to linear and nearest neighbor interpolation [85].

During this project, we choose linear interpolation, since it consists of a good trade-off between computational time and accuracy [85, 92].

Finally, for more details about the image registration, we recommend the PhD thesis from Dirk Loeckx (KULeuven) [47], the PhD thesis from Brecht Heyde (KULeuven) [95] and the ITK manual [85] or the elastix manual [92].

3.1.7. Traditional motion estimation scheme: sequential 2D FFD formulation

Using the tools presented above, one can formulate a sequential 2D FFD scheme to estimate motion from an image sequence. This subsection describes the implementation of Heyde *et al.* [96], which was previously applied on the study of the regional heart strain and deformation in echocardiography.

In this framework a pairwise scheme between two consecutive frames f and $f+1$ is considered (Figure 3.9) to compute the motion field during the cardiac cycle.

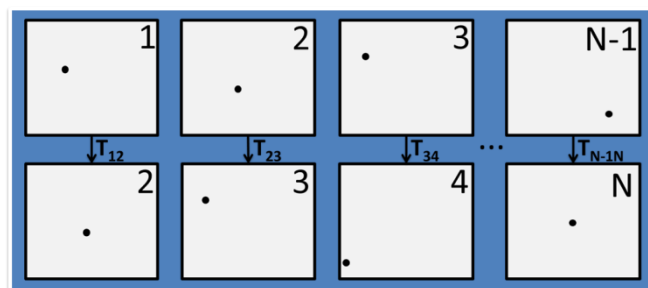


Figure 3.9 - Sequential 2D formulation [96].

In this case, the transformation and deformation field that represent the difference between the two consecutives frames can be expressed similar to the equations (3.2 and 3.3).

$$\mathbf{T}(\mathbf{r}) = \mathbf{r} + \mathbf{u}_{f \rightarrow f+1}(\mathbf{r}) \quad (3.13)$$

$$\mathbf{u}_{f \rightarrow f+1}(\mathbf{r}) = \sum_{i \in \mathbb{N}_x} \sum_{j \in \mathbb{N}_y} \mu^{ij} \beta_x^3 \left(\frac{x - \kappa_x^i}{\sigma_x} \right) \beta_y^3 \left(\frac{y - \kappa_y^j}{\sigma_y} \right) \quad (3.14)$$

The optimal inter-frame transformation field was estimated iteratively with a LBFGSB optimizer [94], by minimizing the cost function (E) defined as:

$$E = \frac{1}{d} \sum_{\mathbf{r} \in I_f} [I_f(\mathbf{r}) - I_{f+1}(\mathbf{T}(\mathbf{r}))]^2 + \frac{\omega_{BE}}{d} \sum_{\mathbf{r} \in I_f} \left\| \frac{\partial^2 \mathbf{T}(\mathbf{r})}{\partial^2 \mathbf{r}} \right\|^2 \quad (3.15)$$

with d the number of points \mathbf{r} , and ω_{BE} a factor to modulate the influence of the BE penalty [69]. The LBFGSB uses the optimization step of equation (3.12).

In their implementation an isotropic grid spacing was used with 3 scales (multi-resolution approach), while halving the spacing in the spatial direction at every scale.

3.2. Image Segmentation

3.2.1. Active Contours

Active contours are a class of deformable models where an optimization problem is proposed to segment the object shape in a target image (Figure 3.10) [44]. An energy minimization function is used, where prior knowledge about the target can be added to guide the proposed model during the iterative phase [33].

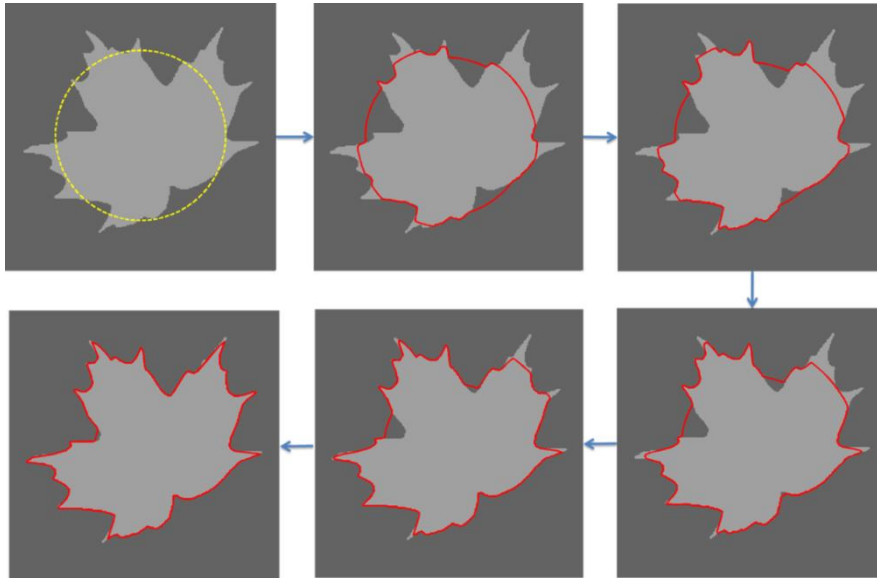


Figure 3.10 - Active contours propagation. The dashed yellow line is the initialization.

Active contours need to be initialized to a given shape (Figure 3.10). This is also the major drawback since misinitialization can easily guide the propagation of the contour towards an undesirable result [97]. Two categories of active contours can be distinguished, depending on the definition of the energy function: the edge-based [98] and the region-based approaches [97, 98].

The edge-based approaches use the gradient of the image (Figure 3.11a) to detect the object boundaries and limit the iterative approach during the model propagation. Given that a high number of interfaces can be detected using the gradient of the image, initialization plays a crucial role. This method is also sensitive to image noise. On the other hand, the region-based methods use a statistical model, based on the image intensity, for the definition of the background and the foreground. Typically, the best results are achieved if a regional assessment is used instead of a global image assessment (Figure 3.11b) [97].

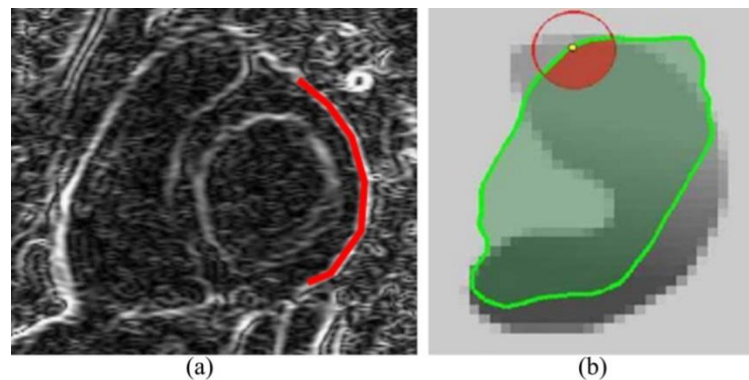


Figure 3.11 - a) Gradient of the image used in edge based approach, b) Regional assessment of the intensity for the definition of the statistically model used in region based methods [97].

The region-based methods are less dependent on the initialization and the image noise, but the segmentation of the objects with high heterogeneity are challenging (Figure 3.12) [97].

Finally, the evolution model is the optimization or the energy minimization step [33]. For the definition of the energy, several factors as elasticity term, curvature term, smoothing term, etc, are normally added to regularize the contour and help to detect the optimal result.

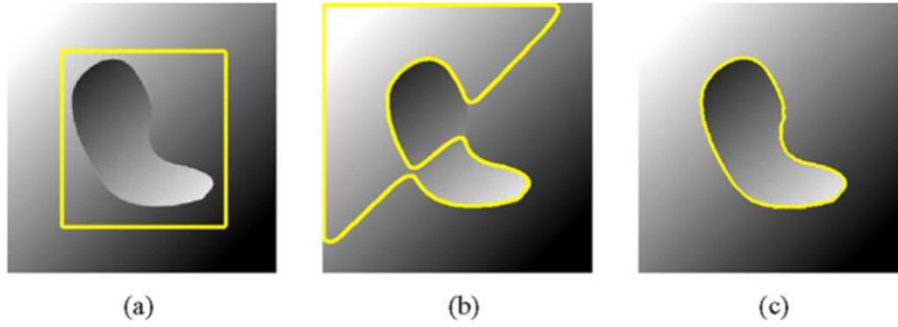


Figure 3.12 - Synthetic image presented in [97] . (a) initialization, (b) unsuccessful result of region-based segmentation, (c) successful result of edge-based segmentation technique [97].

3.2.2. B-spline Explicit Active Surfaces

The BEAS framework was proposed by Barbosa *et al.* in 2012 [44], with the key novelty being the formulation of the interface as an explicit function. Geometrically, this implies that one of the coordinates of the points of the interface, $x = x_1, \dots, x_n$, is expressed as a function of the remaining coordinates, i.e. $x_1 = \psi(x_2, \dots, x_n)$. Such explicit formulation allows reducing the dimensionality of the segmentation problem.

Inspired by the work presented by Bernard *et al.* [99], Barbosa *et al.* [44] defined the interface (ψ) as a linear combination of B-splines basis functions:

$$x_1 = \psi(x_2, \dots, x_n) = \sum_{\mathbf{k} \in \mathbb{Z}^{n-1}} c[\mathbf{k}] \beta^d \left(\frac{\mathbf{x}^*}{h} - \mathbf{k} \right) \quad (3.16)$$

where $\beta^d(\cdot)$ is the uniform symmetric (n-1) dimension B-spline of degree d . The knots of the B-splines are located on a regular grid defined on the chosen coordinate system, with a scale given by h . The coefficients of the B-spline are defined by $c[\mathbf{k}]$. By using the geometric functions and the B-spline formulation [44], a smooth interface can be calculated in an efficient manner, allowing to achieve real-time computation even for 3D segmentation problems.

Following the principles of active contours, the BEAS framework can handle both global and localized region-based energy formulations. The first is based on the method proposed by Chan-Vese [100]. However, given that BEAS is based on B-splines, the authors are intrinsically adding a regularization term, which is an advantage over the initial Chan-Vese formulation. The second type of energies is based on the work of Lankton and Tannenbaum [97]. To maintain a low computational cost, Barbosa *et al.* [44] added a restriction on the region size used for the computation of the localized energy.

BEAS was originally used for real-time segmentation of the endocardium in 3D ultrasound data. An extension of the method was proposed by Queirós *et al.* [33], where both endo- and epicardial contours were modeled as a combination of two explicit functions. Mathematically, each interface (Γ) was modeled as:

$$\Gamma_{endo}(\theta) = \psi_{w_P}(\theta) - \psi_{w_T}(\theta) \quad (3.17)$$

$$\Gamma_{epi}(\theta) = \psi_{w_P}(\theta) + \psi_{w_T}(\theta) \quad (3.18)$$

where $\psi_{w_P}(\theta)$ represents the center position of the myocardial wall as a function of θ and $\psi_{w_T}(\theta)$ encodes half of the myocardial wall thickness. This formulation divides the image space into three regions, namely the blood pool, the myocardium and outer structures. Moreover, since both contours are coupled, the optimal position is estimated simultaneously. Finally, the application of different B-spline scales for ψ_{w_P} and ψ_{w_T} , gives two degrees of freedom during segmentation, allowing separate smoothing of the local variation of the myocardial position and thickness [33].

Regarding the used energy function, Queirós *et al.* chose the localized Chan-Vese energy and added weights for each region of the interface, in order to push the contours towards (or away) from the myocardium and surpass the problem of trabeculae and papillary muscles. Moreover, Queirós *et al.* added a combined global and local formulation of the myocardium, taking advantage of the homogeneity of the myocardium and increasing the robustness against initialization [33].

Based on the coupled segmentation, the resulting energy is formulated as:

$$E = \int_{\Gamma_{endo}} f_{in}(\mathbf{x}^*)H_{\phi_{endo}}(\mathbf{x}^*) + f_{myo}(\mathbf{x}^*)\left(1 - H_{\phi_{endo}}(\mathbf{x}^*)\right) d\mathbf{x}^* \quad (3.19)$$

$$+ \int_{\Gamma_{epi}} f_{myo}(\mathbf{x}^*)H_{\phi_{epi}}(\mathbf{x}^*) + f_{out}(\mathbf{x}^*)\left(1 - H_{\phi_{epi}}(\mathbf{x}^*)\right) d\mathbf{x}^*$$

where,

$$f_{in}(\mathbf{x}^*) = \omega_{in} \cdot (I(\mathbf{x}^*) - u_{x,in})^2 \quad (3.20)$$

$$f_{myo}(\mathbf{x}^*) = \omega_{myo} \cdot (I(\mathbf{x}^*) - u_{gl,myo})^2 \quad (3.21)$$

$$f_{out}(\mathbf{x}^*) = \omega_{out} \cdot (I(\mathbf{x}^*) - u_{x,out})^2 \quad (3.22)$$

and ω_{in} , ω_{myo} and ω_{out} are the scalar weight applied on each region, $u_{x,in}$ and $u_{x,out}$ represent the local intensity means in the vicinity of the x for the inner and outer regions. $u_{gl,myo}$ corresponds to the value $u_{gl,myo} = (u_{x,myo} + u_{g,myo})/2$, which represents mean local intensity of the myocardium ($u_{x,myo}$) and the mean global

intensity estimated using the entire myocardium ($u_{g,myo}$). H_{ϕ_j} is the Heaviside operator applied to the level-set like function ϕ_j [33].

Based on the energy minimization derivation presented in Barbosa *et al.* [44] and applied by Queirós *et al.*[33], the evolution equations are represented as:

$$\frac{\partial E}{\partial c_{W_P}[k]} = \int_{\Gamma_{endo}} g_{endo}(\mathbf{x}^*) \beta^d \left(\frac{\mathbf{x}^*}{h} - \mathbf{k} \right) d\mathbf{x}^* + \int_{\Gamma_{epi}} g_{epi}(\mathbf{x}^*) \beta^d \left(\frac{\mathbf{x}^*}{h} - \mathbf{k} \right) d\mathbf{x}^* \quad (3.23)$$

$$\frac{\partial E}{\partial c_{W_T}[k]} = - \int_{\Gamma_{endo}} g_{endo}(\mathbf{x}^*) \beta^d \left(\frac{\mathbf{x}^*}{h} - \mathbf{k} \right) d\mathbf{x}^* + \int_{\Gamma_{epi}} g_{epi}(\mathbf{x}^*) \beta^d \left(\frac{\mathbf{x}^*}{h} - \mathbf{k} \right) d\mathbf{x}^* \quad (3.24)$$

with,

$$g_{endo}(\mathbf{x}^*) = f_{in}(\mathbf{x}^*) - f_{myo}(\mathbf{x}^*) \quad (3.25)$$

$$g_{epi}(\mathbf{x}^*) = f_{myo}(\mathbf{x}^*) - f_{out}(\mathbf{x}^*) \quad (3.26)$$

For more details about this framework, we recommend the original paper from Barbosa *et al.* [44], the PhD thesis from Daniel Barbosa (KULeuven) [101] and the master thesis from Sandro Queirós (University of Minho) [102].

3.3. Improving the initialization: template matching

One drawback in active contour approaches is associated with the required initialization process. In this section we will describe an interesting approach, called template matching, for a first estimation of the endo- and epicardial contours.

The template matching techniques are useful tool for the detection of pre-defined patterns on the image, based on the profile of different regions or the intensity variation on the image [103]. These methodologies use the principle of block matching search, and can be defined as an optimization problem, where the maximum correlation between a region of the image and a template is searched.

In terms of LV delineation, some assumptions are normally used. First, the anatomic structure has an elliptical or a circular shape and, secondly, the myocardium has a dark appearance when compared to the blood pool. Based on this knowledge, template matching approaches were previously proposed for the estimation of the both contours, endocardium and epicardium, in cine MRI images [33, 104].

Queirós *et al.* [33] proposed a new template matching strategy with low computational time and high feasibility demonstrated in a MICCAI database of, 45 cine-MRI datasets. This work, which is an evolution of the method proposed by Ciofolo

et al.[104], uses an affine transformation to estimate elliptical templates, instead of circular ring templates only (proposed on the original methodology). This affine transformation is essential and improves the robustness of the template matching, since the LV frequently presents an elliptical shape.

The method proposed by Queirós *et al.* creates several kernels with different possible shapes, thicknesses and sizes of the myocardium (Figure 3.13a). These kernels are formed based on a first initialization of the template, where 3 variations of the value in radii, 4 variation of the standard deviations (related with the wall thickness), 5 orientations are used (0° , $\pm 45^\circ$ and $\pm 90^\circ$), and 4 axis ratios. In total, 240 kernels are considered for the block matching approach. During the optimization problem, this method uses the normalized cross correlation to detect the optimal result between the region of the image and a given template (Figure 3.13b). The best template (Figure 3.13c) will define the optimal center, orientation, radius and axes ratio for a first estimation of the endocardial and epicardial contours (Figure 3.13d).

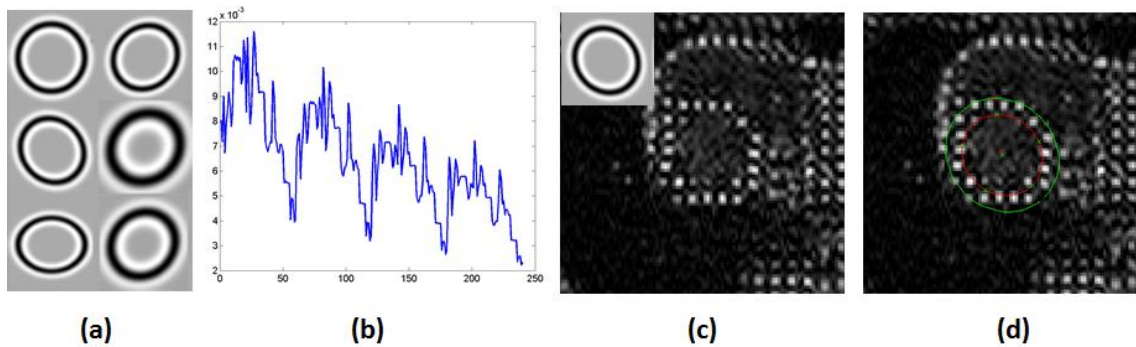


Figure 3.13 - Template matching methodology proposed in [33]. (a) Design of various kernels to use as templates, (b) optimization problem to detect the optimal template, (c) original image and optimal template, (d) original image and first estimation of the contours.

3.4. Application: the BEAS threshold algorithm

The template matching requires an initial template, based on certain parameters, such as radii, standard deviation and orientation. If these parameters are similar to the real properties of the myocardium, the performance of the template matching will improve significantly.

The BEAS threshold is a region growing algorithm capable to estimate with high accuracy the properties of the endo- and epicardial contours, thus being a useful tool to define the parameters of the initial template. This method was proposed in the master thesis of Sandro Queirós (Univeristy of Minho) [102]. The advantage of this method is

the low computational time, the smoothing on the contours during the iterative process and the correction of the center of the heart in each iteration.

The method needs a threshold to limit the evolving process. In the original work, an expectation maximization algorithm for an automatic definition of this threshold is applied. In this case, the algorithm was applied in gray images, and therefore an adaptive threshold should be used, based on the image properties.

Regarding the region growing formulation, this method works as an iterative process. Initially, the algorithm creates a small radius based on a pre-defined center position (Figure 3.14a) and evolves the contours using the threshold. In that step, if the intensity signal at the current position of a contour point is higher than the threshold, the contour grows. In the inverse situation, the contour shrinks (Figure 3.14b).

The algorithm also estimates a new center of the contour in each iteration (Figure 3.14c, where the green point is the new center point estimation based on the contour's center of gravity and the blue point represents the original center point used on the first iteration) and re-initializes the contour. The method only stops when the area enclosed by the contour does not significantly change for a few iterations (Figure 3.14d).

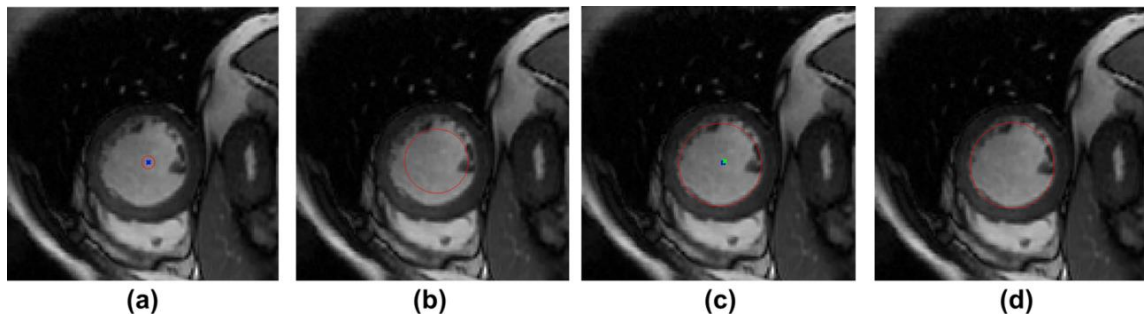


Figure 3.14 - Region growing based on BEAS framework. (a) Initialization of the algorithm using a pre-defined center position, (b) Contour evolution, (c) Optimal solution, where is possible to see a difference between the initial center position (blue point) and the new center position (green point), (d) optimal solution.

3.5. Evaluating image segmentation quality

The computation of metrics to assess the differences between a manual contour and automatic contour is typically performed using the Dice metric, the average perpendicular distance (APD) and the Hausdorff distance [105].

The Dice metric [106] measures the similarity between the two used contours, by the computation of the area overlap. A range between [0-1] is then obtained, with the

maximum value implying total correspondence and the minimum value implying that no relation between the two areas exists. This metric can be computed as:

$$Dice = \frac{2A_{Int}}{A_1 + A_2} \quad (3.27)$$

with A_{Int} , A_1 and A_2 representing the intersection area, the area of the first contour and the area of the second contour.

The APD value represents the mean value of the perpendicular distance between the two contours, calculated over all points. As such, the lower the APD value, the better correspondence between both contours.

Finally, the Hausdorff distance is the maximum perpendicular distance between contours, which indicates the maximum local error.

As a last comment, it is important to mention that these metrics are applied separately for the endocardial and epicardial contours.

3.6. Strain estimation

During this master thesis, the principal objective is the study of the deformation of the heart. For this study, two important clinical indicators, related of the heart function, are the radial and circumferential strains. The radial direction its perpendicular to the epicardium, pointing outwards and the circumferential direction is perpendicular to the radial direction (Figure 3.15) [107]. In terms of normal values, the normal radial strain has a value between 46-80% and the normal circumferential strains shows a negative value (the negative value is used by convention) [108]. It's important to mention that during the computation of these two strains, a definition of the endocardial and epicardial contours is required.

Figure 3.15 shows an overview of the technique used to compute the strain. With this method, we intend to calculate the regional deformation for a set of points positioned within the myocardial walls, using the methodology proposed by Heyde *et al.* [13]. These points are defined in the ED frame, and will be propagated, during the cardiac motion, based on the optimal transformation obtained during the registration.

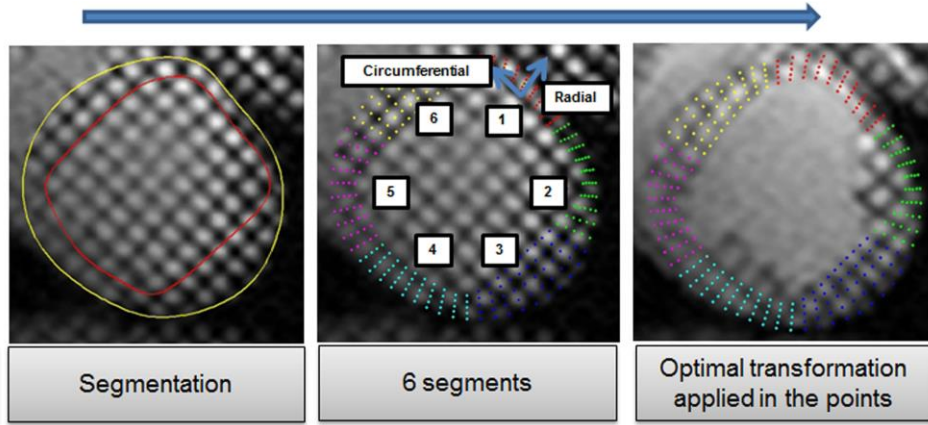


Figure 3.15 - Estimation of the radial and circumferential strain.

In each segment, 5 and 10 points are used in the radial and circumferential direction, respectively. The displacement of this set of points relative to the initial position is then found by cumulating the transformation fields (Figure 3.16).

In the sequential 2D formulation [96], the pairwise transforms ($T_{f \rightarrow f+1}$) were cumulated as:

$$T_{ED \rightarrow f}(\mathbf{r}) = T_{f-1 \rightarrow f}(\mathbf{r}) \circ \dots \circ T_{2 \rightarrow 3}(\mathbf{r}) \circ T_{ED \rightarrow 2}(\mathbf{r}) \quad (3.28)$$

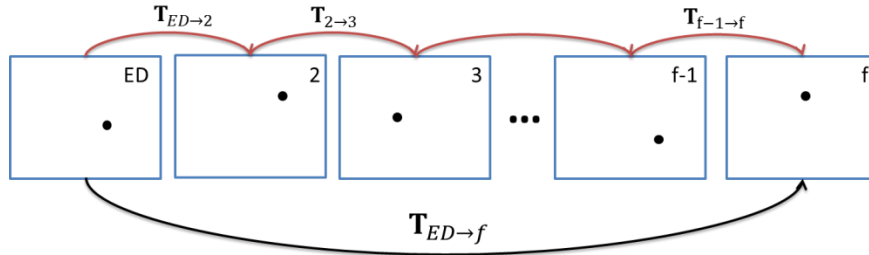


Figure 3.16 - Displacement computation from the frame f to ED based on the optimal alignment.

The differences between the motions of these points are used to compute the strain value ε_N using:

$$\varepsilon_N(t) = \frac{D_N(t) - D_N(0)}{D_N(0)} \quad (3.29)$$

where $D_N(t)$ is the distance between two adjacent sample points in either the radial or circumferential direction at time t , and similarly $D_N(0)$ being the respective initial distance [107].

The equation (3.29) represents the distance between points at the time t when compared with the distance at the initial (undeformed) state [107] (Figure 3.17).

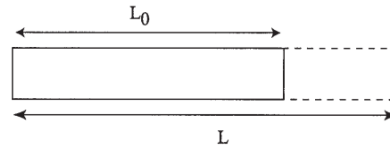


Figure 3.17 - Strain of a one-dimensional object is limited to lengthening or shortening. Strain is the deformation of an object relative to its original shape [107].

An alternative formulation of the strain is based on continuum mechanics theory [109]. The strain along a certain direction at each time t can be estimated as [110]:

$$\epsilon_N = \frac{\|dx\|}{\|dX\|} - 1 = \sqrt{N^T \cdot F^T \cdot F \cdot N} \quad (3.30)$$

where dX is an arbitrary material line segment which is deformed to dx . N corresponds to a unit vector representing the strain direction and F is the spatial gradient of the transformation field, and is thus given by the Jacobian matrix of the transformation field [109, 110].

Normally, in MRI studies, only SA acquisitions are used. The heart performance is typically studied using the 16 model proposed by Cerqueira *et al.* [111], where three slices are assessed and divided in different segments. The apical slice is acquired near the apex of the heart; the mid slice is obtained in the middle position of the cardiac structure; and the basal slice is acquired near the base of the heart (see Figure 1.5). Each slice has different properties (e.g. shape and dimension), and different number of segments should be used in the study. The authors of the work in [111] mention that in the apical slice the myocardium should be divided in 4 segments, while in the remaining slices 6 segments should be used (Figure 3.18).

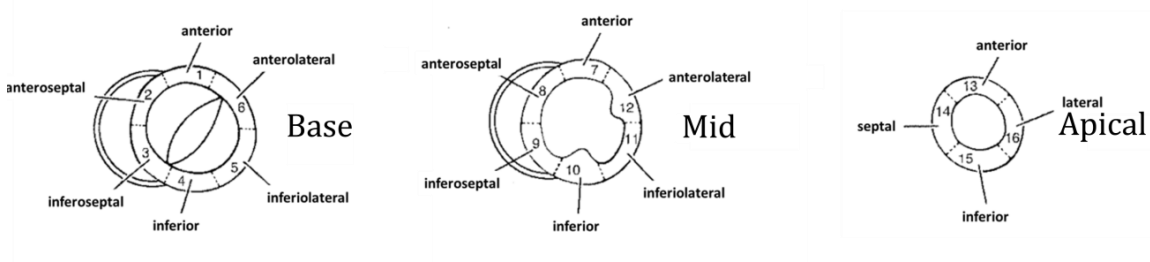


Figure 3.18 – Definition of the segments in the basal, mid and apical slice [111].

Methodology

4. Methodology

In this chapter, an automatic method is proposed to investigate regional cardiac function from short-axis t-MRI images.

4.1. Overview

The proposed method uses several steps as shown schematically in Figure 4.1.

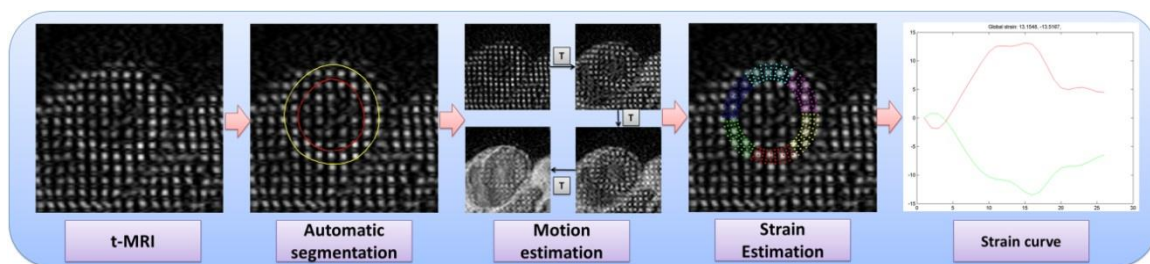


Figure 4.1 – Proposed automatic framework to study cardiac deformation. “T” means tracking.

LV contouring for strain estimation on t-MRI images is challenging due to the lack of contrast between the myocardial borders and the blood pool at the beginning of the cardiac cycle. We therefore focused first on the development of an automatic segmentation strategy. In this work we adapt the BEAS framework, which was previously shown successfully on 3D US images [44] and cine-MRI [33] images. For this purpose, an efficient pre-processing strategy to suppress the tags is first proposed.

Next, motion between subsequent frames is estimated by applying non-rigid image registration techniques. A novel registration technique is proposed by including the temporal information directly in the framework.

Finally, by using the obtained motion field, the myocardial contour can then be propagated over time and regional myocardial strain can be extracted.

4.2. Automatic myocardial segmentation

4.2.1. Overview

In this section, the methodology developed for automatic LV contouring in t-MRI images is described.

As mentioned in section 2.2, a common strategy to segment t-MRI images is to first suppress the tags, followed by an active contour segmentation to define the boundaries [17].

Figure 4.2 schematically shows the data flow to automatically segment the myocardium.

Given that the blood pool contains tags in the initial ED frame, and given that the tags fade over the cardiac cycle, we propose to use the 4th frame (see Appendix I, Figure 10.1) of the sequence to segment the myocardium (see Figure 4.2A). Since we are interested in cardiac strain with respect to ED, a strategy to propagate the myocardial contour between the 4th frame and ED frame is required. This strategy will be described in section 4.4.1.

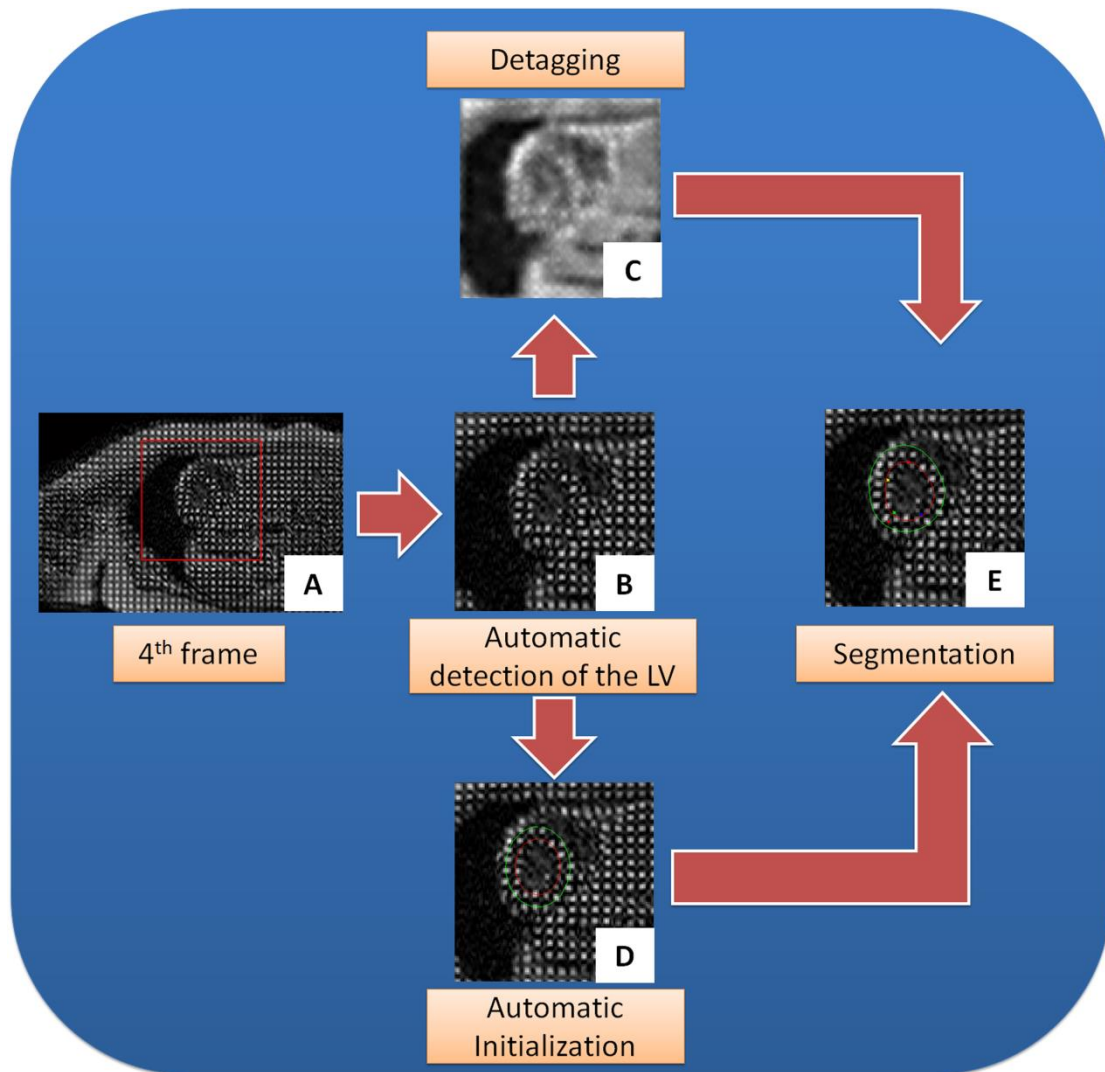


Figure 4.2 - Scheme used for automatic segmentation of LV in t-MRI images.

The strategy used to segment the myocardium consists of the following steps: (i) starting from the 4th frame, we automatically detect the LV and define a ROI (see Figure 4.2B). This is then used as input to (ii) detag the images based on spectral analysis (see Figure 4.2C) and (iii) automatically initialize BEAS based on template matching (see Figure 4.2D); (iv) Finally, BEAS is then used to define endo- and epicardial borders (see Figure 4.2E).

4.2.2. Automatic detection of the LV

In order to automatically detect the LV, several consecutive steps were performed. These were inspired by the techniques of several papers found in literature [112-114]. In the end of this strategy, a ROI will be defined where the LV is positioned in the center of the image. At the same time, we will reduce the region used in the next steps. This last factor is essential during the computation of the FFT, since the tags are in the whole image. Using this ROI, the spectrum will more easily show the LV tag frequencies.

Computation of the variance over the cardiac cycle

First, Cocosco *et al.* [112] suggested that the intensity variance over the cardiac cycle, can be used to detect the myocardium. Since tags deform with the myocardium, a high variance indicates the position of the myocardium. In the current approach, we computed the variance between frame number 4 and 8 (Figure 4.3A). We are using a limited amount of frames due to the effect of tag fading.

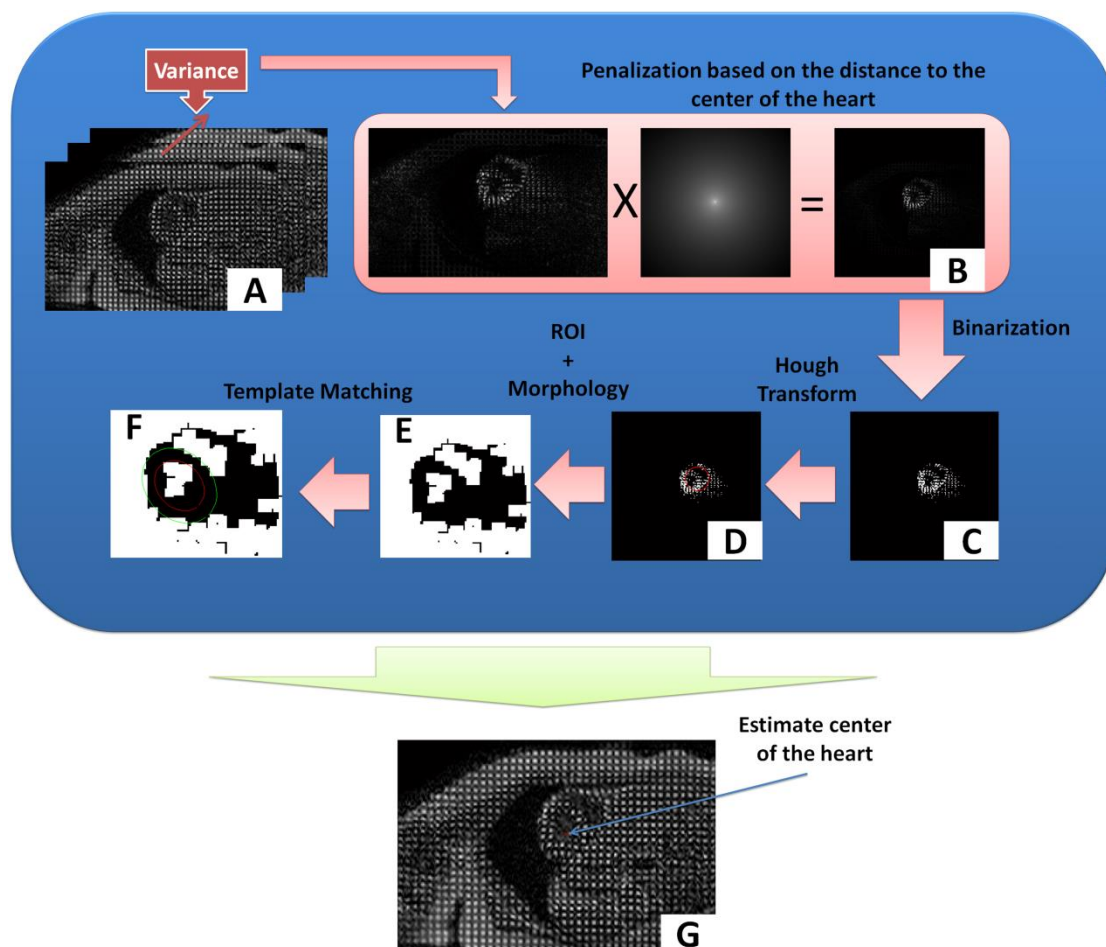


Figure 4.3 - Methodology used to determine the center of the myocardium.

The obtained variance image is further post-processed by noting that the myocardium is more likely to be centered in the image. As such, points were weighted according to their distance to the center (Figure 4.3B). In certain situations, this penalization can be essential to remove artifacts that appear on the image.

These steps will also enhance the myocardium relative to the background. Using a simple binarization operation based on the 1% of the pixels with highest intensity will therefore detect the majority of the myocardium, in addition to some false positive points e.g. originating from the right ventricle (see Figure 4.3C).

Estimate the LV position

After the binarization, three techniques are combined to estimate the center of the LV. First, the Hough transform is used to detect the LV position since it will favor regions having a dense number of points with a circular shape (more details in the next sub-section – “Hough Transform”, see Figure 4.3D). Using this result, an initial ROI around the center of LV is defined. Please note that this method can fail in some situations, e.g.: (i) the presence of the RV and (ii) the difficulties to detect the complete septal wall in the binary image (Figure 4.4). It is important to mention that we have difficulties to detect the septal wall based on the variance measure, because it has little motion compared to the other regions of the myocardium.

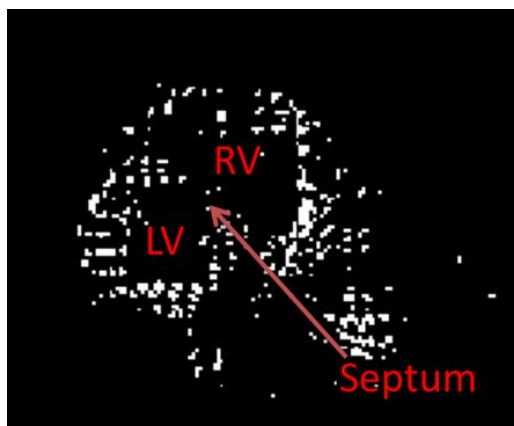


Figure 4.4 - Definition of the LV, RV and septum after the binarization step.

In order to solve these limitation, a morphological operator (closing followed by an opening) was applied over the binary image, to define the myocardial wall (Figure 4.3E). To define the final ROI (measuring a 50x50 pixels) a template matching scheme (see section 3.3) is applied (Figure 4.3F). The template matching will detect the final LV position (see Figure 4.3G).

As a last comment, it is important to mention that the present methodology estimate the LV position with an acceptable performance. A high accuracy to detect the LV center position is not expected, but in this step we only intend to detect a point inside the LV. As such, some errors to estimate the LV center position are acceptable.

Hough Transform

The Hough transform is an image processing technique used to detect specific object shapes on the image.

This approach was previously used for LV detection in cine-MRI [113, 115], and in the current thesis we intend to expand this technique to estimate the initial LV position in t-MRI images.

This method is applied on a binary image (Figure 4.5a). In each white point a virtual circle is drawn (Figure 4.5b) with different radius (the minimum value is 10 pixels and the maximum 30 pixels). A large range of radius should be used, due the variability of the properties of the heart. The location of the center of the heart will be the point where the intersection between all the virtual circles has the maximum value (Figure 4.5c).

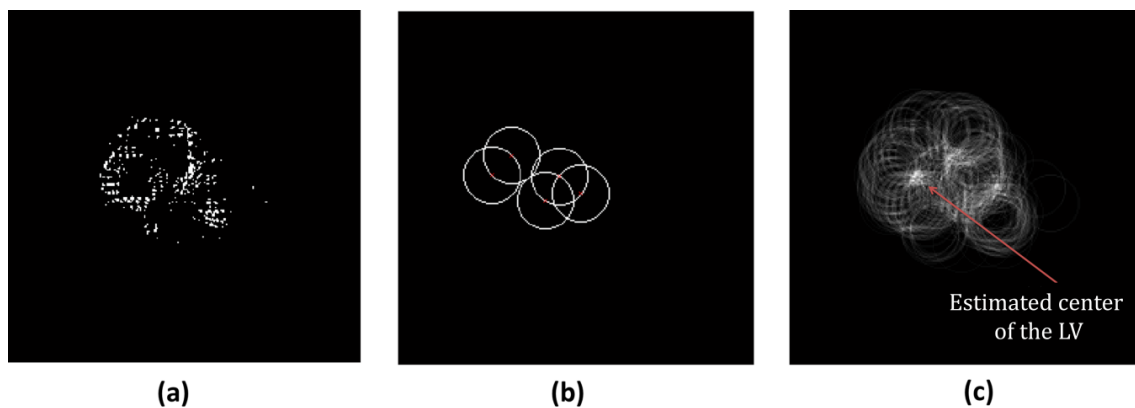


Figure 4.5 - (a) Binary image, (b) Virtual circle in some white points of (a), (c) result of the Hough transform method.

4.2.3. Image detagging

In this section, the method to remove/attenuate the presence of tags is described. This method is similar to the techniques previously presented in the section 2.2.1, where we intend to remove the frequency of the tags from the Fourier domain (Figure 4.6). Given our intention to use the BEAS segmentation framework (see section 3.2.2) to segment the myocardium, this step will be critical to ensure a proper evolution of the

contour. Without a detagging step, the original tagged MRI would contain too many interfaces near the myocardial borders due to the presence of tags.

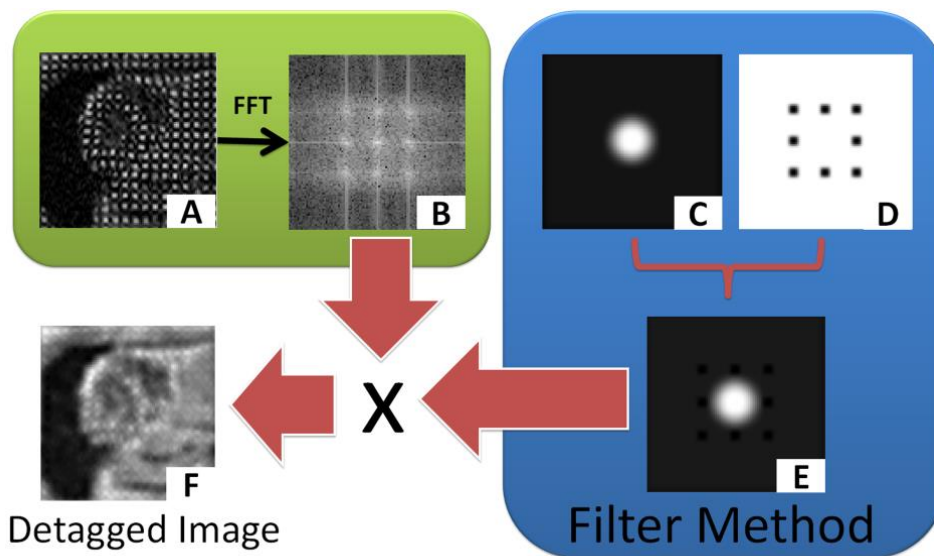


Figure 4.6 - Method used to suppress the tags in the t-MRI images.

Calculating the image spectrum

The spectrum (Figure 4.6B) is computed using a 2D FFT [34]. In t-MRI, since the tags present a certain orientation, this will translate in a specific representation on the Fourier Domain. In the spectrum (Figure 4.6B), a central peak defining the DC component, and 8 secondary peaks representing the first harmonic of the tag frequencies are shown. The orientation of the peaks is related to the orientation of the tags. In the images with tags acquired at 45° the spectrum will be rotated 45° when compared with the images acquired with tags at 0° (Figure 4.7).

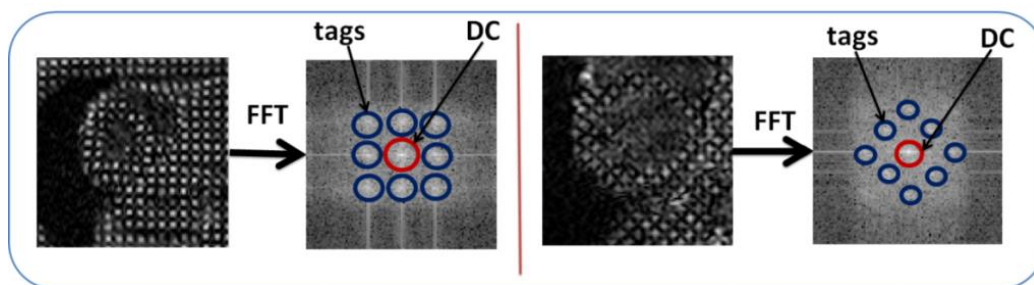


Figure 4.7 - Differences in spectrum between two t-MRI images with different tag orientations.

As shown in Figure 4.6E, a combination of two filters is used to pre-process the t-MRI. The first is a low pass filter (Figure 4.6C), to suppress noise and the second is a more specific filter (Figure 4.6D), which will attenuate only the frequencies corresponding to the tags.

Low pass filter

To design the low pass filter, we start from the tag positions in the spectrum. These positions will define the cutoff frequency. We intend to preserve the DC components, and attenuate the high frequency to suppress noise. In the spectral image, the DC component has the highest intensity followed by the tag frequencies. To detect the cutoff frequency, we first transform the spectrum to the polar domain by using the center position of the spectral image. Next, we create a binary image using only the 3% of pixels with highest intensity. In order to retain the tag frequency components only, we remove the first 10 lines of the polar image corresponding to the DC component (see Appendix I, Figure 10.2). Finally, a mathematical morphology (closing) operation is applied to generate an image where the white groups represent the tag positions (Figure 4.8).

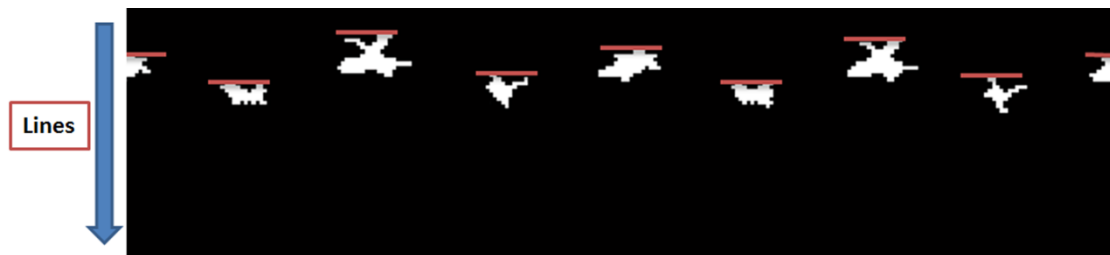


Figure 4.8 - Binary polar image used to define the cutoff frequency.

To obtain the cutoff frequency for the low pass filter, we detect the minimum line in each tag group (red lines in the Figure 4.8). Since we are using the polar space, each red line represents the radius in the cartesian space. The red line with minimum value will be used as cutoff frequency.

Figure 4.9 shows the resulting filter in the Cartesian space and its profile.

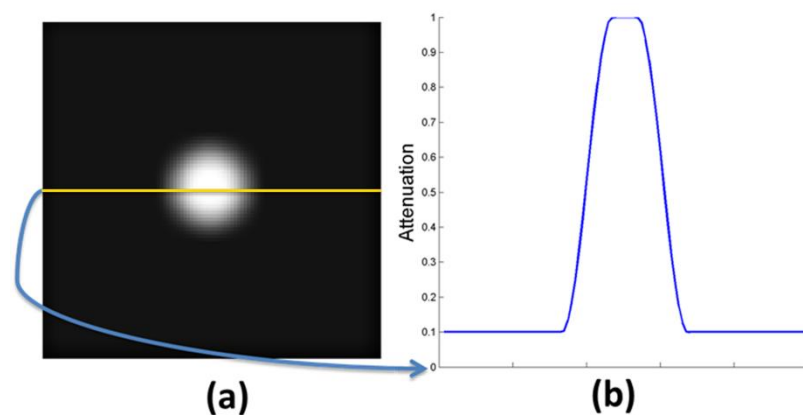


Figure 4.9 - (a) - Low pass filter, (b) - Profile of low pass filter on the yellow line.

Filter to attenuate the tag frequencies

A second filter will be used to attenuate only the frequencies corresponding to the tags. As such, it will have a more specific region of action.

First, we remove the DC component using the cutoff frequency obtained from the low pass filter. Without the DC component, the tag peaks are the structures with higher intensity in the spectrum image.

To detect the tag frequencies (first harmonic, see blue circle in Figure 4.7) an iterative approach is used. Initially, the method will search for the eight pixels with highest intensity in the spectrum image (Figure 4.7). In the next step, we will compare the distance between these 8 candidates. If the distance is lower than 10 pixels, the candidate with the lowest intensity is considered invalid (Figure 4.10a). The method continues until the 8 candidates representing the tag frequencies in all directions are detected (Figure 4.10b).

In the following steps we aim to fit a square to the 8 candidates. This fit increases the robustness of the methodology, removing errors that may occur during the detection of the candidates. To calculate the size of the square, we compute the difference between all 8 candidates and the center position (Figure 4.10b). Then, we calculate the mean value between them. This value will be used to define the size of the square (Figure 4.10c).

Finally, a morphological dilation of 3 pixels is applied on the 8 candidate points. At the same time, the intensities of the image are inverted. These regions are then convolved with a Gaussian filter to prevent the ringing effect. The resulting 8 regions are used in the filter to attenuate the tag frequencies (Figure 4.10d and Figure 4.10e).

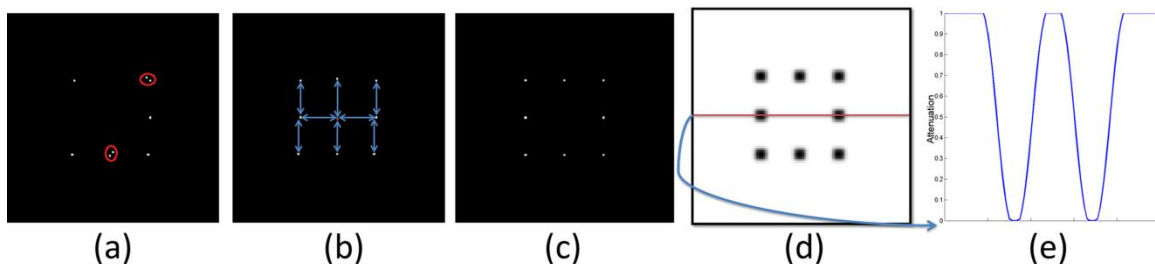


Figure 4.10 - Peak filter design. (a) Detection of 8 candidates with restrictions in terms of distance, (b) the 8 candidates pixels (white points), the blue lines represent the method used to compute the difference to the center of the image (red point), (c) The perfect square used in the method, (d) Filter design, application of a morphological dilate in (c) and convolution with a Gaussian filter, (e) Profile of the filter using as a reference the red line present in the figure (d).

Combination of the two filters

The combination of the two filters previously described, should efficiently suppress the tag components. A 3D visualization of the final filter profile is shown in Figure 4.11. The DC component is not attenuated and the biggest attenuation occurs on the tags frequency. It is important to mention that this combined filter is applied on the spectral image (Figure 4.6B), removing the tag components. Then, a 2D FFT^{-1} method will transform the resulting spectrum to the spatial domain (Figure 4.6F).

Please note that only the frequency corresponding to the first harmonic was removed. Some tests were done to remove first and second harmonics, but no difference was found when compared with the actual methodology (see Appendix I, Figure 10.3).

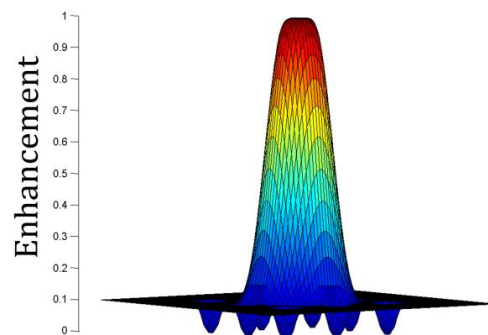


Figure 4.11 - 3D profile of the filter design to suppress the tags.

4.2.4. Automatic Initialization

The BEAS segmentation framework (as described in section 3.2.2) requires an initialization step, based on the LV center position, radius and estimate of the initial contour (Figure 4.12). An automatic initialization strategy could be based on the tagged image or the detagged image (obtained in section 4.2.3). However, we do not use the latter image due to the low contrast between the blood pool and the myocardium.

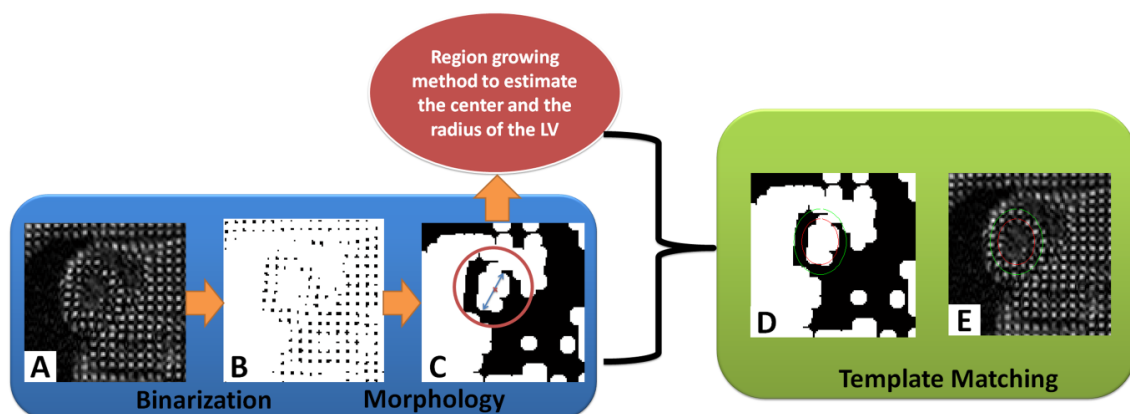


Figure 4.12 - Methodology used to automatically initialize the BEAS framework.

Definition of the myocardial wall

The first step presented in the Figure 4.12 is the binarization method. As proposed in [33] a multilevel Otsu methodology [116] with 3 classes is currently used. The first class represents the background and the tags, the second class represents the transition between the background and the brighter points and the third class represents the myocardial structures with higher intensity. The first two classes are joined and considered as background. The third class is used to define the myocardial wall. After the binarization, an image with the region between tags is observed (Figure 4.12B). In the next step, mathematical morphology (opening) is applied to join the points. This technique will remove isolated points and join sets, creating a binary image that will be used to detect the majority of myocardial wall (Figure 4.12C).

Template Matching

As previously explained in section 3.3, during the computation of the template matching we need a prior information about the radius and the center position of the heart. For the definition of the first template, we are using a region growing algorithm based on the BEAS framework (section 3.4, see Figure 4.12D). The BEAS Threshold is initialized using the estimated LV center position obtained from section 4.2.2 (Figure 4.13a). Please note that in the initial formulation of this method, the author [102] uses an expectation maximization algorithm to define a threshold. In the current approach, we are not using this method since we are working with a binary image (Figure 4.13).

The BEAS Threshold method can correct the center of the heart and estimate the radius of the LV cavity (Figure 4.13). This method can fail in the cases where only a small part of the myocardium wall was detected or when the method suggested in the section 4.2.2 is unsuccessful.



Figure 4.13 - Region growing based on BEAS framework. (a) Initialization of the algorithm, (b) Contour evolution, (c) Contour evolution with a result similar to the optimal solution, where is possible to see a difference between the initial center position (red point) and the new center position (green point), (d) optimal solution.

When the region growing techniques fails or the estimation of the radius has an impossible value, we develop a second methodology that will estimate the radius of the LV. This new method is only used when the BEAS threshold technique fails, since more accuracy is expected in the first formulation.

Using the LV center position estimated in section 4.2.2 and the binary image showed in Figure 4.12B, it is possible to compute an image, in the polar space, as demonstrated in Figure 4.14a. As referred previously, in the polar space each line represent the radius on the Cartesian space. In that case, we will compute for each line, the number of points that belong to the myocardium – black points on the image (Figure 4.14b). In the end, we use the maximum value as a reference for the minimum radius. Obviously, this method has many disadvantages: first, we need a good estimation of the center of the heart; second, we assume a circular shape of the LV.

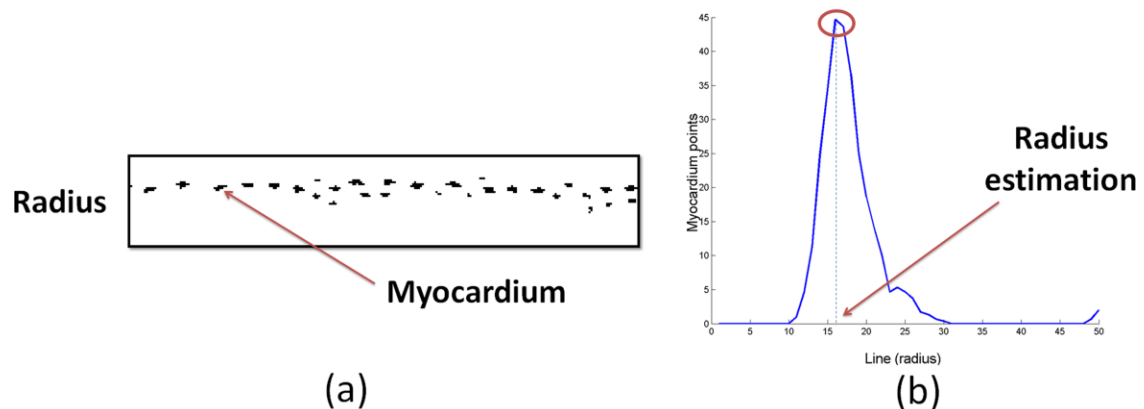


Figure 4.14 - Estimation of the minimum radius. (a) Image in polar space, and (b) number of points from the myocardium in each line of the polar image.

Based on the minimum radius and the center position, the template matching approach is applied. As result, a first estimation of the endo- and epicardial contours is created. This estimate will be used as initialization for the BEAS framework.

Segmentation parameters

In t-MRI is difficult to have access to a viable ground truth. As such we used the parameters proposed by Queirós *et al.* [33] in the development of a fully automatic approach for LV segmentation in cine-MRI. In that case, h (scale, see section 3.2.2) was set to 2^2 and 2^3 for the wall position and thickness respectively and 64 points were used on each boundary for the contour discrete representation. A local region of size 11×11 was used to compute the local region means.

4.2.5. Segmentation propagation

A t-MRI acquisition typically consists of 3 slices (apical, mid and basal slice). These slices are acquired independently, and may therefore potentially introduce misalignments between them.

In this section, we describe a technique to propagate information inter-slices. We are propagating the LV center position between consecutive slices, to prevent failures during the section 4.2.2, principally on the apical slice.

As such, the result of the segmentation on basal slice will be used to define the center position on the next slices, as demonstrated on the Figure 4.15. Please note that since we are using the BEAS threshold algorithm, we can correct offsets that occur due the misalignments.

As a last comment, it is important to mention that all the methodology presented in Figure 4.2 is only applied on the basal slice. In this slice the myocardium is easily detected, the image noise is low and a low number of tags are seen on the blood pool. Finally, in the mid and apical slices are only applied the methods explained in sections 4.2.3 and 4.2.4.

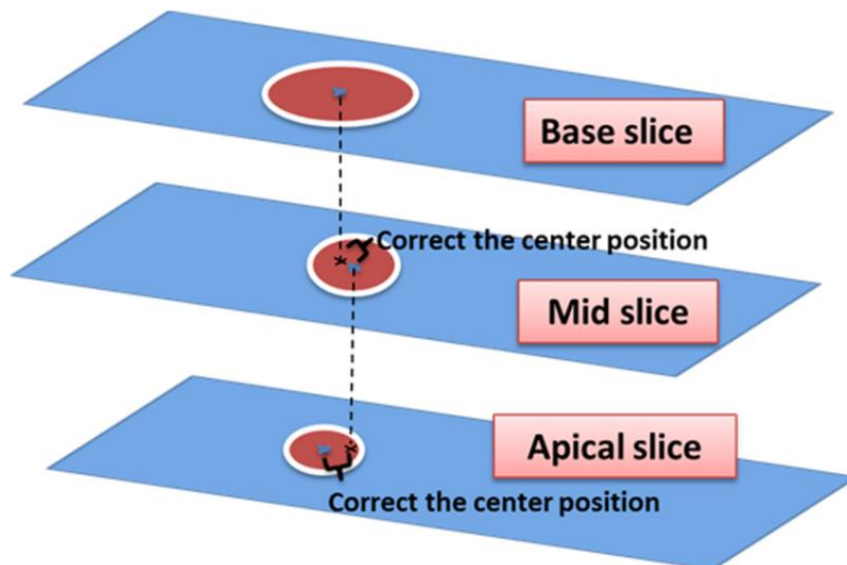


Figure 4.15 – 3D methodology used to propagate the LV center position.

4.3. Cardiac Motion estimation

4.3.1. Sequential 2D+t FFD formulation

In this section, the traditional sequential 2D formulation introduced in section 3.1.7, is further extended to include the temporal information. The proposed sequential 2D+t approach poses the problem of tracking myocardial motion as a 3D registration problem (Figure 4.16). This formulation was published by Morais *et al.* [117].

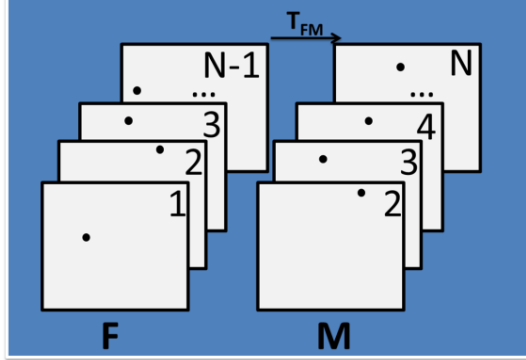


Figure 4.16 - Schematic used for the proposed sequential 2D+t FFD.

The images to be registered are two 3D sets represented by:

$$F = \{I_i, i \in [1, N - 1]\} \quad (4.1)$$

and a temporal shifted version of F :

$$M = \{I_j, j \in [2, N]\} \quad (4.2)$$

where N represents the number of frames in the cardiac sequence.

To create this strategy, a straightforward extension of the FFD model to include the temporal dimension would lead to following the description of the transformation model:

$$T(\mathbf{r}, t) = (\mathbf{r}, t) + \mathbf{u}_{F \rightarrow M}(\mathbf{r}, t) \quad (4.3)$$

and the following deformation field:

$$\mathbf{u}_{F \rightarrow M}(\mathbf{r}, t) = \sum_{i \in \mathfrak{N}_x} \sum_{j \in \mathfrak{N}_y} \sum_{k \in \mathfrak{N}_t} \boldsymbol{\mu}^{ijk} \beta_x^3 \left(\frac{x - \kappa_x^i}{\sigma_x} \right) \beta_y^3 \left(\frac{y - \kappa_y^j}{\sigma_y} \right) \beta_t^3 \left(\frac{t - \kappa_t^k}{\sigma_t} \right) \quad (4.4)$$

with κ_γ and σ_γ the control point location and spacing respectively, and \mathfrak{N}_γ the set of control points within the compact support of the B-spline β_γ ($\gamma \in [x, y, t]$). In the proposed approach the temporal information is represented by a temporal B-spline with compact support σ_t .

However, a trivial but undesirable solution to this registration formulation would be the transformation field which just shifts the sequence in time, i.e. $\mathbf{T}(\mathbf{r},t)=(\mathbf{0},t-1)$. This result is obvious, since we are dealing with a 3D registration problem between two shifted blocks.

In the next part of the work we will explain the method used to constrain the optimization. To prevent optimization in the temporal direction, several considerations should be made.

First of all, the transformation should be constrained to only recover inter-frame registrations which are optimized in a joint way. This can be achieved by noting $\mathbf{u}_{F \rightarrow M} = [u_x, u_y, u_t]$ in equation (4.4) and setting:

$$u_t = 0 \quad (4.5)$$

Equation (4.5) guarantees that the deformation in the temporal direction will always be zero, such that the transformation will never move any point in this direction. In practice, this restriction can easily be implemented by setting $\mu_t^{k+1} = \mu_t^0 = 0$ in the optimization step (equation 3.12), while keeping the update functions unchanged in the spatial direction. As such, we only use the in-plane image gradients to update the transformation parameters.

Secondly, since we want to align the whole image sequence, the original formulation of the cost function in (3.15) should be modified to:

$$E = \frac{1}{d} \sum_{(\mathbf{r},t) \in F} [\mathbf{F}(\mathbf{r},t) - \mathbf{M}(\mathbf{T}(\mathbf{r},t))]^2 + \frac{\omega_{BE}}{d} \sum_{(\mathbf{r},t) \in F} \left\| \frac{\partial^2 \mathbf{T}(\mathbf{r},t)}{\partial(\mathbf{r},t)^2} \right\|^2 \quad (4.6)$$

where the classic expression of the bending energy [69] is extended in time as:

$$\begin{aligned} \left\| \frac{\partial^2 \mathbf{T}(\mathbf{r},t)}{\partial(\mathbf{r},t)^2} \right\|^2 &= \sum_{\gamma \in (x,y,t)} \left(\frac{\partial^2 T_\gamma}{\partial x^2}(\mathbf{r},t) \right)^2 + \left(\frac{\partial^2 T_\gamma}{\partial y^2}(\mathbf{r},t) \right)^2 + \left(\frac{\partial^2 T_\gamma}{\partial t^2}(\mathbf{r},t) \right)^2 \\ &+ 2 \left(\frac{\partial^2 T_\gamma}{\partial xy}(\mathbf{r},t) \right)^2 + 2 \left(\frac{\partial^2 T_\gamma}{\partial xt}(\mathbf{r},t) \right)^2 + 2 \left(\frac{\partial^2 T_\gamma}{\partial yt}(\mathbf{r},t) \right)^2 \end{aligned} \quad (4.7)$$

with $\mathbf{T} = [T_x, T_y, T_t]$ and (\mathbf{r},t) representing each point in the constructed image sequence \mathbf{F} . Please note that due to the imposed restriction in the optimizer, the following terms are always zero, since the gradient in this direction is never updated:

$$\frac{\partial^2 \mathbf{T}_t}{\partial \gamma \partial \gamma}(\mathbf{r},t) = 0 \quad (4.8)$$

However, without further modifications, equation (4.7) would lead to an over-smoothing effect in the time due to the contributions of the second order derivative

terms in time. To solve this limitation during the computation of the BE, the following constrain was added:

$$\frac{\partial^2 T_\xi}{\partial t \partial \gamma}(\mathbf{r}, t) = 0 \quad (4.9)$$

where $\gamma \in [x, y, t]$ and $\xi \in [x, y]$.

Finally, the expression of the bending energy becomes:

$$\left\| \frac{\partial^2 \mathbf{T}(\mathbf{r}, t)}{\partial (\mathbf{r}, t)^2} \right\| = \sum_{\xi \in (x, y)} \left(\frac{\partial^2 T_\xi}{\partial x^2}(\mathbf{r}, t) \right)^2 + \left(\frac{\partial^2 T_\xi}{\partial y^2}(\mathbf{r}, t) \right)^2 + 2 \left(\frac{\partial^2 T_\xi}{\partial xy}(\mathbf{r}, t) \right)^2 \quad (4.10)$$

This implies that the BE expression (4.10) is comparable to the 2D formulation (3.10) and the temporal smoothness is achieved only due to the compact support of the temporal B-spline.

As a last comment, please note that an anisotropic grid spacing was used, keeping the temporal support fixed over all the 3 scales, while halving the spacing in the spatial direction in every scale.

4.3.2. Fixed 2D+t FFD formulation

As described in section 2.1, Chandrashekara *et al.* [68] proposed a strategy similar to the sequential 2D+t formulation. In this work, the reference block F is fixed, using the ED frame (Figure 4.17). Within the context of the current thesis, their strategy is therefore termed fixed 2D+t FFD formulation.

In order to compare the influence of the registration scheme, we also implemented their method. We prevent the optimization in the temporal direction, using the constraints suggested for the sequential 2D+t. It is important to mention that these constraints are not indicated on the original work [68], but a similar strategy to prevent optimization in the temporal direction is expected.

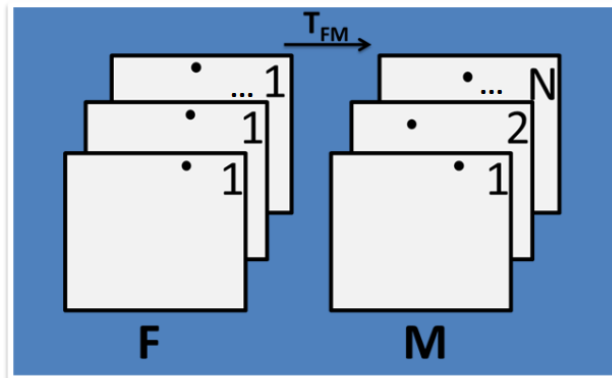


Figure 4.17 - Schematic used for the fixed 2D+t FFD.

4.4. Strain estimation

4.4.1. Strain estimation in the sequential 2D+t and fixed 2D+t FFD formulation

In section 3.6, we described a method to estimate strain using a series of pairwise registrations. By cumulating the transformation, it was shown it is possible to describe the motion of each point in the frame f relatively to the ED frame.

In the proposed sequential 2D+t formulation, only one transformation is used to describe the motion of each point (\mathbf{r}, t) of block F to a new position in block M . As such, we can't cumulate the transformation as described before.

In the sequential 2D+t methodology, the displacements can therefore be cumulated (Figure 4.18) by taking the corresponding time frames:

$$\mathbf{T}_{ED \rightarrow t}(\mathbf{r}, t) = \mathbf{T}_{F \rightarrow M}(\mathbf{r}, t - 1) \circ \dots \circ \mathbf{T}_{F \rightarrow M}(\mathbf{r}, 2) \circ \mathbf{T}_{F \rightarrow M}(\mathbf{r}, ED) \quad (4.11)$$

For the fixed 2D+t FFD formulation, transformations do not have to be cumulated, since all the transformations are defined relative to the ED frame.

As a last comment, using the obtained transformation fields, strain can then be computed by using the expression (3.29) or (3.30).

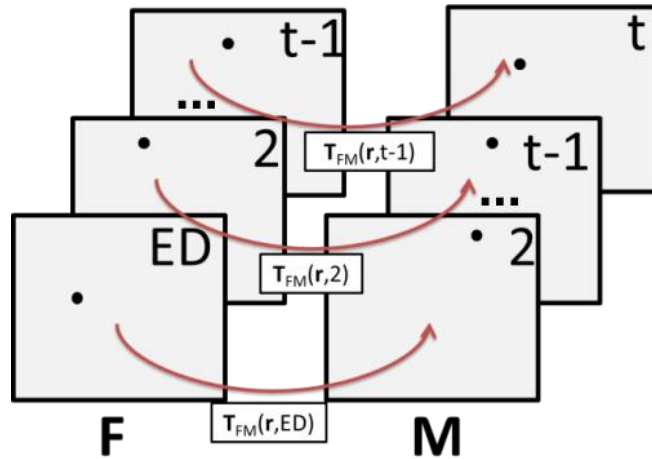


Figure 4.18 – Cumulating the displacement field in the proposed sequential 2D+t.

4.4.2. Contours definition on the ED frame

Since we are using the 4th frame to start the automatic segmentation methodology, we need to modify the strategy proposed for the computation of the strain values. The method presented in section 3.6 and expanded in 4.4.1, calculates the strain

values using the ED frame as reference. To solve this problem, we implement a second registration problem as shown in the Figure 4.19. One of the registration problems will be used to detect the optimal transformation between 4th frame and the ED frame (Figure 4.19). The optimal transformation will define the contours in the ED. The other registration problem will be used to compute the strain value, using the method explained in the section 3.6 and 4.4.1. Please note that in this step we use whole the cardiac sequence.

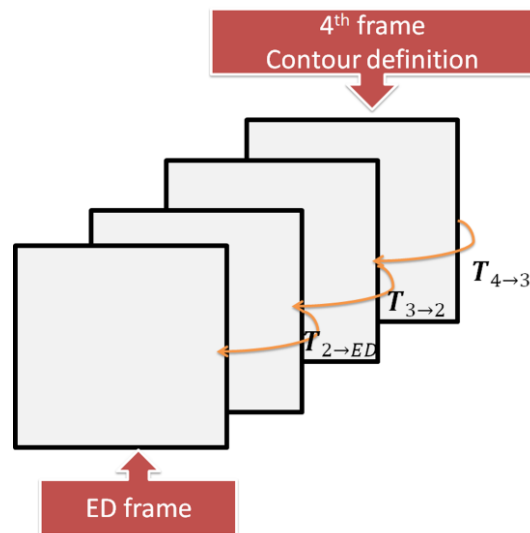


Figure 4.19 - Strategy used to pass the contours from the frame number 4 for the ED frame.

Methods

5. Methods

In this chapter, all the experiments performed during the current master thesis are described.

5.1. Datasets

In this master thesis, three different datasets are used: a synthetic dataset with ground truth, a porcine dataset and a human clinical dataset.

The synthetic dataset¹ (Figure 5.1) has four image sequences with different signal noise ratio (SNR). In each sequence, a total of 30 frames were acquired. Several tag positions were tracking during the cardiac cycle, creating the ground-truth. Please note, that these datasets are not capable to simulate the tag fading.

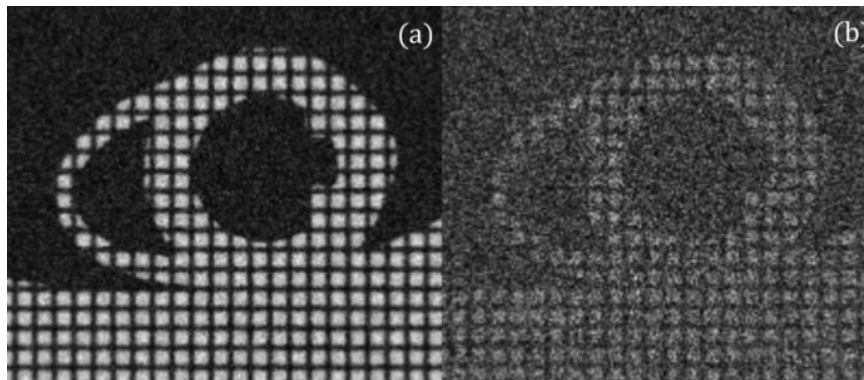


Figure 5.1 - Synthetic images with (a) SNR = 18db and (b) SNR = 6dB [49].

In the porcine dataset (Figure 5.2), unhealthy and healthy exams are available. An experimental database of a pre-clinical porcine model of chronic myocardial ischemia, with an induced left-anterior descending coronary artery lesion, resulting in a small but variable anterior, anterospetal infarct is used in the lesion cases. Datasets were acquired on a 3T MRI unit (TRI-tim, Siemens, Erlangen, Germany). From these datasets a short-axis image with grid tagging was tracked and compared to the corresponding short – axis of the delayed-enhancement dataset. Tagging datasets were acquired with a 6 mm space grid, using gradient echo readout, with ECG triggering and during suspended respiration. In plane resolution was 1.3x1.3 mm and slice thickness was 6 mm. Echo time was 3.96ms, repetition time 41 ms and flip angle 10°. Delayed-enhancement datasets (Figure 5.2) were acquired 15 min after 0.2 mmol/kg Gadolinium injection, with a voxelsize of 1.8x1.8x6mm. Inversion time was adapted to obtain

¹ The author would like to thank Smal *et al.* for providing access to the synthetic dataset.

optimal nulling of the healthy myocardium (340-370ms), repetition time was 2.19 ms, echo time 0.78 ms and flip angle 15° .

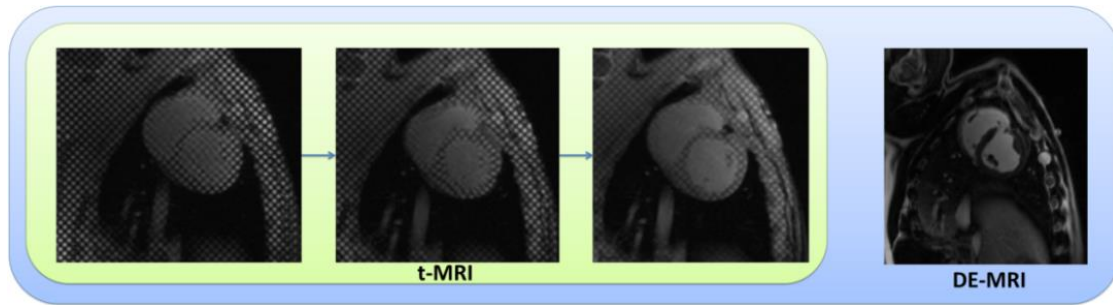


Figure 5.2 - Registration validation using t-MRI and DE-MRI images.

The human dataset is obtained from a multi-center study with core-lab analysis. The data used in the current master thesis, corresponds to patients with suspicion of ongoing (chronic) myocardial ischemic heart disease and has been acquired in two different laboratories in Europe (Figure 5.3), while being analyzed in a core lab whose expertise focuses on t-MRI images. All the acquisitions present the short-axis images at base, mid and apical slice. In center 1 (Figure 5.3), the images were acquired with tag orientation at 0° , resolution 1.367×1.367 mm and a slice thickness of 14 mm. The center 2 (Figure 5.3) presents images with tag orientation at 45° degrees, resolution 1.25×1.25 mm and a slice thickness of 6 mm.

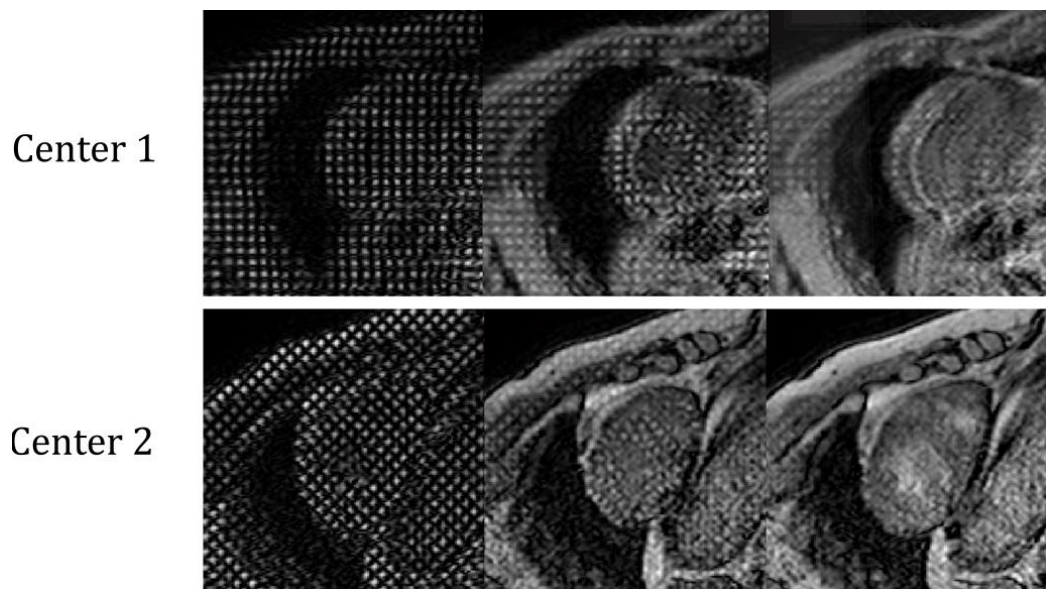


Figure 5.3 - t-MRI acquired in two different centers.

5.2. Experiments

5.2.1. Parameter tuning

The validation in a registration problem is not a straightforward task, due to the difficulty in creating an acceptable ground-truth.

In the first experiment of the current master thesis, we intend to study the influence of different parameters on the performance of the algorithm, e.g. final grid spacing $[\sigma_x, \sigma_y]$, BE weight ω_{BE} , number of scales used in the multi-resolution registration problem and the used metrics in the cost function. Two images obtained from the synthetic dataset are used (the image with highest SNR, SNR = 18dB; and the image with lower SNR, SNR = 6dB). Using the available ground truth, a comparison between the sequential 2D FFD formulation and the proposed sequential 2D+t FFD formulation is performed. The root mean square error (RMSE) and end-of-systole error (EES) were used to compare the different methodologies.

5.2.2. Detection of (dys)functional regions

During this experiment, 8 MRI studies were randomly selected from the porcine dataset with chronic myocardial ischemia. Additionally, 4 MRI studies of normal animals were included. Radial and circumferential strain maps were computed and compared with DE-MRI regions to investigate whether dysfunctional areas could be identified. Next, the myocardium was divided using a standard six-segmental model as described in section 3.6 and each segment was classified as an infarct, adjacent or normal region as indicated by the corresponding delay-enhancement Magnetic Resonance Imaging (DE-MRI). A paired t-test between these regions was used, for the sequential 2D FFD formulation and the proposed sequential 2D+t FFD formulation, to assess whether or not dysfunctional regions could be localized.

5.2.3. Validation of the (semi-) automatic segmentation approach

In this experiment, 40 exams from the center 1 and 43 exams from the center 2 are used to validate the segmentation technique.

First, two non-experts create a manual contour of these datasets. The non-experts mentioned that they were not capable to segment the first frame. As such, they segment the frame number 4. To facilitate the manual segmentation, the non-experts can use temporal information.

Second, using the (semi-) automatic approach we define the automatic contour. Please note, in some cases a user input is needed to correct the contours. A friendly user interface was therefore developed (Figure 5.4) to visualize the automatic contours and correct them. Two types of corrections are possible: correction of the LV center position and correction of the contour based in one click on the image.

Then, we study the intra-observer variability, the inter-observer variability (comparing with the automatic contour) and the differences between a mean contour, using the non-experts delineation, and the automatic result. The comparison was done using the APD distance, dice value, the Hausdorff distance (see section 3.5), the correlation coefficient and the BIAS value (a paired t-test is used to verify if the differences are statistically significant), using the area of the endocardium and epicardium. At the same time, a statistical study using boxplots is suggested, to verify the variability of the results and the number of outliers.

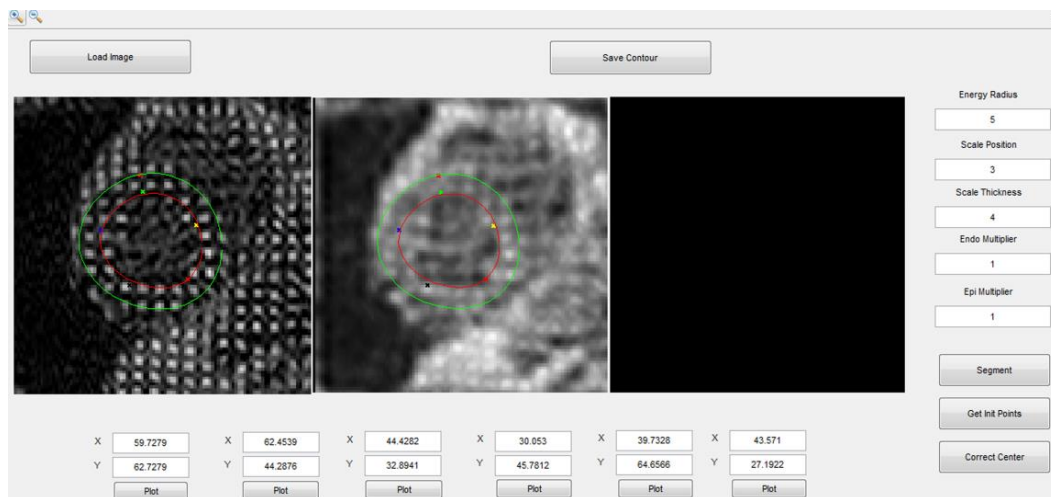


Figure 5.4 - Interface developed for assess the automatic segmentation of the LV in t-MRI.

5.2.4. Validation of the proposed sequential 2D+t FFD formulation

During this experiment, we compared the different registration schemes presented in this master thesis (sequential 2D, sequential 2D+t and fixed 2D+t). The comparison is performed using the global strain curve in the radial and circumferential direction. This curve was obtained by averaging strain over the 6 segments in a mid-slice case. The contours are defined using the (semi-) automatic methodology. One case (selected randomly) from the human clinical dataset is used. At same time, we compare trajectories of individual points.

5.2.5. Comparison of the proposed algorithm with a commercial state-of-the-art solution

In this experiment, we compared the proposed methodology with the commercial solution (*diagnosoft-HARP*), using the human clinical dataset from a multi-center study (Doppler CIP). The *HARP* results are obtained from core-lab analysis. As such, we don't have any information about the initial contour. The core-lab analysis only has the circumferential strain value.

Cases where the result from the commercial software showed a positive circumferential strain value at ES defined by physician were excluded. This result is not physiologic. As such, for center 1, 40 exams were acquired, but only 30 mid, 30 basal slices and 23 apical slices were using in the comparison. In center 2, 43 exams were acquired, but only 16 apical, 34 mid slice and 35 basal slices were used.

A linear regression and a Bland-Altman analysis (a paired t-test is realized to verify if the BIAS is statistically significant) are performed between the presented methods and the commercial software. Two studies are suggested, the first uses the ES frame defined by the physician as reference, and the second study uses the strain peak value in each technique as reference. The methods used are: sequential 2D FFD, and the proposed sequential 2D+t FFD formulation, with $\sigma_t = 1$, $\sigma_t = 2$ and $\sigma_t = 3$. Please note, a global and a regional study is shown.

A comparison between the mean peak values using the global and segmental strain curve, in each technique, is realized. To verify if the differences are statistically significant, a paired t-test was used.

The last study consists in an ANOVA table. During this study only the segmental strain value are used. At same time, we perform an unpaired t-test to verify if the two methods used (proposed framework and commercial software) are capable to distinguish the strain value in each slice.

Results

6. Results

6.1. Parameter tuning

The RMSE and EES in the simulated data (image with signal noise ratio (SNR) equal to 18dB) are shown in Figure 6.1.

The RMSE and the EES in the simulated data (image with SNR = 18dB) are shown in Figure 6.2 using three different registration metrics for the computation of the cost function. During the formulation of the registration method we suggest a multi-resolution approach with 3 scales. In this image, the result using 4 scales is shown.

In the Figure 6.3 we can observe the results in terms of RMSE and EES for the image with SNR = 18dB. In this figure, 64 bins are used to compute the joint histogram.

In Figure 6.4, a similar comparison is done in terms of RMSE and EES using three different metrics, but using an image with low SNR (SNR = 6dB).

Figure 6.5 shows the RMSE and EES for the synthetic image with SNR = 6 dB [49] using different values for the final grid spacing and the weight ω_{BE} using a multi-resolution approach with 4 scales.

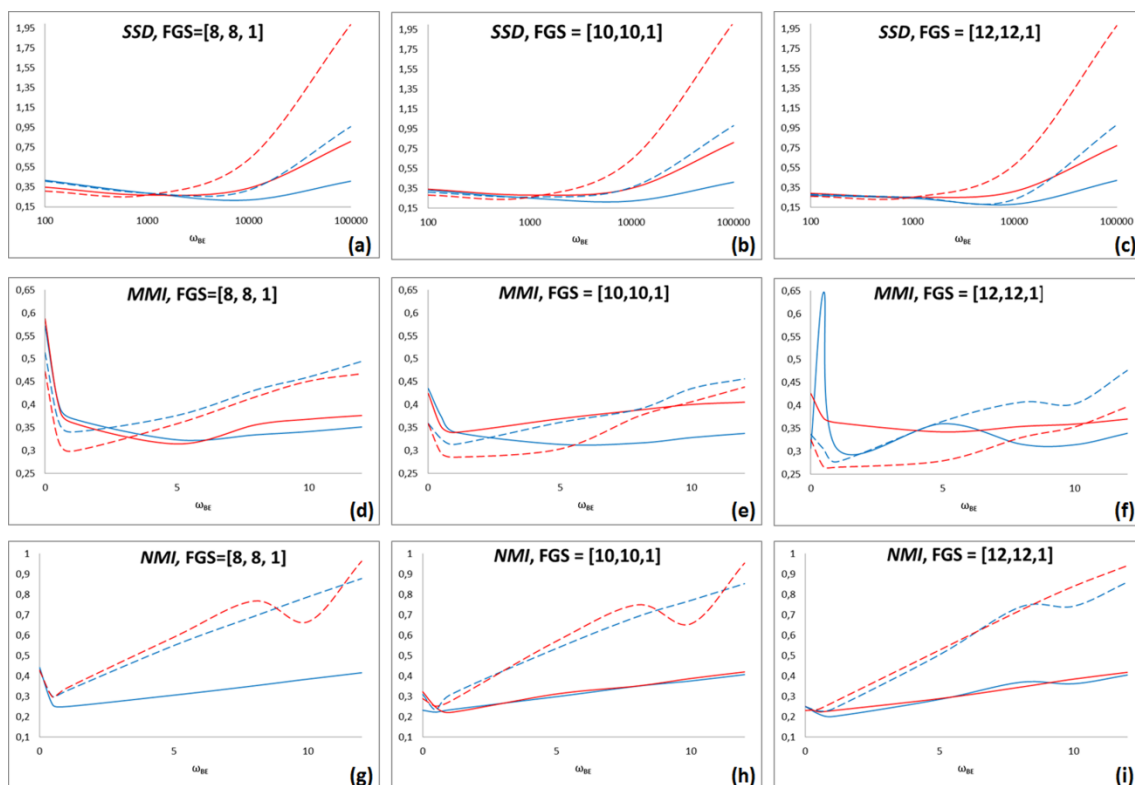


Figure 6.1 - Influence of the ω_{BE} weight in image with SNR = 18dB [49]. The vertical axis represents the error in pixels. The results with sequential 2D (red) and the proposed sequential 2D+t (blue) approaches are presented, in terms of RMSE (solid line) and EES (dashed line), using different metrics and different final grid spacing (FGS) values.

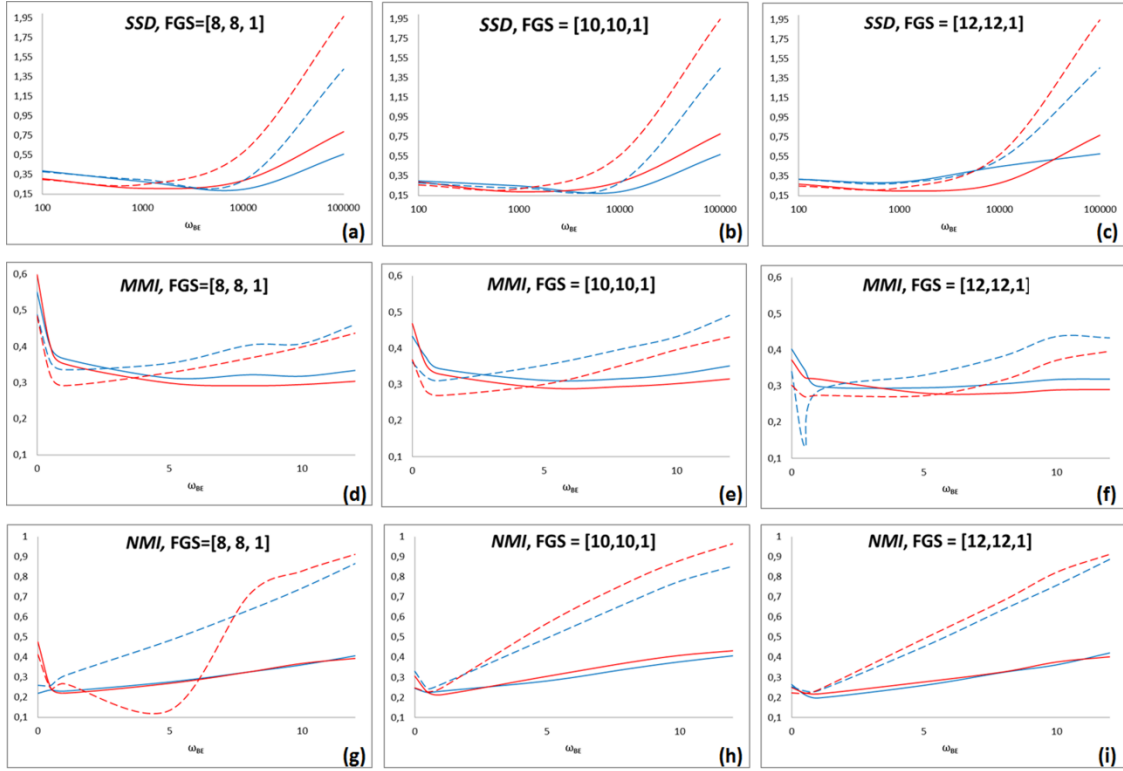


Figure 6.2 - Influence of the ω_{BE} weight in image with SNR =18dB [49] using 4 scales. The vertical axis represents the error in pixels. The results with sequential 2D (red) and the proposed sequential 2D+t (blue) approaches are presented, in terms of RMSE (solid line) and EES (dashed line), using different metrics and different final grid spacing (FGS) values.

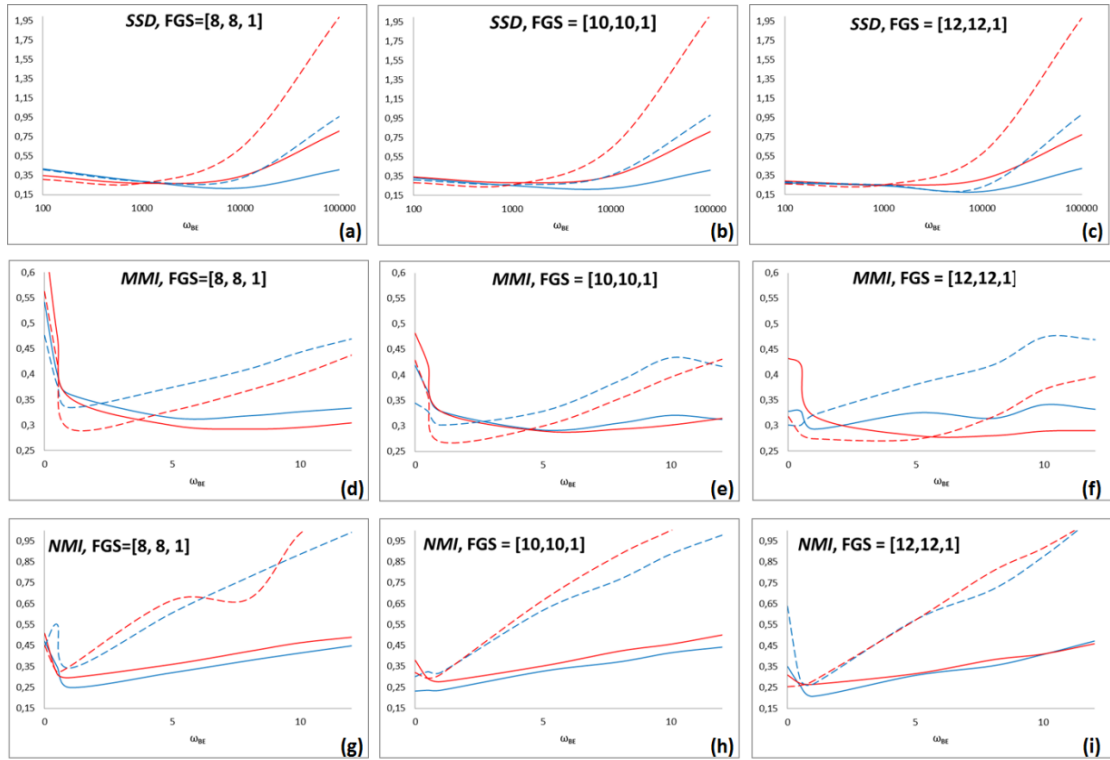


Figure 6.3 - Influence of the ω_{BE} weight in image with SNR =18dB [49] using 64 bins to compute the joint histogram. The vertical axis represents the error in pixels. The results with sequential 2D (red) and the proposed sequential 2D+t (blue) approaches are presented, in terms of RMSE (solid line) and EES (dashed line), using different metrics and different final grid spacing (FGS) values.

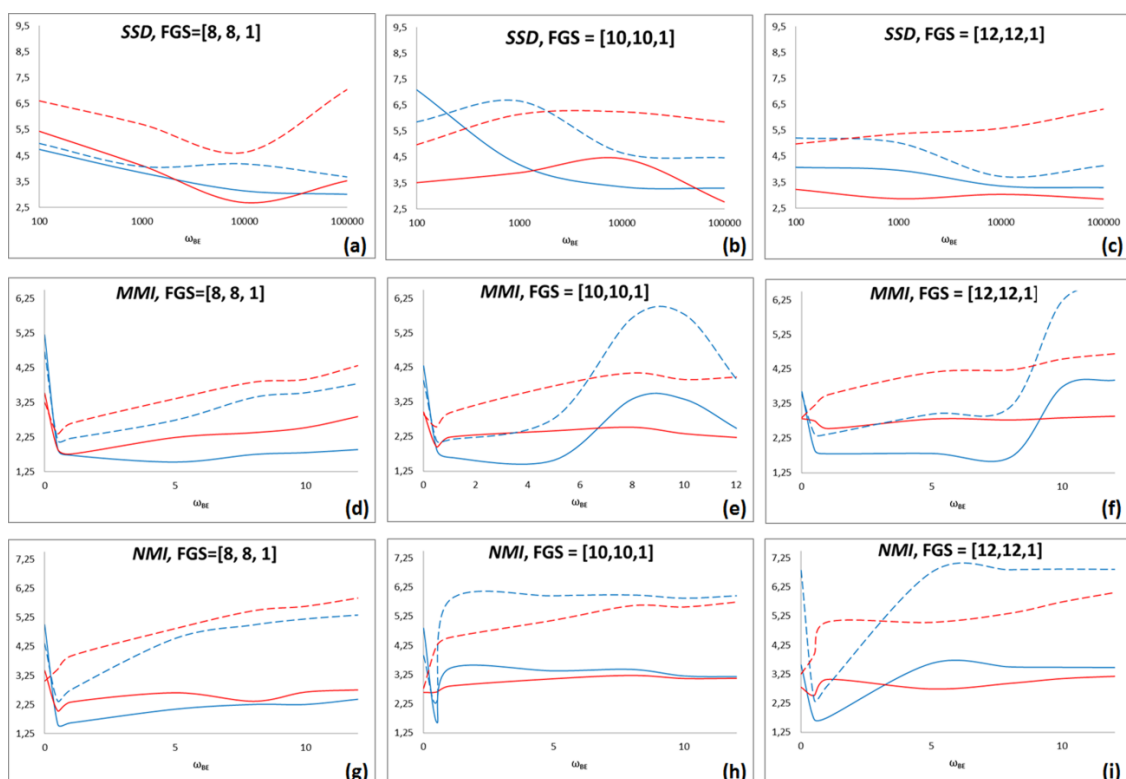


Figure 6.4 - Influence of the ω_{BE} weight in image with SNR =6dB [49]. The vertical axis represents the error in pixels. The results with sequential 2D (red) and the proposed sequential 2D+t (blue) approaches are presented, in terms of RMSE (solid line) and EES (dashed line), using different metrics and different final grid spacing (FGS) values

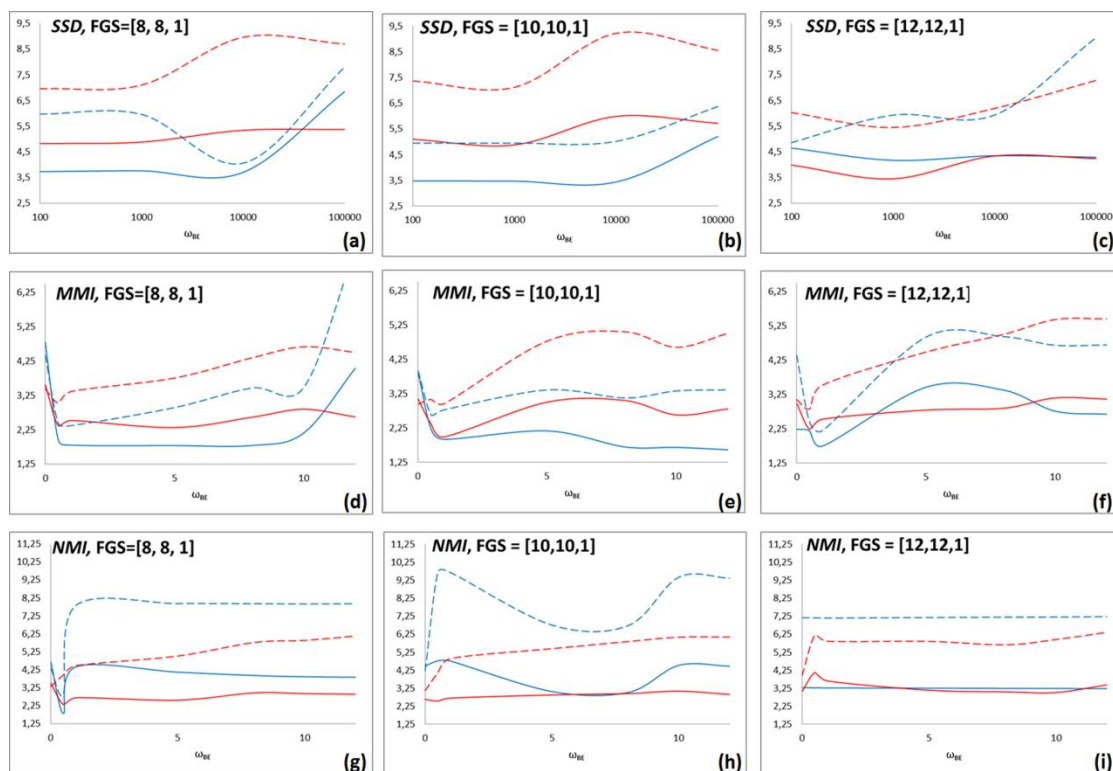


Figure 6.5 - Influence of the ω_{BE} weight in image with SNR =6dB [49] using 4 scales. The vertical axis represents the error in pixels. The results with sequential 2D (red) and the proposed sequential 2D+t (blue) approaches are presented, in terms of RMSE (solid line) and EES (dashed line), using different metrics and different final grid spacing (FGS) values

6.2. Detection of (dys)functional regions

Figure 6.6 presents an example strain map obtained from the in-vivo porcine datasets using the proposed 2D+t and the sequential 2D approaches. A comparison between the registration result for the detection of the dysfunctional regions (blue regions) and the DE-MRI is presented.

Figure 6.7 shows a normal porcine dataset, which can be proved by the DE-MRI image (Figure 6.7d). The results in terms of radial and circumferential strain for the sequential 2D and the proposed sequential 2D+t approaches are illustrated.

In Figure 6.8 the ability to detect infarct regions using either the sequential 2D+t or the sequential 2D approaches is shown.

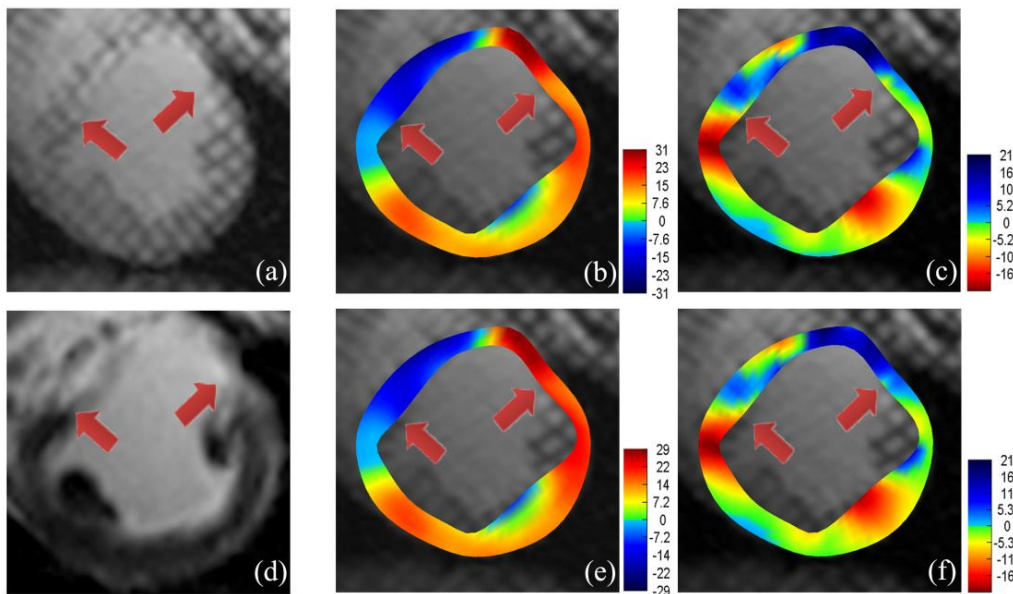


Figure 6.6 - (Dys)functional regions detection using different methodologies. (a) t-MRI at end-systole, (d) DE-MRI, (b/e) radian strain map and (c/f) circumferential strain map using the sequential 2D (top) and the proposed sequential 2D+t (bottom). The arrows represent the borders of the dysfunctional region.

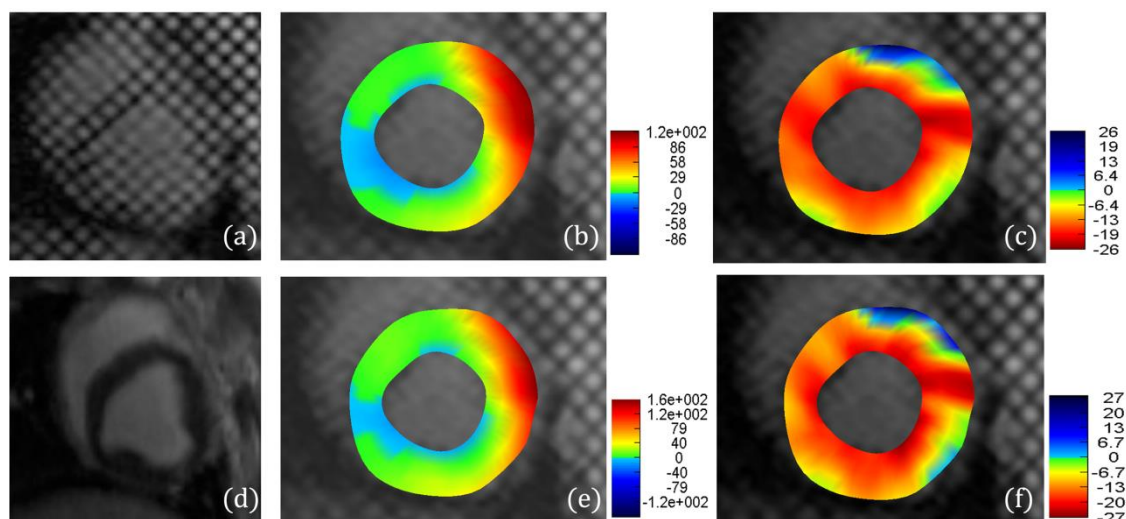


Figure 6.7 - (Dys)functional regions detection using different methodologies. In this situation a normal dataset is used. (a) t-MRI at end-systole, (d) DE-MRI, (b/e) radial strain map and (c/f) circumferential strain map using the sequential 2D (top) and the proposed sequential 2D+t (bottom).

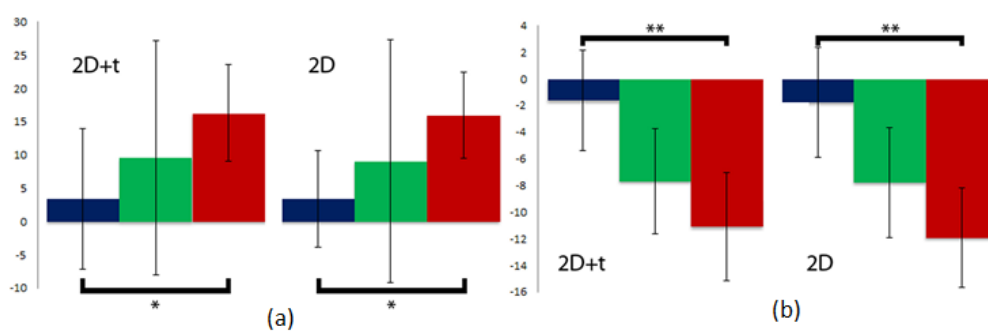


Figure 6.8 - Capability to distinguish between dysfunctional and normal regions by assessing (a) radial and (b) circumferential strain. The different bars indicate the respective functional regions: (blue) infarct, (green) adjacent and (red) normal. * $p < 0.05$, ** $p < 0.001$.

6.3. Validation of the (semi-) automatic segmentation approach

Table 6.1 and Table 6.2 show the intra-observer differences, inter-observer differences comparing with a (semi-)automatic approach and the differences between a mean contour and the (semi-)automatic approach, using all the datasets available in each center, for the endocardium and epicardium, respectively. At the same time, it is important to mention that the (semi-) automatic approach was capable to segment more slices than the non-experts.

In Figure 6.9, we present a study in terms of percentiles and outliers point for the segmentation validation. The following comparisons are shown: 1) between the non-experts (E1 and E2); E1 and E2 with the (semi-) automatic approach (Auto); and a mean contour (using the intermediary contour between E1 and E2) with Auto.

Table 6.1 - Dice value, average perpendicular distance (APD), Hausdorff value for the endocardium using different comparisons between the non-experts (E1 and E2), the (semi-) automatic approach (Auto) and the mean contour (MC) obtained from E1 and E2. At same time, we compute the area of the endocardium and determine correlation coefficient (r) and BIAS. *Statistically significant (p<0.05)

	Dice	APD (mm)	Hausdorff (mm)	Correlation coefficient (r)	BIAS
E1 and E2	0.881±0.084	2.202±1.402	5.106±2.645	0.904	157.357*
E1 and Auto	0.867±0.111	2.683±1.284	5.790±2.32	0.868	94.611*
E2 and Auto	0.837±0.104	3.203±1.829	6.570±2.979	0.854	251.968*
MC and Auto	0.864±0.082	2.690±1.414	5.634±2.422	0.882	181.681*

Table 6.2 - Dice value, average perpendicular distance (APD), Hausdorff value for the epicardium using different comparisons between the non-experts (E1 and E2), the (semi-) automatic approach (Auto) and the mean contour (MC) obtained from E1 and E2. At same time, we compute the area of the epicardium and determine correlation coefficient (r) and BIAS. *Statistically significant (p<0.05)

	Dice	APD (mm)	Hausdorff (mm)	Correlation coefficient (r)	BIAS
E1 and E2	0.943±0.039	1.743±1.046	4.282±1.922	0.943	-45.157*
E1 and Auto	0.916±0.043	2.512±1.152	5.789±2.322	0.901	-95.461*
E2 and Auto	0.909±0.045	2.763±1.310	6.215±2.441	0.886	-140.618*
MC and Auto	0.9177±0.040	2.475±1.123	5.535±2.251	0.907	-111.675*

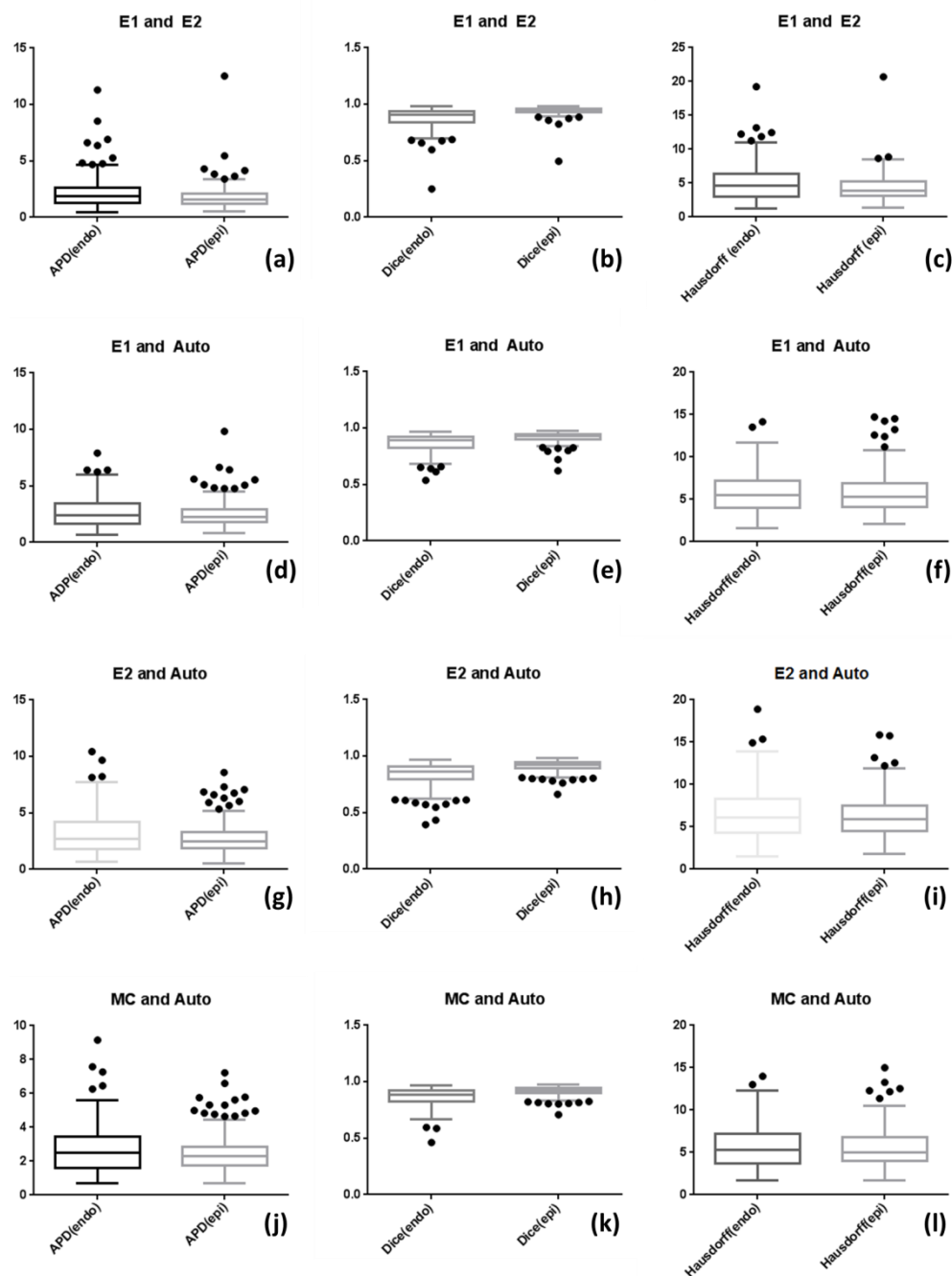


Figure 6.9 - Validation of the (semi-) automatic segmentation technique. First line, test the intra-observer variability, the second line compare the first observer with the proposed method, the third line present the result between the second observer and the (semi-)automatic approach and the last line shows the results between a mean contour and the (semi-) automatic approach. The comparison was performed in terms of APD (average perpendicular distance) – first column, dice value – second column, and Hausdorff value – third column.

6.4. Validation of the proposed sequential 2D+t FFD formulation

Figure 6.10a shows an example of a global strain curve. The panel (b) illustrates the differences between the sequential 2D and the proposed method in terms of the trajectories of individual points.

Figure 6.11a presents a global strain map illustrating the influence of σ_t on the performance of the proposed 2D+t approach. The contours are obtained using the automatic segmentation method. Using the same values for σ_t , panel (b) shows the differences in terms of the trajectories of individual points.

Figure 6.12 shows the differences between the methodology proposed (sequential 2D+t) and the state-of-the-art approach (fixed 2D+t).

Figure 6.13 shows the result in terms of contour propagation during the cardiac cycle using the fixed 2D+t formulation presented in [68]. The first line uses the *SSD* as metric, while the second line uses the *NMI*.

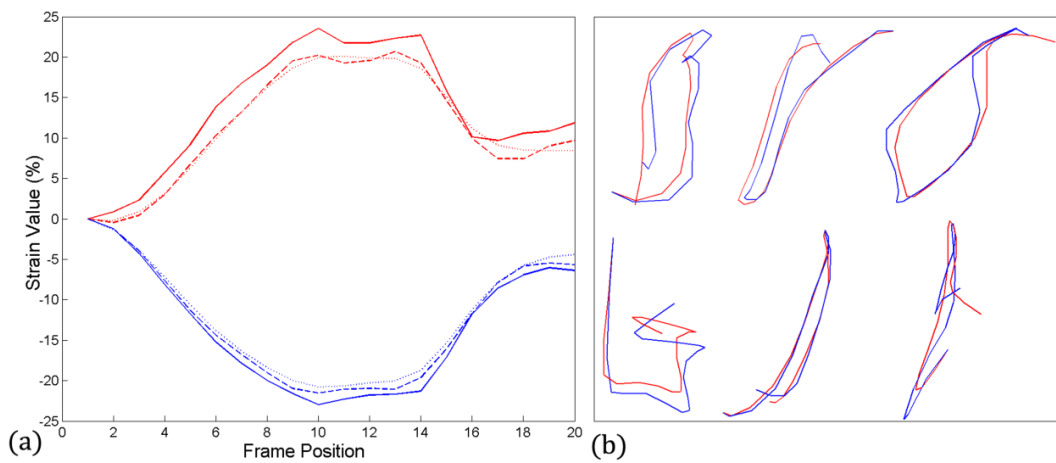


Figure 6.10 - (a) Global radial (red) and circumferential (blue) strain by using different methodologies: (solid line) the sequential 2D, (dotted line) sequential 2D+t using equation (4.7) and (dashed line) sequential 2D+t using equation (4.10) [proposed]. (b) Tag trajectory examples showing the difference between (blue) sequential 2D and (red) the sequential 2D+t approach.

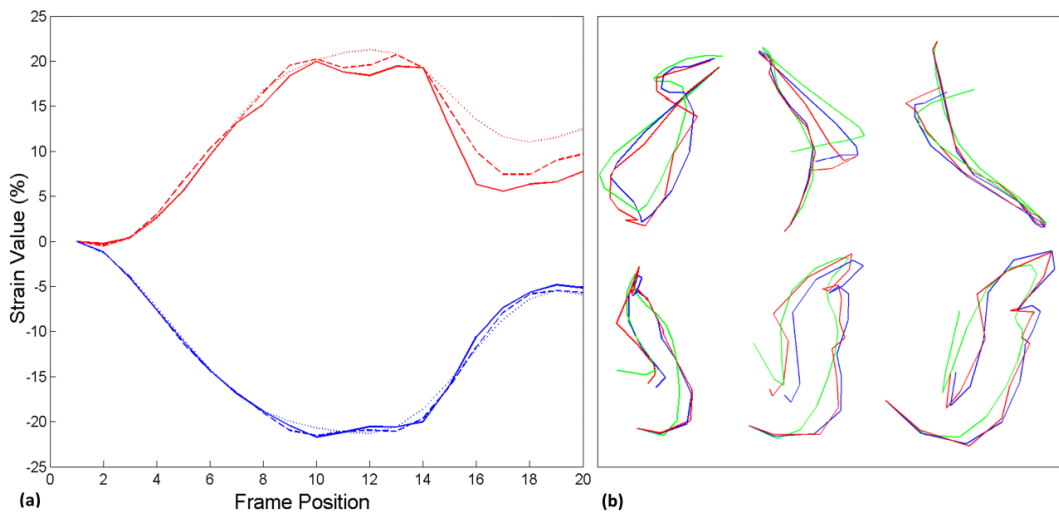


Figure 6.11 - (a) Global radial (red) and circumferential (blue) strain by using different spacing in time direction: (dotted line) $\sigma_t=3$, (dashed line) $\sigma_t=2$ and (solid line) $\sigma_t=1$. (b) Tag trajectory examples showing the difference between the proposed 2D+t approach with (blue) $\sigma_t=1$, (red) $\sigma_t=2$ and (green) $\sigma_t=3$.

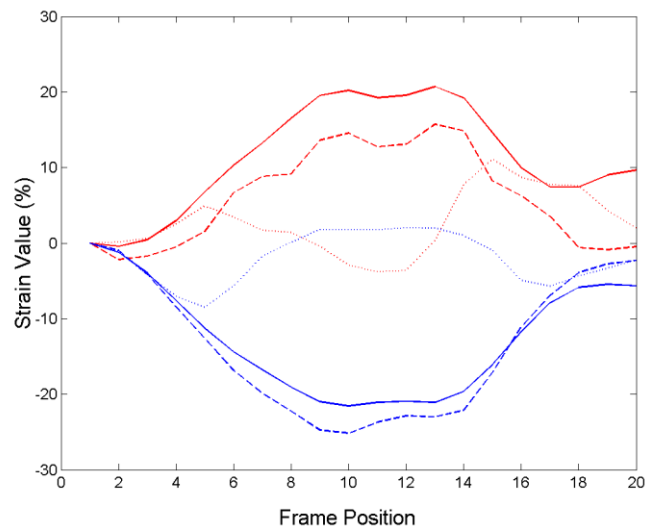


Figure 6.12 - (a) Global radial (red) and circumferential (blue) strain using different methodologies; (solid line) proposed sequential 2D+t approach, (dashed line) fixed 2D+t approach using *NMI* and (dotted line) fixed 2D+t approach using *SSD* as metric.

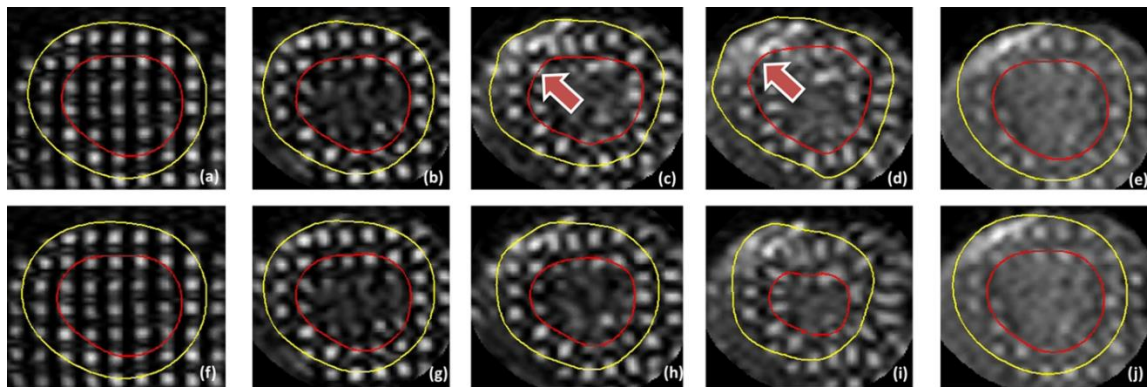


Figure 6.13 - Validation of the methodology proposed for the fixed 2D+t FFD formulation presented in [70]. The first line shows the results using *SSD* and in the second line we present the results in terms of contour propagation using the *NMI*. In each line, the third and fourth columns are consecutive frames. The red arrow represents the “jump” of one frame between consecutive frames.

6.5. Comparison of the proposed algorithm with a commercial state-of-the-art solution

Study 1

Table 6.3 presents the results from the multi-center study in terms of linear regression and Bland-Altman analysis. In this table, we are comparing the result with different methodologies (sequential 2D and sequential 2D+t FFD formulations) in the ES defined by physicians.

Cardiac motion and deformation estimation in tagged magnetic resonance imaging

Figure 6.14 shows the correlation between the commercial software and proposed method (*NRR*) and the Bland-Altman analysis for the best result in the Table 6.3 (sequential 2D+t with $\sigma_t = 1$).

Table 6.4 indicates the results from the multi-center study in terms of linear regression and Bland-Altman analysis. This analysis focuses only on the segmental circumferential strain. In this table, we are comparing the result using different methodologies (sequential 2D and sequential 2D+t). Based on the results of this table, we illustrate in the Figure 6.15 the best result (sequential 2D+t with $\sigma_t = 1$), using linear regression between the commercial software and proposed framework. The Bland-Altman analysis is also shown.

Table 6.3 - Results from Doppler CIP study, in terms of global circumferential strain, using different methodologies. *Statistically significant ($p < 0.05$)

Study	Method	Correlation Coefficient (r)	Bland-Altman Analysis	
			Bias	LOA ($\mu \pm 1.96\sigma$)
1	Sequential 2D	0.242	4.815*	[-6.568;16.198]
2	Sequential 2D+t ($\sigma_t = 1$)	0.260	4.196*	[-7.222;15.616]
3	Sequential 2D+t ($\sigma_t = 2$)	0.232	4.161*	[-7.334;15.655]
4	Sequential 2D+t ($\sigma_t = 3$)	0.248	4.131*	[-7.61;15.274]

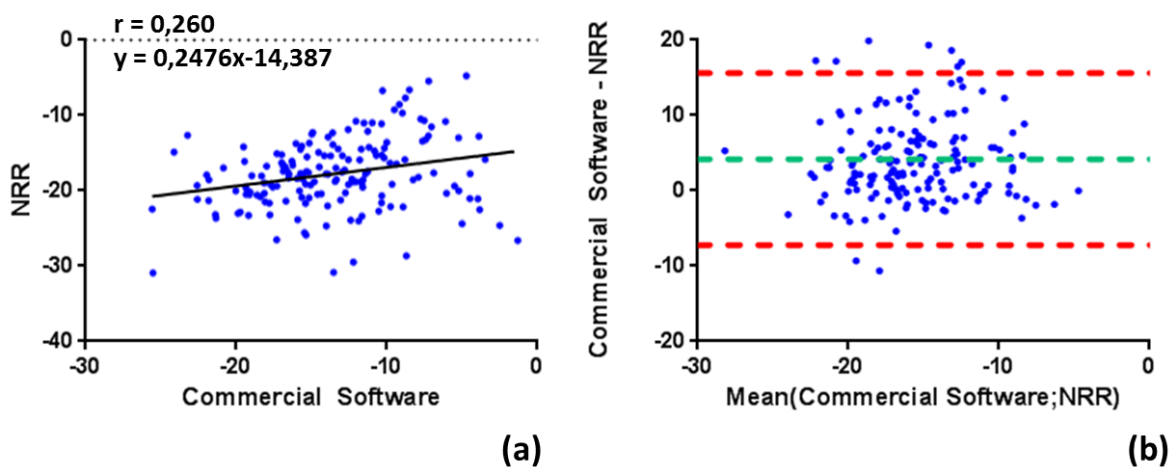


Figure 6.14 - (a) Linear regression, and (b) Bland-Altman Analysis in terms of global circumferential strain.

Table 6.4 - Results from Doppler CIP study, in terms of segmental circumferential strain, using different methodologies. *Statistically significant ($p < 0.05$)

Study	Method	Correlation Coefficient (r)	Bland-Altman Analysis	
			Bias	LOA ($\mu \pm 1.96\sigma$)
1	Sequential 2D	0.182	4.834*	[-14.113;23.784]
2	Sequential 2D+t ($\sigma_t = 1$)	0.188	4.358*	[-14.607;23.323]
3	Sequential 2D+t ($\sigma_t = 2$)	0.182	4.306*	[-14.804;23.416]
4	Sequential 2D+t ($\sigma_t = 3$)	0.178	3.985*	[-15.454;23.425]

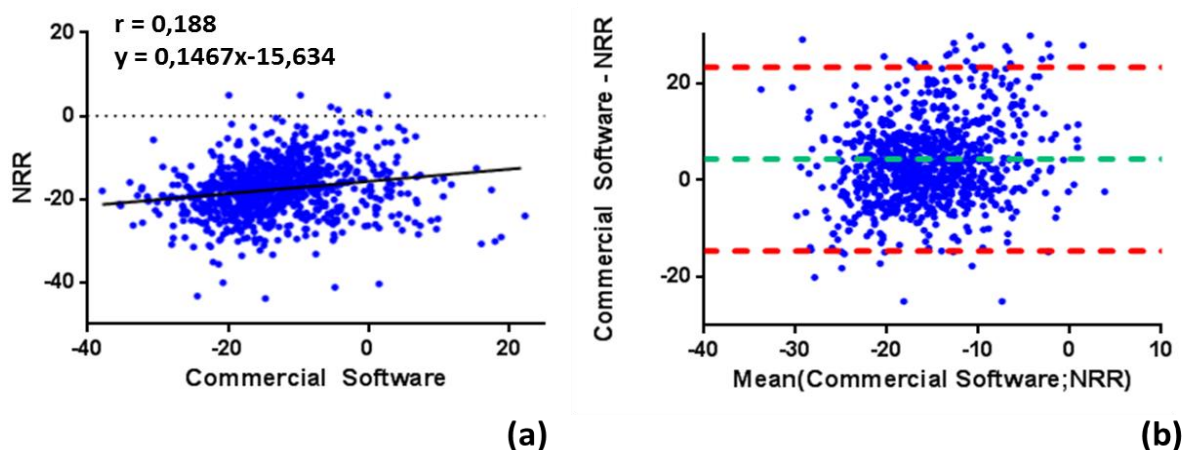


Figure 6.15 - (a) Linear regression, and (b) Bland-Altman Analysis in terms of segmental circumferential strain.

Study 2

The normal procedure used by the physician to detect the ES moment, consists in searching for the frame where the area of the endocardium is lower. This is a subjective process, which can create an error of 1 or 2 frames.

Some works [118] use the circumferential peak value as an important clinical indicator. Since this methodology was previously applied and accepted, we compare the peak value, obtained with the proposed method, with peak value from the commercial-software. We present in Table 6.5 and Table 6.6 the results for the global and segmental strain, respectively.

Figure 6.16 and Figure 6.17 show the linear regression between the *diagnosoft-HARP* and the proposed framework and the Bland-Altman analysis for the best situation in Table 6.5 (sequential 2D+t with $\sigma_t = 1$) and Table 6.6 (sequential 2D).

Cardiac motion and deformation estimation in tagged magnetic resonance imaging

Table 6.5 - Results from Doppler CIP study, in terms of global circumferential strain, using different methodologies. *Statistically significant ($p < 0.05$)

Study	Method	Correlation Coefficient (r)	Bland-Altman Analysis	
			Bias	LOA ($\mu \pm 1.96\sigma$)
1	Sequential 2D	0.591	2.561*	[-4.736;9.858]
2	Sequential 2D+t ($\sigma_t = 1$)	0.601	1.965*	[-5.322;9.252]
3	Sequential 2D+t ($\sigma_t = 2$)	0.598	1.750*	[-5.568;9.068]
4	Sequential 2D+t ($\sigma_t = 3$)	0.596	1.211*	[-6.223;8.646]

Table 6.6 - Results from Doppler CIP study, in terms of segmental circumferential strain, using different methodologies. *Statistically significant ($p < 0.05$)

Study	Method	Correlation Coefficient (r)	Bland-Altman Analysis	
			Bias	LOA ($\mu \pm 1.96\sigma$)
1	Sequential 2D	0.353	1.755*	[-12.038;15.549]
2	Sequential 2D+t ($\sigma_t = 1$)	0.339	1.294*	[-12.216;14.805]
3	Sequential 2D+t ($\sigma_t = 2$)	0.334	1.172*	[-12.613;14.957]
4	Sequential 2D+t ($\sigma_t = 3$)	0.332	0.537	[-13.438;14.513]

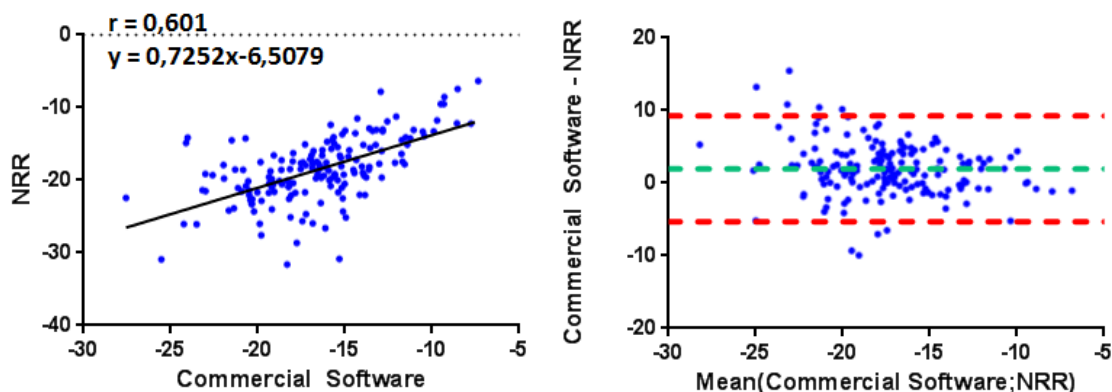


Figure 6.16 - (a) Linear regression, and (b) Bland-Altman Analysis in terms of global circumferential strain.

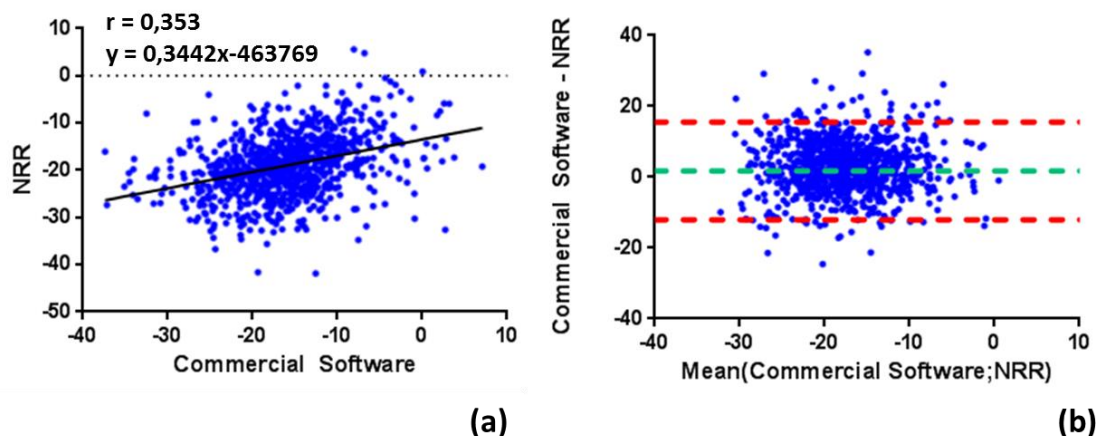


Figure 6.17 - (a) Linear regression, and (b) Bland-Altman Analysis in terms of segmental circumferential strain.

Analysis of the strain peak values

Table 6.7 and Table 6.8 compare the mean strain value, using the global strain and segmental strain (both cases using the peak value as reference) in the commercial software and the proposed framework, respectively. The global strain value, suggest differences between the two methods that are statistically significant ($p < 0.05$).

Table 6.9 shows the ANOVA study, based on the segmental strain peak values, for the *HARP* and the proposed method. The homogeneity was achieved by removing 5% of the cases, which were outlier's points. Statistically, the elimination of this percentage is acceptable and not statistically significant. The validation of present study is available on the Appendix VIII.

Figure 6.18 illustrates the difference in terms of marginal mean value for the commercial software and the proposed method. The figure is based on the Table 6.9 and we remove the outliers, as indicated before. In the commercial software there are no differences statistically ($p < 0.05$) significant between the apical and mid slice. In the other situations, the differences are statistically significant.

Table 6.7 – Mean strain value in terms of global circumferential strain. The mean result for the commercial software and the proposed approach (NRR) are shown

Software	Mean value for the global circumferential strain (%)
<i>diagnosoft-HARP</i>	-16.533
NRR	-19.094

Cardiac motion and deformation estimation in tagged magnetic resonance imaging

Table 6.8 – Mean strain value in each slice for the different segments (S1, S2, S3, S4, S5, S6). The segmental peak results are used. In each slice we present the strain result for the commercial software and the proposed approach (NRR)

Slice	Software	Mean value for each segment in terms of circumferential strain (%)					
		S1	S2	S3	S4	S5	S6
Apical	<i>diagnosoft-HARP</i>	-18.449	-15.307	-17.497	-17.471	-	-
	NRR	-20.973	-19.248	-19.337	-21.015	-	-
Mid	<i>diagnosoft-HARP</i>	-18.782	-15.735	-15.735	-15.075	-16.046	-17.856
	NRR	-15.624	-18.941	-18.730	-17.928	-18.822	-21.425
Base	<i>diagnosoft-HARP</i>	-18.872	-15.590	-14.857	-12.743	-14.639	-17.164
	NRR	-17.395	-16.995	-16.965	-15.799	-15.748	-20.168

Table 6.9 - ANOVA table using the segmental peak strain results in each slice for the different software's presented

Source	Sum of squares	DOF	Mean Square	Fischer value	Significance
Slices	1366.1	2	683.05	23.274	0.000
Software	3212.689	1	3212.689	109.469	0.000
Slice and Software	268.406	2	134.203	4.573	0.010
Error	55262.180	1883	29.348		
Total	60109.375	1888			

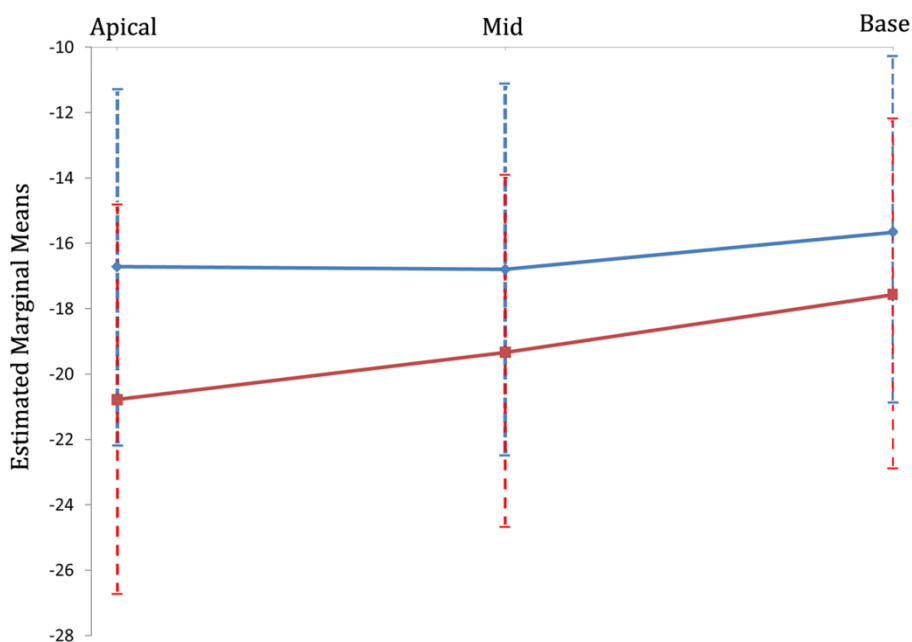


Figure 6.18 - Estimated Marginal Means values for each slice. The blue line represents the commercial software, and the red line the proposed methodology based on registration.

Discussion

7. Discussion

7.1. Parameter tuning

Based on the results presented in Figure 6.1, it is evident that, using different values for the final grid spacing or different registration metrics, a sub-pixel accuracy is achieved in terms of RMSE and EES. In all the cases, the differences between the sequential 2D and the proposed sequential 2D+t approach are small. The best result in terms of RMSE is 0.2 and 0.18 pixels for the sequential 2D and the sequential 2D+t approaches, respectively. In terms of EES, the best result was 0.23 and 0.25 pixels for the sequential 2D and sequential 2D+t, respectively.

A comparison between the three metrics proposed, suggests that the *SSD* has the best result, but with a small difference relative to the *NMI*. In Figure 6.1, the *MMI* appears to have the worst result, but keeping the sub-pixel accuracy, what is satisfactory. Another difference is related to the value of ω_{BE} . In the *SSD*, high values should be used, since it is a metric based on the difference in terms of intensities between the two images, while in the *MI* a range between 0-12 should be used, due the probability value associated with this metric.

About the influence of the ω_{BE} in each metric, we can observe that high value leads to worst result in terms of RMSE and EES error, due a high regularization; on other hand, a lower value will lead to worst results, which happens due the large degrees of freedom allowed. In the case of *SSD* a value in the range [1000-10000] and the *MI* approaches a value in the range [0.5 – 2] should be used.

In Figure 6.2 is possible to see the influence of 4 scales, instead the 3 scales previously used (multi-resolution technique used in the registration problem). At the same time, in Figure 6.3, the influence of 64 bins used during the computation of the joint histogram is shown. In these results, no big difference between the different parameters was found, suggesting some robustness for the current methodologies.

Regarding the image with lower SNR (Figure 6.4), the results revealed a high value for the RMSE and EES. In this case, it is possible to see that a metric based on *MI* has a better result than *SSD*. This was expected, since the *MI* approach is not based on the intensity of the image, but on the histogram of the image. As such, it is more appropriate for images with noise. Looking in Figure 6.4, it is also possible to observe no big differences between different final grid spacing values. In terms of ω_{BE} , a performance similar to the image with high SNR was found, but with other ranges for

the optimum result. This last observation proves that a study about the regularization factor is essential, when we change the properties of the image. The best result for the *SSD* in terms of RMSE is 2.68 and 3 pixels for the sequential 2D and the proposed sequential 2D+t with optimal range for the ω_{BE} between [10000-1000000]. About the result with Mutual Information, the *MMI* has the best result in terms of RMSE of 1.76 and 1.52 pixels for the sequential 2D and the proposed sequential 2D+t, respectively. In terms of EES, the best result was 2.35 and 2.16 pixels for sequential 2D and sequential 2D+t, respectively, using a range between [1-5] for ω_{BE} . Relatively the *NMI*, the best result was 2/3.45 and 1.58/2.36 pixels for the RMSE/EES with optimal range between [0.5-5]. In Figure 6.5, the RMSE and EES results using 4 scales instead 3 scales are shown. Again, no big difference was found between the two results, proving that ω_{BE} is the factor with higher impact on the final result of the registration problem.

As a final comment, it is important to note that the image with SNR = 6dB is an “extreme” situation, where the influence of the noise might be big. In clinical t-MRI, image quality is generally better, and the results obtained in the image with SNR = 18dB (Figure 6.1) should be used as a reference for the parameter study.

7.2. Detection of (dys)functional regions

Figure 6.6 illustrates that the sequential 2D and the proposed sequential 2D+t show reduced (and even inversed) strain values at the lesion location as identified in the corresponding DE-MRI image. The center of the lesion was more clearly visible in the circumferential strain map, compared to the radial strain map. The inverse strain pattern seen in the circumferential strain map is likely caused by passive stretching due to the contraction of the neighboring viable segments. However, in the radial strain map, part of the lesion was (wrongly) classified as having a high positive strain value (represented as a red area). These detection errors in the strain map may be related to the initial segmentation which was used to delineate a ROI for strain estimation, or due to the influence of the papillary muscle on tracking accuracy. The difference between the strain map of both methods is also small. This is expected, since the sequential 2D+t approach does not impose additional spatial smoothing.

In Figure 6.7, the strain map of a healthy heart is shown. In that case, both approaches were capable to estimate an acceptable strain map for the image. The regions that are presented as a blue (represent a lesion) typically appear on the borders of the contour, suggesting that this can happen due the manual initial segmentation.

The statistic study available in the Figure 6.8 demonstrates that both approaches were capable to separate dysfunction from normal regions. The circumferential strain seems best suited for this purpose. No significant differences were found between the adjacent region and the normal or infarct region. Nevertheless, the strain behavior was as expected, with an increasing strain gradient from infarct to normal tissue. It should be noted that the present segmental classification may be too coarse as the infarct borders from the DE-MRI images did not necessarily coincide with borders between the standard segments. Adapting this classification may thus improve these results.

7.3. Validation of the (semi-) automatic segmentation approach

Table 6.1 and Table 6.2 show high intra-observer variability. This is expected, due the presence of tags. Normally some observers adapt the contours to the limit of the tags and others prefer to use a mean tag position. This difference can cause large variability in the final result, since one tag typically has 3 or more pixels. At the same time, since the experts need to look in the temporal direction to detect the endocardium and epicardium, due the image noise, some errors in the manual segmentation are expected. As a last comment, the non-experts remarked that this task was tedious and the differences, in terms of dice value, APD value and Hausdorff distance, between the observers are acceptable. In clinical practice, we expect a similar result.

Comparing each non-expert (E1 and E2) with the automatic result, it is possible to see that the differences, in terms of Dice, APD and Hausdorff distance are higher than in the last situation, particularly in the case of E2. This result is expected, since the automatic approach will remove the intra-observer variability, presenting always the same behavior.

In terms of Dice value and APD value, the epicardium has a better result than the endocardium. This is not expected, since if we analyze the tracking results of the contours, the endocardium appears to have a more robust result than the epicardium. These differences can prove that the actual “ground truth” could present some errors, but these problems are related with properties of the t-MRI images. If we analyze the correlation coefficient in terms of area, we also observe a best result for the epicardium.

Looking for the BIAS value, we can observe that E1 and E2 typically draw an endocardium more inward than the automatic approach and an epicardium more outward than the automatic approach.

To solve the limitation related with intra-observer variability, we created a mean contour between the E1 and E2. The results obtained are in accordance with the previous observations.

Figure 6.9 presents a detailed statistic study about the contours. This result supports the previous observations. It is important to mention that with this task we intend to validate the proposed (semi-) automatic methodology, but we are not comparing with a benchmark database. As such, these results demonstrate that the proposed approach can create an acceptable contour.

Finally, during the discussion we refer that we are using a (semi-) automatic approach, but initially we propose to develop an automatic methodology. All the work was focused on an automatic methodology, but due the high variability of the images and problems during the acquisition (e.g. heart is not in the center of the image) in some situations a user input was used. Appendix II indicates the number of cases where the physician needs to insert some information, for example the LV position. It is important to mention that the user input was used in a small number of cases. In these cases, the physician only needs to click one or two times on the image, which is less time consuming than manual segmentation. As such, the results suggest that this framework could be useful for the physician. About the number of apical fails (Table 11.1), in all these cases the physician was also not capable to process the image.

7.4. Validation of the proposed sequential 2D+t FFD formulation

In the next part of the discussion, we focus on difference between the registration scheme described in the section 3.1.7 (sequential 2D) and the approaches proposed in the section 4.3 (sequential 2D+t and fixed 2D+t).

Using the automatic contours we intend to assess the different methodologies proposed for tracking. The motion and strain behavior seen in Figure 6.10, which is temporally smoother for the proposed 2D+t approach, is also in line with expectations. Taking motion estimates from neighboring frames into account eliminates noisy or jaggy motion trajectories caused by the original assumption that pairwise registrations are independent. Furthermore, by adapting the BE formulation (equation 4.10), an over-smoothing effect of the strain curves can be avoided. In this situation, the over-smoothing effect is not so big, but it is possible to see a strain curve really similar to a B-spline. The high influence of the adaptation of BE formulation can be shown in a published result by Morais *et al.* [117] (Appendix IV).

Figure 6.11 shows the influence of the B-spline spacing factor on the time directions. The results prove, as expected, that if we increase this factor, a larger smoothness effect can be observed. Increasing the spacing implies that we are using information from more distant frames. Due to use of B-splines in the transformation, large temporal grid spacing will increase the smoothness of the global strain curve. A small value should be used on this parameter to prevent an over-smoothed result.

To validate the proposed methodology, we decided to create a comparison with a state of the art approach, using temporal information on the transformation model. The work proposed by Chandrashekara *et al.* in 2004 was implemented, during the development of this master thesis, based on the information presented in the paper published in [70]. Initially, we implemented the methodology using *SSD*. Since in the fixed 2D+t approach we are registering each frame in the cardiac cycle with the first frame, highest differences are expected in term of intensities. This factor is problematic in the case of t-MRI, since the ED frame presents different contrast and tags on the blood pool. Using *SSD*, we are not capable to estimate the motion field (Figure 6.12 – dotted line), and it is possible to see that the contours typically fail in the frames with biggest deformation (first line in Figure 6.13). During these phases, the contours typically have biggest changes between consecutives frames and it is possible to see a “jump” of almost one tag spacing (first line in Figure 6.13).

Using the same methodology as a reference, the fixed 2D+t, we implemented a new non-intensity based metric, called Mutual Information. Two approaches were available, *MMI* and *NMI*. We were only capable to estimate the motion field with *NMI*. The result presented in Figure 6.12 (dashed line) and in Figure 6.13 (second line), suggests that this methodology can estimate an acceptable strain curve result. No reason was found to explain why *MMI* fails to compute the motion field, but this can be related with the parameters used. Finally, we compared the result between the fixed 2D+t using *NMI* and the proposed approach using *SSD* (proposed sequential 2D+t), and it was possible to see a more smooth effect and a more normal curve in the proposed sequential 2D+t. During the current master thesis, we don't study the parameters for the fixed 2D+t approach using normalized mutual information. The parameters used for the computation of the strain curve were obtained using the reference values from the study realized in Figure 6.1. Possibly, this parameter study could improve the final result of the fixed 2D+t method, but we don't expect a more smooth effect on fixed 2D+t methodology, when compared with the proposed sequential 2D+t approach.

7.5. Comparison of the proposed algorithm with a commercial state-of-the-art solution

Initially, we intend to discuss the feasibility of the proposed method. The new method was capable to segment and estimate the strain value in all the cases. As such, a feasibility of 100% was achieved.

Now, during the next step of the discussion, we will compare the cardiac strain values between the commercial software and the proposed methodology, based on elastic registration. We intend to assess the circumferential strain value in the ES frame, since this is an important indicator about heart function. Two studies were proposed to compare the two methodologies. The first is based on the ES defined by the physician using visual assessment (searching for the frame where the endocardium present a lower area); and the second study is based on the peak value between the *diagnosoft-HARP* and the proposed approach.

Initially, in Appendix V a problem of the *HARP* results is detected. The t-MRI sequences normally do not contain a full cardiac cycle, so the circumferential strain should never be higher than zero. A value of zero means that the heart recovers the original shape and a value higher than zero means that the heart is not contracting correctly. Obviously, these values can happen in the case of abnormal heart function (e.g. infarct region), but all the results from the core lab have the same problem (values high than zero in terms of circumferential strain in the end of the dataset). The current dataset has abnormal situations, but also has normal cases. This is not limitative, since we only want to study the strain at the ES. The proposed methodology also has some problems at the end of the cycle, due to the loss in the image contrast, but we never achieve a circumferential strain value higher than zero, which is not normal in clinical practice.

One possible explanation for the results obtained with the *HARP* technique, is related to tag fading. At the end of the cycle, the *HARP* method, which is based on the study of the frequency, typically fails since the peaks on FFT (as demonstrated in Figure 4.7) start to disappear. Without the peaks, the *HARP* method is not capable to compute the correct phase image and consequently it is not capable to estimate the strain value.

Other problem referred by the physician is related with tag orientation. The commercial software is prepared to estimate strain in images with tags at 45° . During this study, one of the centers is using tags at 0° , so the physician needs to rotate the

image to estimate the strain. The proposed approach is better on this point, since we don't assume any tag orientation, and the results prove that we can estimate the strain with tags at 0° and 45° .

In terms of global strain values, Table 6.3 presents a low correlation coefficient between the two strategies and has a positive BIAS statistically significant (best result with $r = 0.260$). The ES frame defined by the physician was obtained by visual assessment, which can create some errors. Other problem is related with the *HARP* result. As referred before, we removed from the study the cases where the circumferential strain is higher than zero at ES. This assumption works as a "threshold", and the cases where the value of the strain is approximately zero are included (see Figure 6.14a). Obviously, these cases will influence the correlation and a low value is expected. The Bland-Altman analysis presented in Figure 6.14 shows the high value of the BIAS and a large limit of agreement, which prove a high variability on the result. Table 6.4 and the respective Figure 6.15 are consistent with the last conclusions, but in this case we are using the segmental strain (best situation with $r = 0.188$). In terms of results, we expect always worst values on the segmental study, due the regional analysis. It is important to note, that the segments were defined by the model proposed by Cerqueira *et al.*[111], but some variability on the limits can occur between the result with the proposed approach and the core lab analysis.

The previous results were not capable to validate the proposed methodology, and more statistical tests should be done to see if there is some correlation between the commercial software and the proposed method.

In the second test, we compare the strain peak value between the *diagonosft-HARP* and the elastic registration methodology [118]. It is important to mention that since we are using core lab analysis, we do not have access to the initial contour of the image, which has a high impact on the strain estimation. Based on this difference a high correlation between the two methodologies is not expected.

The results obtained during this study suggests an acceptable value for the correlation coefficient ($r = 0.601$ and $r = 0.353$ for the best situation in the global and segmental strain, respectively) between the two software's and a statistically significant BIAS in the case of global strain (see Table 6.5 and Figure 6.16) and segmental strain (see Table 6.6 and Figure 6.17), which prove that the proposed methodology typically presents a peak value more negative than the commercial software. This last point is important, and can be explained due the method used by the

physician for the definition of the endo- and epicardial contour. Due the difficulties to understand some results obtained by the commercial software, we inquire the physician about the technique used for the definition of the endocardium and epicardium. This definition is done using manual segmentation, and the physician does not draw the contours in the endocardium structure, but a little bit within the myocardium, following the recommendation by the inventor of the software. Obviously, this difference in the definition of the endocardial contour can explain the BIAS and prove why we typically have a lower value, as presented on the Table 6.7 and Table 6.8. In this second study was possible to observe that the limits of agreement are not so large, so we can see a decrease on the variability of the data. Comparing the sequential 2D and the proposed sequential 2D+t methodologies, no statistically significant differences were found. Again, we showed that the smoothness on the temporal direction is the principal advantage of the sequential 2D+t methodology when compared with the sequential 2D.

The Appendix VI presents the result of the second test (comparison between peak values) in each slice. The results prove that the basal slice has the most acceptable correlation ($r = 0.755$) and the apical slice the lowest correlation ($r = 0.446$). This is expected and this proves why the basal slice is the best option, in t-MRI, for start the automatic segmentation approach.

In Appendix VII, we propose a different study to compare the two methodologies. Using the *diagnosoft-HARP* results as a “viable ground truth”, which is adequate since it is the generally accepted commercial software, we use the strain peak value to define the ES frame. After, using this frame we determine in the proposed methodology the respective strain value. This study, shows the highest correlation ($r = 0.691$ and $r = 0.408$ for the global and segmental strain, respectively) comparing with the two studies presented before (ES defined by physician and the strain peak value). In terms of Bland-Altman analysis, we can see that the limits of agreement have the most acceptable results. This appendix, suggests that the proposed approach has a high correlation with the *HARP* result until the *HARP* peak value, after that, the commercial software start failing. This observation is valid for the global (Table 16.1 and Figure 16.1) and the segmental circumferential strain (Table 16.2 and Figure 16.2).

In Table 6.8, it is also possible to observe a gradient between the apical and basal slice. Looking for the results obtained with the proposed method, we can see that the apical slice has a high strain value and this value reduces in all the segments towards

the base. This is expected in the clinical practice. The same behavior is not observed in all the slices of the commercial software, which was not expected and can be analyzed as a drawback of the current commercial software. A statistical study, based on the ANOVA table (Table 6.9) proves that there are statistically significant differences in the combination, different software's and different slices. The differences can be easily seen on the Figure 6.18, where the proposed method has a linear behavior. The same is not visible on the commercial software.

During the discussion, we are creating some suspicions about the current commercial software. To detect what method is better to estimate the cardiac strain value, a fair comparison should be done in future work, using a phantom. The proposed approach appears to present more adequate results. The same can be observed, if we study the difference between the ES defined by the physician, and the ES frame defined by the strain peak value. The results show that the absolute difference is 1.637 and 1.363 frames for the commercial software and the proposed methodology, respectively (statistically is not significant using a paired t-test with $p < 0.05$). Without the absolute value, the final results are 1.230 and -1.129 frames, for the *diagnosoft-HARP* and registration approach, respectively. This result proves that the ES (using as reference the strain peak value) in the *HARP* occurs before the ES defined by the physician, while in proposed approach occurs after. A global analysis about the last results, suggests that the proposed methodology appears to be more robust than the commercial software.

Conclusions and Contributions

8. Conclusions and contributions

8.1 Conclusions

In conclusion, this work presents an automatic framework to estimate the LV deformation in t-MRI. The LV tracking and segmentation methods are described and validated, showing acceptable results for clinical practice.

In this work, different registration schemes to track tissue motion and to estimate cardiac deformation from t-MRI are described. A pairwise approach termed the sequential 2D is first explained. The results suggest that the method can estimate the motion field, but with the general assumption that there is independence between registrations. A sequential 2D+t approach is presented to solve the last assumption and the results show a smoothing effect in the strain curve. At same time, we describe a state-of-the art technique, termed as fixed 2D+t. This method was capable to estimate the motion field using non-intensity based metric, but without a high smoothing effect in the temporal direction. As such, the proposed sequential 2D+t appears to be a more adequate methodology. More tests should be done in future work.

No significant differences were found between the sequential 2D and sequential 2D+t approaches in the detection of the dysfunctional regions. More exams and a refinement of the segments should be used to improve the results.

In future work, we intend to improve the proposed sequential 2D+t. Currently, this methodology was only applied on short axis data. Out-of-plane motion may have therefore introduced additional errors. Including longitudinal strain measurements from long-axis views or extending the method to 3D tagged MR images may further extend its appeal. Furthermore, the analysis of the clinical dataset is not straightforward. As such, we intend to apply the current strategy in the recent STACOM challenge [119].

Regarding the proposed segmentation approach, a technique to automatic define of the LV contours was not achieved. We proposed a strategy for automatic definition of the myocardium, but the results prove that in a few cases a user input, based in one or two clicks, was needed. As a result, we develop a (semi-) automatic approach, where we remove the tedious task, related with the manual segmentation, and the intra-observer variability.

The semi-automatic approach used for LV contouring presents acceptable results, when compared with the manual segmentation. In future work, a benchmark database should be used to validate the methodology.

A comparison between the proposed framework (LV tracking and segmentation) and the commercial software (*diagnosoft-HARP*) to estimate cardiac deformation in t-MRI is shown. Several problems were detected in the commercial software, but these problems are related with the manual contouring used. Since we are using a core lab analysis, we don't have any information about the initial endo- and epicardial contour. As such, some differences in the strain curves are expected. The two techniques appear to have an acceptable correlation, when we compare the strain peak values. The same is not observed, if we use the ES frame defined by the physician. In future work, we intend to develop a phantom to compare, with high accuracy, the two methods.

As last conclusions, the entire proposed framework can estimate, with acceptable results, the global and segmental strain curve. At the same time, a global analysis of all the results suggests that the proposed framework appears to be more adequate than the currently available commercial software to estimate motion in t-MRI images.

8.2 Contributions

The main contributions during the present master thesis are as follow:

1. A new registration formulation was proposed (sequential 2D+t), where the time was included on the transformation model formulation.
 - a. Validation of the new methodology was performed in synthetic, porcine dataset with dysfunctional regions and human clinical dataset;
 - b. A study about the parameters, such as bending energy factor, the final grid spacing and different similarity metrics was developed;
 - c. A new formulation for the strain estimation was developed;
 - d. A comparison between the proposed formulation (sequential 2D+t) and a state-of-the art approach (fixed 2D+t) was performed.
2. A study about active contours methods, with particular interest on the formulation of the BEAS [44] method was presented. At the same time, some studies were done about tag suppression methods using the t-MRI images.
 - a. Development of a methodology to automatic detection of the LV cavity and tag suppression in t-MRI images.
 - b. Development of a new technique for automatic initialization of the LV contours, based on the original t-MRI image. In this step, the template matching approach described in [33] is used.

- c. Application of the BEAS framework in t-MRI images, using the coupled myocardial segmentation method proposed in [33]. The method is not applied in the original image, but in an un-tagged image.
 - d. Validation of the (semi-) automatic approach used for LV contouring. We compare the results obtained using the proposed technique with a ground truth, created by two non-experts.
3. Using the entire framework we can automatically compute the radial and circumferential strain curves. A comparison between the proposed framework and the current commercial software was developed. The images used are obtained from a multi-center study with core lab analysis.
 - a. A statistical study was performed using as reference the ES frame defined by the physician.
 - b. In the second step, a comparison between the strain peak values in each strategy was shown. In this step, we also present the strain differences in each slice.
 - c. We detect a gradient, in terms of strain values, between the apical and basal slice. An ANOVA study was developed to validate the last observation.
 - d. Differences between the two strategies were detected, in terms of mean global and segmental strain. Also, a comparison between the ES in each strategy (using the peak value as reference) and the ES defined by the physician was presented.

References

9. References

- [1] A. M. Katz, *Physiology of the Heart*: Lippincott Williams & Wilkins, 2001.
- [2] A. Davies, A. G. H. Blakeley, C. Kidd, and J. G. McGeown, *Human Physiology*: Churchill Livingstone, 2001.
- [3] L. H. Opie, *The heart: physiology, from cell to circulation*: Lippincott-Raven, 1998.
- [4] E. Page, H. A. Fozzard, R. J. Solaro, and A. P. Society, *The cardiovascular system: The heart*: Published for the American Physiological Society by Oxford University Press, 2002.
- [5] W. F. Boron and E. L. Boulpaep, *Medical Physiology*: Elsevier Health Sciences, 2008.
- [6] <http://my.clevelandclinic.org/PublishingImages/heart/insideheart2.JPG> (30/09/2013).
- [7] K. L. Moore, A. F. Dalley, and A. M. R. Agur, *Clinically Oriented Anatomy*: Wolters Kluwer Health/Lippincott Williams & Wilkins, 2010.
- [8] A. Noble, *The cardiovascular system*: Elsevier Churchill Livingstone, 2005.
- [9] B. Hannaford and S. A. Glantz, "Adaptive linear predictor tracks implanted radiopaque markers," *Biomedical Engineering, IEEE Transactions on*, pp. 117-125, 1985.
- [10] E. Oubel, M. De Craene, A. O. Hero, A. Pourmorteza, M. Huguet, G. Avegliano, B. H. Bijmens, and A. F. Frangi, "Cardiac motion estimation by joint alignment of tagged MRI sequences," *Medical image analysis*, vol. 16, pp. 339-350, 2012.
- [11] M. De Craene, G. Piella, O. Camara, N. Duchateau, E. Silva, A. Doltra, J. D'hooge, J. Brugada, M. Sitges, and A. F. Frangi, "Temporal diffeomorphic free-form deformation: application to motion and strain estimation from 3D echocardiography," *Medical image analysis*, vol. 16, pp. 427-450, 2012.
- [12] W. Shi, X. Zhuang, H. Wang, S. Duckett, D. V. Luong, C. Tobon-Gomez, K. Tung, P. J. Edwards, K. S. Rhode, and R. S. Razavi, "A Comprehensive Cardiac Motion Estimation Framework Using Both Untagged and 3-D Tagged MR Images Based on Nonrigid Registration," *Medical Imaging, IEEE Transactions on*, vol. 31, pp. 1263-1275, 2012.
- [13] B. Heyde, P. Claus, R. Jasaityte, D. Barbosa, S. Bouchez, M. Vandenheuvel, P. Wouters, F. Maes, and J. D'Hooge, "Motion and deformation estimation of cardiac ultrasound sequences using an anatomical B-spline transformation model," in *Biomedical Imaging (ISBI), 2012 9th IEEE International Symposium on*, 2012, pp. 266-269.
- [14] A. Becciu, R. Duits, B. J. Janssen, L. M. Florack, and H. C. van Assen, "Cardiac motion estimation using covariant derivatives and helmholtz decomposition," in *Statistical Atlases and Computational Models of the Heart. Imaging and Modelling Challenges*, ed: Springer, 2012, pp. 263-273.
- [15] R. Chabiniok, P. Moireau, P.-F. Lesault, A. Rahmouni, J.-F. Deux, and D. Chapelle, "Estimation of tissue contractility from cardiac cine-MRI using a biomechanical heart model," *Biomechanics and Modeling in Mechanobiology*, vol. 11, pp. 609-630, 2012.
- [16] N. F. Osman, E. R. McVeigh, and J. L. Prince, "Imaging heart motion using harmonic phase MRI," *Medical Imaging, IEEE Transactions on*, vol. 19, pp. 186-202, 2000.
- [17] L. Axel, A. Montillo, and D. Kim, "Tagged magnetic resonance imaging of the heart: a survey," *Medical image analysis*, vol. 9, pp. 376-393, 2005.

- [18] W. Hui and A. A. Amini, "Cardiac Motion and Deformation Recovery From MRI: A Review," *Medical Imaging, IEEE Transactions on*, vol. 31, pp. 487-503, 2012.
- [19] L. Axel and L. Dougherty, "MR imaging of motion with spatial modulation of magnetization," *Radiology*, vol. 171, pp. 841-845, 1989.
- [20] T. J. Mosher and M. B. Smith, "A DANTE tagging sequence for the evaluation of translational sample motion," *Magnetic Resonance in Medicine*, vol. 15, pp. 334-339, 1990.
- [21] B. D. Bolster, E. R. McVeigh, and E. A. Zerhouni, "Myocardial tagging in polar coordinates with use of striped tags," *Radiology*, vol. 177, pp. 769-772, 1990.
- [22] E. R. McVeigh and E. Atalar, "Cardiac Tagging with Breath-Hold Cine MRI," *Magnetic Resonance in Medicine*, vol. 28, pp. 318-327, 1992.
- [23] S. E. Fischer, G. C. McKinnon, S. E. Maier, and P. Boesiger, "Improved myocardial tagging contrast," *Magnetic Resonance in Medicine*, vol. 30, pp. 191-200, 1993.
- [24] E. X. Wu, C. W. Towe, and H. Tang, "MRI cardiac tagging using a sinc-modulated RF pulse train," *Magnetic Resonance in Medicine*, vol. 48, pp. 389-393, 2002.
- [25] S. Ryf, M. A. Spiegel, M. Gerber, and P. Boesiger, "Myocardial tagging with 3D-CSPAMM," *Journal of Magnetic Resonance Imaging*, vol. 16, pp. 320-325, 2002.
- [26] D. A. Herzka, M. A. Guttman, and E. R. McVeigh, "Myocardial tagging with SSFP," *Magnetic Resonance in Medicine*, vol. 49, pp. 329-340, 2003.
- [27] C. C. Moore, C. H. Lugo-Olivieri, E. R. McVeigh, and E. A. Zerhouni, "Three-dimensional Systolic Strain Patterns in the Normal Human Left Ventricle: Characterization with Tagged MR Imaging¹," *Radiology*, vol. 214, pp. 453-466, 2000.
- [28] J. Bogaert and F. E. Rademakers, "Regional nonuniformity of normal adult human left ventricle," *American Journal of Physiology-Heart and Circulatory Physiology*, vol. 280, pp. H610-H620, 2001.
- [29] S. Ryf, J. Tsao, J. Schwitter, A. Stuessi, and P. Boesiger, "Peak-combination HARP: A method to correct for phase errors in HARP," *Journal of Magnetic Resonance Imaging*, vol. 20, pp. 874-880, 2004.
- [30] T. S. Yoo, *Insight into images: principles and practice for segmentation, registration, and image analysis* vol. 203: AK Peters Wellesley^ eMassachusetts Massachusetts, 2004.
- [31] J. Beutel and M. Sonka, *Handbook of Medical Imaging: Medical image processing and analysis*: Society of Photo Optical, 2000.
- [32] X. Chen, J. K. Udupa, U. Bagci, Y. Zhuge, and J. Yao, "Medical image segmentation by combining graph cuts and oriented active appearance models," *Image Processing, IEEE Transactions on*, vol. 21, pp. 2035-2046, 2012.
- [33] S. Queirós, D. Barbosa, B. Heyde, P. Morais, D. Friboulet, P. Claus, O. Bernard, and J. D'hooge, "Fast Fully Automatic Segmentation of the Myocardium in 2D Cine MR Images," in *Functional Imaging and Modeling of the Heart*, ed: Springer, 2013, pp. 71-79.
- [34] R. C. Gonzalez, *Digital Image Processing*: Pearson Education, 2009.
- [35] L. Rusko, G. Bekes, G. Nemeth, and M. Fidrich, "Fully automatic liver segmentation for contrast-enhanced CT images," *MICCAI Wshp. 3D Segmentation in the Clinic: A Grand Challenge*, vol. 2, 2007.
- [36] H. Fujimoto, L. Gu, and T. Kaneko, "Recognition of abdominal organs using 3D mathematical morphology," *Systems and Computers in Japan*, vol. 33, pp. 75-83, 2002.

-
- [37] F. Liu, B. Zhao, P. K. Kijewski, L. Wang, and L. H. Schwartz, "Liver segmentation for CT images using GVF snake," *Medical Physics*, vol. 32, p. 3699, 2005.
- [38] R. Malladi, J. A. Sethian, and B. C. Vemuri, "Shape modeling with front propagation: A level set approach," *Pattern Analysis and Machine Intelligence, IEEE Transactions on*, vol. 17, pp. 158-175, 1995.
- [39] A. X. Falcão, J. K. Udupa, S. Samarasekera, S. Sharma, B. E. Hirsch, and R. d. A. Lotufo, "User-steered image segmentation paradigms: Live wire and live lane," *Graphical models and image processing*, vol. 60, pp. 233-260, 1998.
- [40] H. Masoumi, A. Behrad, M. A. Pourmina, and A. Roosta, "Automatic liver segmentation in MRI images using an iterative watershed algorithm and artificial neural network," *Biomedical Signal Processing and Control*, vol. 7, pp. 429-437, 2012.
- [41] H. Park, P. H. Bland, and C. R. Meyer, "Construction of an abdominal probabilistic atlas and its application in segmentation," *Medical Imaging, IEEE Transactions on*, vol. 22, pp. 483-492, 2003.
- [42] J. Ma and L. Lu, "Hierarchical segmentation and identification of thoracic vertebra using learning-based edge detection and coarse-to-fine deformable model," *Computer Vision and Image Understanding*, 2013.
- [43] T. F. Cootes, G. J. Edwards, and C. J. Taylor, "Active appearance models," *Pattern Analysis and Machine Intelligence, IEEE Transactions on*, vol. 23, pp. 681-685, 2001.
- [44] D. Barbosa, T. Dietenbeck, J. Schaerer, J. D'hooge, D. Friboulet, and O. Bernard, "B-spline explicit active surfaces: An efficient framework for real-time 3-D region-based segmentation," *Image Processing, IEEE Transactions on*, vol. 21, pp. 241-251, 2012.
- [45] L. A. Schwarz, "Non-rigid Registration Using Free-form Deformations," Ph. D. dissertation, Dept. CS, Technische Univ., Munchen, German, 2007.
- [46] F. Maes, "Class of Advanced Medical Imaging - Image Registration," ed: Katholieke Universiteit Leuven, 2012-2013.
- [47] D. Loeckx, "Automated nonrigid intra-patient image registration using B-splines," PhD thesis, Katholieke Universiteit Leuven, 2006.
- [48] S. P. Allender S, Peto V, Rayner M, Leal J, Luengo-Fernández R, Gray A., "European cardiovascular disease statistics: 2008 edition," *London: British Heart Foundation*, 2008.
- [49] I. Smal, N. Carranza-Herrezuelo, S. Klein, W. Niessen, and E. Meijering, "Quantitative comparison of tracking methods for motion analysis in tagged MRI," in *Biomedical Imaging: From Nano to Macro, 2011 IEEE International Symposium on*, 2011, pp. 345-348.
- [50] W. S. Kerwin and J. L. Prince, "Cardiac material markers from tagged MR images," *Medical image analysis*, vol. 2, pp. 339-353, 1998.
- [51] A. A. Amini, Y. Chen, M. Elayyadi, and P. Radeva, "Tag surface reconstruction and tracking of myocardial beads from SPAMM-MRI with parametric B-spline surfaces," *Medical Imaging, IEEE Transactions on*, vol. 20, pp. 94-103, 2001.
- [52] S. Sampath, N. F. Osman, and J. L. Prince, "A combined harmonic phase and strain-encoded pulse sequence for measuring three-dimensional strain," *Magnetic resonance imaging*, vol. 27, pp. 55-61, 2009.
- [53] L. Pan, J. L. Prince, J. A. Lima, and N. F. Osman, "Fast tracking of cardiac motion using 3D-HARP," *Biomedical Engineering, IEEE Transactions on*, vol. 52, pp. 1425-1435, 2005.

- [54] K. Z. Abd-Elmoniem, N. F. Osman, J. L. Prince, and M. Stuber, "Three-dimensional magnetic resonance myocardial motion tracking from a single image plane," *Magnetic Resonance in Medicine*, vol. 58, pp. 92-102, 2007.
- [55] X. Liu and J. L. Prince, "Shortest path refinement for motion estimation from tagged MR images," *Medical Imaging, IEEE Transactions on*, vol. 29, pp. 1560-1572, 2010.
- [56] <http://www.diagnosoft.com/> (12/10/2013).
- [57] T. Arts, F. W. Prinzen, T. Delhaas, J. Milles, A. C. Rossi, and P. Clarysse, "Mapping displacement and deformation of the heart with local sine-wave modeling," *Medical Imaging, IEEE Transactions on*, vol. 29, pp. 1114-1123, 2010.
- [58] A. Montillo, D. Metaxas, and L. Axel, "Extracting tissue deformation using gabor filter banks," in *Medical Imaging 2004*, 2004, pp. 1-9.
- [59] Z. Qian, D. N. Metaxas, and L. Axel, "Extraction and tracking of MRI tagging sheets using a 3D Gabor filter bank," in *Engineering in Medicine and Biology Society, 2006. EMBS'06. 28th Annual International Conference of the IEEE*, 2006, pp. 711-714.
- [60] T. Chen and L. Axel, "Using Gabor filter banks and temporal-spatial constraints to compute 3D myocardium strain," in *Engineering in Medicine and Biology Society, 2006. EMBS'06. 28th Annual International Conference of the IEEE*, 2006, pp. 4755-4758.
- [61] P. Clarysse, C. Basset, L. Khouas, P. Croisille, D. Friboulet, C. Odet, and I. Magnin, "Two-dimensional spatial and temporal displacement and deformation field fitting from cardiac magnetic resonance tagging," *Medical image analysis*, vol. 4, pp. 253-268, 2000.
- [62] P. Radeva, A. Amini, J. Huang, and E. Marti, "Deformable B-solids and implicit snakes for localization and tracking of SPAMM MRI-data," in *Mathematical Methods in Biomedical Image Analysis, 1996., Proceedings of the Workshop on*, 1996, pp. 192-201.
- [63] J. Huang, D. Abendschein, V. G. Davila-Roman, and A. A. Amini, "Spatio-temporal tracking of myocardial deformations with a 4-D B-spline model from tagged MRI," *Medical Imaging, IEEE Transactions on*, vol. 18, pp. 957-972, 1999.
- [64] N. J. Tustison, V. G. Davila-Roman, and A. A. Amini, "Myocardial kinematics from tagged MRI based on a 4-D B-spline model," *Biomedical Engineering, IEEE Transactions on*, vol. 50, pp. 1038-1040, 2003.
- [65] N. J. Tustison and A. A. Amini, "Biventricular myocardial strains via nonrigid registration of AnFigatomical NURBS models," *Medical Imaging, IEEE Transactions on*, vol. 25, pp. 94-112, 2006.
- [66] J. Prince and E. McVeigh, "Motion estimation from tagged MR image sequences," *Medical Imaging, IEEE Transactions on*, vol. 11, pp. 238-249, 1992.
- [67] L. Dougherty, J. C. Asmuth, A. S. Blom, L. Axel, and R. Kumar, "Validation of an optical flow method for tag displacement estimation," *Medical Imaging, IEEE Transactions on*, vol. 18, pp. 359-363, 1999.
- [68] R. Chandrashekara, R. H. Mohiaddin, and D. Rueckert, "Analysis of 3-D myocardial motion in tagged MR images using nonrigid image registration," *Medical Imaging, IEEE Transactions on*, vol. 23, pp. 1245-1250, 2004.
- [69] D. Rueckert, L. I. Sonoda, C. Hayes, D. L. G. Hill, M. O. Leach, and D. J. Hawkes, "Nonrigid registration using free-form deformations: application to

- breast MR images," *Medical Imaging, IEEE Transactions on*, vol. 18, pp. 712-721, 1999.
- [70] R. Chandrashekhara, R. H. Mohiaddin, and D. Rueckert, "Cardiac motion tracking in tagged MR images using a 4D B-spline motion model and nonrigid image registration," in *Biomedical Imaging: Nano to Macro, 2004. IEEE International Symposium on*, 2004, pp. 468-471 Vol. 1.
- [71] E. Oubel, C. Tobon-Gomez, A. O. Hero, and A. F. Frangi, "Myocardial Motion Estimation in Tagged MR Sequences by Using α MI-Based Non Rigid Registration," in *Medical Image Computing and Computer-Assisted Intervention – MICCAI 2005*. vol. 3750, J. Duncan and G. Gerig, Eds., ed: Springer Berlin Heidelberg, 2005, pp. 271-278.
- [72] E. Oubel, A. F. Frangi, and A. O. Hero, "Complex wavelets for registration of tagged MRI sequences," in *Biomedical Imaging: Nano to Macro, 2006. 3rd IEEE International Symposium on*, 2006, pp. 622-625.
- [73] E. Oubel, M. De Craene, M. Gazzola, A. O. Hero, and A. F. Frangi, "Multiview registration of cardiac tagging MRI images," in *Biomedical Imaging: From Nano to Macro, 2007. ISBI 2007. 4th IEEE International Symposium on*, 2007, pp. 388-391.
- [74] S. Wenzhe, Z. Xiahai, W. Haiyan, S. Duckett, D. V. N. Luong, C. Tobon-Gomez, T. KaiPin, P. J. Edwards, K. S. Rhode, R. S. Razavi, S. Ourselin, and D. Rueckert, "A Comprehensive Cardiac Motion Estimation Framework Using Both Untagged and 3-D Tagged MR Images Based on Nonrigid Registration," *Medical Imaging, IEEE Transactions on*, vol. 31, pp. 1263-1275, 2012.
- [75] Z. Qian, D. Metaxas, and L. Axel, "A Learning Framework for the Automatic and Accurate Segmentation of Cardiac Tagged MRI Images," in *Computer Vision for Biomedical Image Applications*. vol. 3765, Y. Liu, T. Jiang, and C. Zhang, Eds., ed: Springer Berlin Heidelberg, 2005, pp. 93-102.
- [76] M. A. Guttman, J. L. Prince, and E. R. McVeigh, "Tag and contour detection in tagged MR images of the left ventricle," *Medical Imaging, IEEE Transactions on*, vol. 13, pp. 74-88, 1994.
- [77] T. Manglik, L. Axel, W. Pai, D. Kim, P. Dugal, A. Montillo, and Z. Qian, "Use of bandpass Gabor filters for enhancing blood-myocardium contrast and filling-in tags in tagged MR images," *Proc of Int'l Society for Mag. Res. In Med*, p. 1793, 2004.
- [78] J. Milles, A. van Susteren, T. Arts, P. Clarysse, P. Croisille, and I. E. Magnin, "Automatic 2D segmentation of the left ventricle in tagged cardiac MRI using motion information," in *Biomedical Imaging: Nano to Macro, 2004. IEEE International Symposium on*, 2004, pp. 153-156 Vol. 1.
- [79] O. Camara, E. Oubel, G. Piella, S. Balocco, M. Craene, and A. Frangi, "Multi-sequence Registration of Cine, Tagged and Delay-Enhancement MRI with Shift Correction and Steerable Pyramid-Based Detagging," in *Functional Imaging and Modeling of the Heart*. vol. 5528, N. Ayache, H. Delingette, and M. Sermesant, Eds., ed: Springer Berlin Heidelberg, 2009, pp. 330-338.
- [80] X. Huang, Z. Li, and D. Metaxas, "Learning Coupled Prior Shape and Appearance Models for Segmentation," in *Medical Image Computing and Computer-Assisted Intervention – MICCAI 2004*. vol. 3216, C. Barillot, D. Haynor, and P. Hellier, Eds., ed: Springer Berlin Heidelberg, 2004, pp. 60-69.
- [81] P. Lilly, J. Jenkins, and P. Bourdillon, "Automatic contour definition on left ventriculograms by image evidence and a multiple template-based model," *Medical Imaging, IEEE Transactions on*, vol. 8, pp. 173-185, 1989.

- [82] F. Vincent, P. Clarysse, P. Croisille, and I. E. Magnin, "An elasticity-based region model and its application to the estimation of the heart deformation in tagged MRI," in *Image Processing, 2000. Proceedings. 2000 International Conference on*, 2000, pp. 629-632.
- [83] Q. Zhen, H. Rui, D. Metaxas, and L. Axel, "A NOVEL TAG REMOVAL TECHNIQUE FOR TAGGED CARDIAC MRI AND ITS APPLICATIONS," in *Biomedical Imaging: From Nano to Macro, 2007. ISBI 2007. 4th IEEE International Symposium on*, 2007, pp. 364-367.
- [84] H. Rui, V. Pavlovic, and D. N. Metaxas, "A graphical model framework for coupling MRFs and deformable models," in *Computer Vision and Pattern Recognition, 2004. CVPR 2004. Proceedings of the 2004 IEEE Computer Society Conference on*, 2004, pp. II-739-II-746 Vol.2.
- [85] T. S. Yoo, M. J. Ackerman, W. E. Lorensen, W. Schroeder, V. Chalana, S. Aylward, D. Metaxas, and R. Whitaker, "Engineering and algorithm design for an image processing Api: a technical report on ITK--the Insight Toolkit," *Studies in health technology and informatics*, vol. 85, pp. 586-592, 2002.
- [86] D. Barbosa, "3D Cardiac strain estimation based on non-rigid registration: optimization for in-vivo application," ESAT, Katholieke Universiteit Leuven, 2009.
- [87] F. Maes, A. Collignon, D. Vandermeulen, G. Marchal, and P. Suetens, "Multimodality image registration by maximization of mutual information," *Medical Imaging, IEEE Transactions on*, vol. 16, pp. 187-198, 1997.
- [88] A. Elen, H. F. Choi, D. Loeckx, H. Gao, P. Claus, P. Suetens, F. Maes, and J. D'hooge, "Three-dimensional cardiac strain estimation using spatio-temporal elastic registration of ultrasound images: A feasibility study," *Medical Imaging, IEEE Transactions on*, vol. 27, pp. 1580-1591, 2008.
- [89] H.-m. Chen and P. K. Varshney, "Mutual information-based CT-MR brain image registration using generalized partial volume joint histogram estimation," *Medical Imaging, IEEE Transactions on*, vol. 22, pp. 1111-1119, 2003.
- [90] D. Mattes, D. R. Haynor, H. Vesselle, T. K. Lewellen, and W. Eubank, "PET-CT image registration in the chest using free-form deformations," *Medical Imaging, IEEE Transactions on*, vol. 22, pp. 120-128, 2003.
- [91] J. P. Pluim, J. A. Maintz, and M. A. Viergever, "Image registration by maximization of combined mutual information and gradient information," in *Medical Image Computing and Computer-Assisted Intervention--MICCAI 2000*, 2000, pp. 452-461.
- [92] S. Klein, M. Staring, K. Murphy, M. A. Viergever, and J. P. Pluim, "Elastix: a toolbox for intensity-based medical image registration," *IEEE transactions on medical imaging*, vol. 29, pp. 196-205, 2010.
- [93] S. Klein, M. Staring, and J. P. Pluim, "Evaluation of optimization methods for nonrigid medical image registration using mutual information and B-splines," *Image Processing, IEEE Transactions on*, vol. 16, pp. 2879-2890, 2007.
- [94] R. H. Byrd, P. Lu, J. Nocedal, and C. Zhu, "A limited memory algorithm for bound constrained optimization," *SIAM J. Sci. Comput.*, vol. 16, pp. 1190-1208, 1995.
- [95] B. Heyde, "Non-rigid image registration for the assessment of myocardial deformation from 3D echocardiography (in press)," KULeuven, 2013.
- [96] B. Heyde, R. Jasaityte, D. Barbosa, V. Robesyn, S. Bouchez, P. Wouters, F. Maes, P. Claus, and J. D'Hooge, "Elastic image registration versus speckle tracking for

- 2D myocardial motion estimation: a direct comparison in-vivo," *Medical Imaging, IEEE Transactions on*, vol. PP, pp. 1-1, 2012.
- [97] S. Lankton and A. Tannenbaum, "Localizing region-based active contours," *Image Processing, IEEE Transactions on*, vol. 17, pp. 2029-2039, 2008.
- [98] T. Chen, J. Babb, P. Kellman, L. Axel, and D. Kim, "Semiautomated segmentation of myocardial contours for fast strain analysis in cine displacement-encoded MRI," *Medical Imaging, IEEE Transactions on*, vol. 27, pp. 1084-1094, 2008.
- [99] O. Bernard, D. Friboulet, P. Thévenaz, and M. Unser, "Variational B-spline level-set: a linear filtering approach for fast deformable model evolution," *Image Processing, IEEE Transactions on*, vol. 18, pp. 1179-1191, 2009.
- [100] T. F. Chan and L. A. Vese, "Active contours without edges," *Image Processing, IEEE Transactions on*, vol. 10, pp. 266-277, 2001.
- [101] D. Barbosa, "Automated Assessment Of Cardiac Morphology And Function: An Integrated B-spline Framework For Real-time Segmentation And Tracking Of The Left Ventricle," Faculty of Medicine, KULeuven and Faculty of Electrical Engineering, INSA Lyon, 2013.
- [102] S. Queirós, "Fast Fully Automatic Myocardial Segmentation in 4D cine Cardiac Magnetic Resonance datasets," Master Degree, Departamento de Electrónica Industrial, Universidade do Minho, 2013.
- [103] X. H. Ren and J. Q. Bai, "Research Based on Template Matching Technologys Sandbox Sand Body CT Image Processing Methods," *Applied Mechanics and Materials*, vol. 385, pp. 1488-1494, 2013.
- [104] C. Ciofalo, M. Fradkin, B. Mory, G. Hautvast, and M. Breeuwer, "Automatic myocardium segmentation in late-enhancement MRI," in *Biomedical Imaging: From Nano to Macro, 2008. ISBI 2008. 5th IEEE International Symposium on*, 2008, pp. 225-228.
- [105] P. Radau, Y. Lu, K. Connelly, G. Paul, A. Dick, and G. Wright, "Evaluation framework for algorithms segmenting short axis cardiac MRI," *MIDAS J.—Cardiac MR Left Ventricle Segmentation Challenge*, 2009.
- [106] I. Ben Ayed, H.-m. Chen, K. Punithakumar, I. Ross, and S. Li, "Max-flow segmentation of the left ventricle by recovering subject-specific distributions via a bound of the Bhattacharyya measure," *Medical image analysis*, vol. 16, pp. 87-100, 2012.
- [107] J. D'hooge, A. Heimdal, F. Jamal, T. Kukulski, B. Bijmens, F. Rademakers, L. Hatle, P. Suetens, and G. Sutherland, "Regional strain and strain rate measurements by cardiac ultrasound: principles, implementation and limitations," *European Journal of Echocardiography*, vol. 1, pp. 154-170, 2000.
- [108] C. C. Moore, E. R. McVeigh, and E. A. Zerhouni, "Quantitative tagged magnetic resonance imaging of the normal human left ventricle," *Topics in magnetic resonance imaging: TMRI*, vol. 11, p. 359, 2000.
- [109] L. E. Malvern, *Introduction to the mechanics of a continuous medium*: Prentice-Hall, 1969.
- [110] B. Heyde, S. Cygan, H. F. Choi, B. Lesniak-Plewinska, D. Barbosa, A. Elen, P. Claus, D. Loeckx, K. Kaluzynski, and J. D'hooge, "Regional cardiac motion and strain estimation in three-dimensional echocardiography: A validation study in thick-walled univentricular phantoms," *Ultrasonics, Ferroelectrics and Frequency Control, IEEE Transactions on*, vol. 59, pp. 668-682, 2012.
- [111] M. D. Cerqueira, N. J. Weissman, V. Dilsizian, A. K. Jacobs, S. Kaul, W. K. Laskey, D. J. Pennell, J. A. Rumberger, T. Ryan, and M. S. Verani, "Standardized

- myocardial segmentation and nomenclature for tomographic imaging of the heart a statement for healthcare professionals from the cardiac imaging committee of the Council on Clinical Cardiology of the American Heart Association," *Circulation*, vol. 105, pp. 539-542, 2002.
- [112] C. A. Cocosco, T. Netsch, J. S negas, D. Bystrov, W. J. Niessen, and M. A. Viergever, "Automatic cardiac region-of-interest computation in cine 3D structural MRI," in *International Congress Series*, 2004, pp. 1126-1131.
- [113] C. Constantinides, Y. Chenoune, E. Mousseaux, E. Roullot, and F. Frouin, "Automated heart localization for the segmentation of the ventricular cavities on cine magnetic resonance images," in *Computing in Cardiology, 2010*, 2010, pp. 911-914.
- [114] M. M. Hadhoud, M. I. Eladawy, and A. Farag, "Region of Interest Localization of Cardiac Structure from Cine MRI Images," in *Information Technology: New Generations (ITNG), 2012 Ninth International Conference on*, 2012, pp. 14-17.
- [115] M.-P. Jolly, "Automatic segmentation of the left ventricle in cardiac MR and CT images," *International Journal of Computer Vision*, vol. 70, pp. 151-163, 2006.
- [116] N. Otsu, "A threshold selection method from gray-level histograms," *Automatica*, vol. 11, pp. 23-27, 1975.
- [117] P. Morais, B. Heyde, D. Barbosa, S. Queir s, P. Claus, and J. D'hooge, "Cardiac Motion and Deformation Estimation from Tagged MRI Sequences Using a Temporal Coherent Image Registration Framework," in *Functional Imaging and Modeling of the Heart*. vol. 7945, S. Ourselin, D. Rueckert, and N. Smith, Eds., ed: Springer Berlin Heidelberg, 2013, pp. 316-324.
- [118] B. D. Rosen, M. Cushman, K. Nasir, D. A. Bluemke, T. Edvardsen, V. Fernandes, S. Lai, R. P. Tracy, and J. A. Lima, "Relationship Between C-Reactive Protein Levels and Regional Left Ventricular Function in Asymptomatic Individuals The Multi-Ethnic Study of Atherosclerosis," *Journal of the American College of Cardiology*, vol. 49, pp. 594-600, 2007.
- [119] C. Tobon-Gomez, M. De Craene, A. Dahl, S. Kapetanakis, G. Carr-White, A. Lutz, V. Rasche, P. Etyngier, S. Kozerke, and T. Schaeffter, "A multimodal database for the 1 st cardiac motion analysis challenge," in *Statistical Atlases and Computational Models of the Heart. Imaging and Modelling Challenges*, ed: Springer, 2012, pp. 33-44.

Appendix

10. Appendix I – Details about the automatic segmentation method

During the proposed segmentation technique, we use the 4th frame to delineate the LV contours. We can't use the 1st and 2nd frames due to the presence of tags inside the blood pool (Figure 10.1). In Figure 10.1, we can see that the 3rd frame has a small number of tags on the blood pool. Comparing the 3rd frame with the 4th frame, the last option appears to be more adequate, but with a small difference. It is important to mention that we can't use a frame in the middle of the cycle, due to the tag fading.

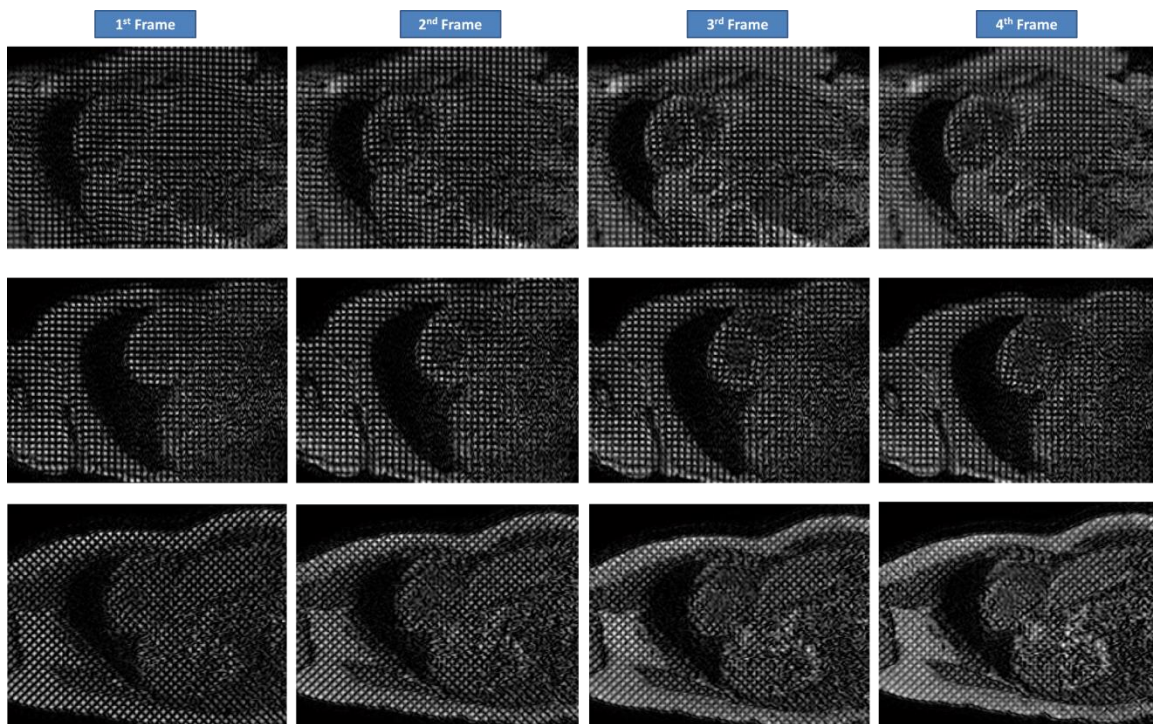


Figure 10.1 - Differences of tags inside the blood pool between the 1st frame and 4th frame.

The low pass filter used is computed using a polar image based on the spectrum image. A binarization based on the intensities will be performed. The DC component has the highest intensities on the image. To remove the DC component, we eliminate the first 10 lines of the polar image. Figure 10.2 shows the components that are removed (please note the red line). We can confirm that the range assumed (10 lines) only removes the DC component. As such, the binarization method will detect the tag positions as expected.

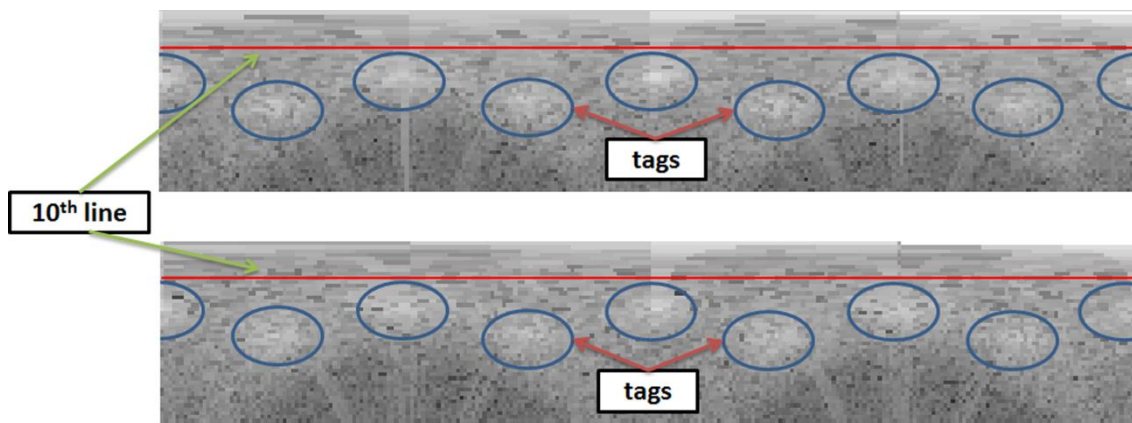


Figure 10.2 - Polar image used to compute the low pass filter.

In the current thesis, we suppress the tags using a combination of two filters. One filter will attenuate the high frequencies (low pass filter) and the second will remove the tag frequencies. In the proposed methodology, the second filter only removes the 1st harmonic of the tag frequencies. Figure 10.3 shows an alternative technique, where the 1st and 2nd harmonics of the tag frequencies are removed. Looking for the final result in each case (Figure 10.3), no significant difference was found.

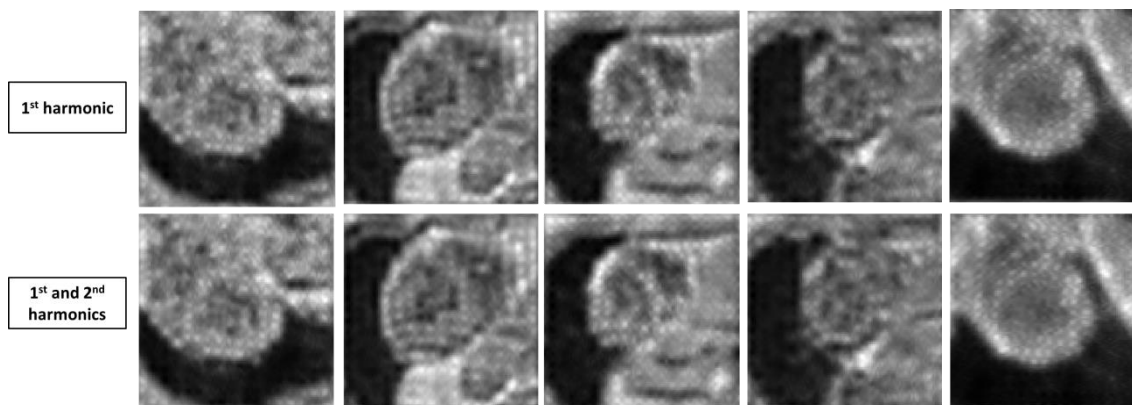


Figure 10.3 - Differences in the detagged image using a filter where the 1st harmonic of the tag frequencies is removed (first line) and the 1st and 2nd harmonics of the tags frequencies are removed.

11. Appendix II – Number of correction in the automatic contour

During this work, we refer that we are developing an automatic segmentation approach, but due the image properties and high variability of t-MRI a (semi-) automatic method is proposed. Typically, the physician can use this framework for automatic definition of the endocardial and epicardial contours, but in some situations due the previous assumptions (e.g., the heart should be positioned in the center of the image) a user input to correct the contours is used. Table 11.1 indicates the number of cases where user input was needed, and the number of cases where the apical was unsuccessful segmented. The mid and basal slice was always contoured with success.

Table 11.1 - Number of cases where the user input was used. We count the number of slices where the user need to change the first estimation of the LV center position (Center Correction), the number of slices where the user change one point in the automatic initialization method (One Point Correction) and the number of cases where the apical slice was not segmented (Apical Contour fail)

Center	N° of cases in Slices	Center Correction	One Point Corrected	Apical contour fail
1	120	5	2	3
2	129	5	10	9

12. Appendix III – LV tracking and segmentation results

Figure 12.1 shows the results of the registration framework for five different datasets. A virtual grid line was imposed on first frame, where the tags present a regular shape. This grid moves during the cardiac cycle based on the optimal transformation, following the tags.

In Figure 12.2 we illustrate some examples of the automatic contour (first column) and the propagation of the contour during the cardiac cycle. The segmentation delineated in first frame is propagated during the cycle based on the optimal transformation, using elastic registration.

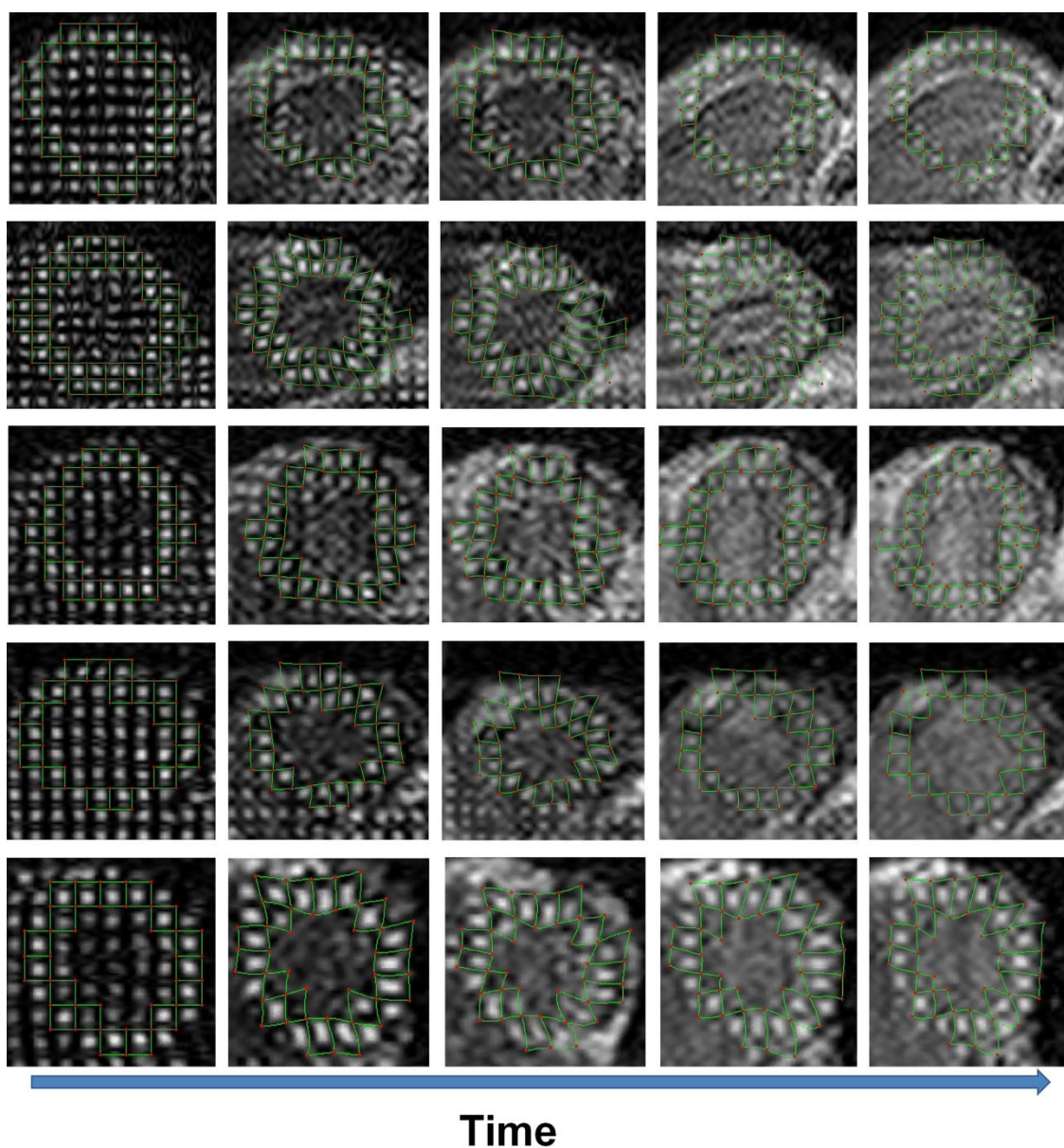


Figure 12.1 - Tag tracking result of the proposed sequential 2D+t methodology in five human datasets.

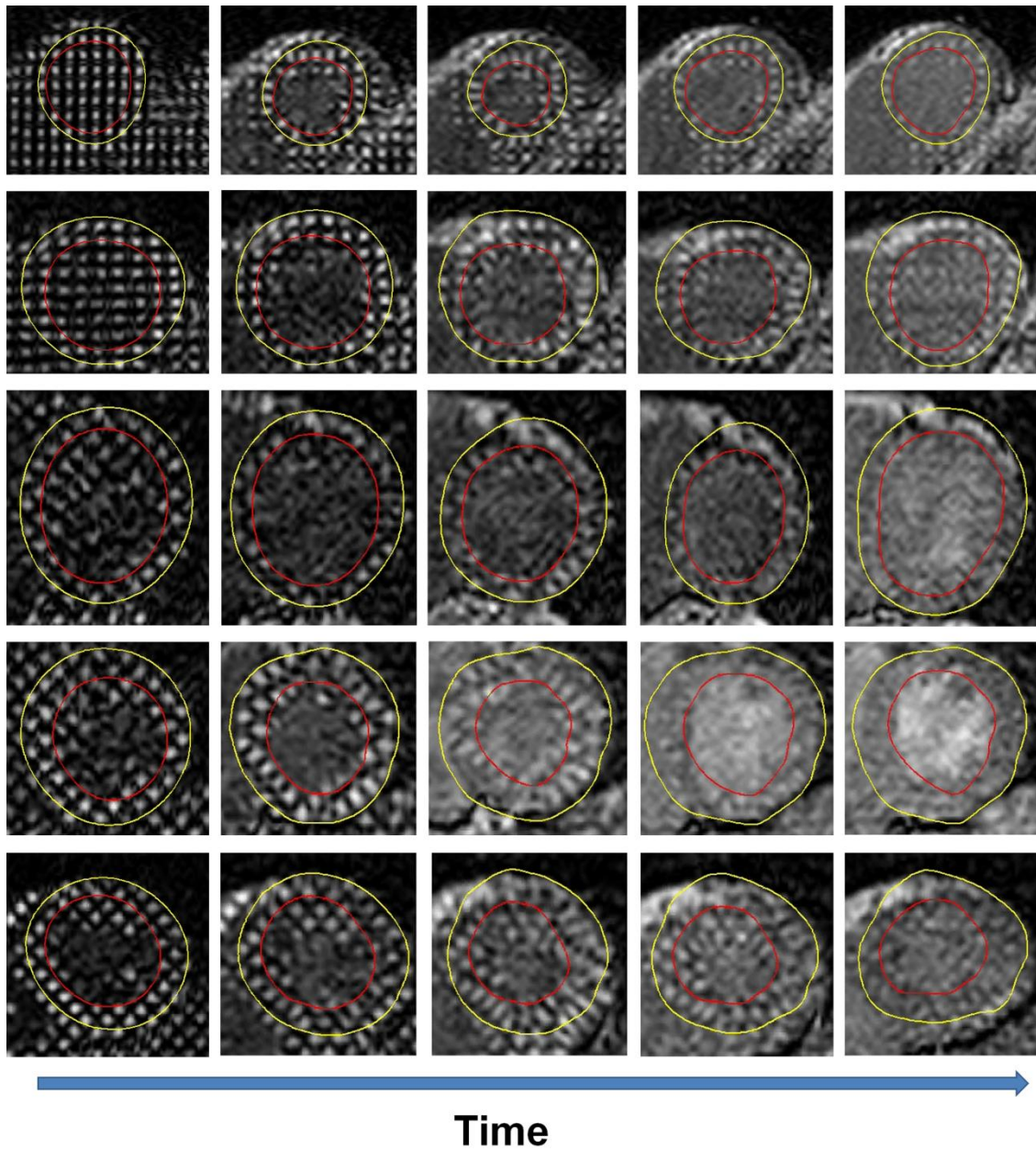


Figure 12.2 - (Semi) Automatic segmentation result. In the image we present five different situations, with images from different slices, obtained from different centers.

13. Appendix IV – Validation of the proposed sequential 2D+t FFD formulation using a published result

In this appendix, we illustrate a result (Figure 13.1) published by the author of the current master thesis in [117]. The differences between the sequential 2D and the sequential 2D+t approach, using and not a new adaptation of BE formulation (equation 4.10), are shown in the Figure 13.1. Please note, in this result the contours are defined manually.

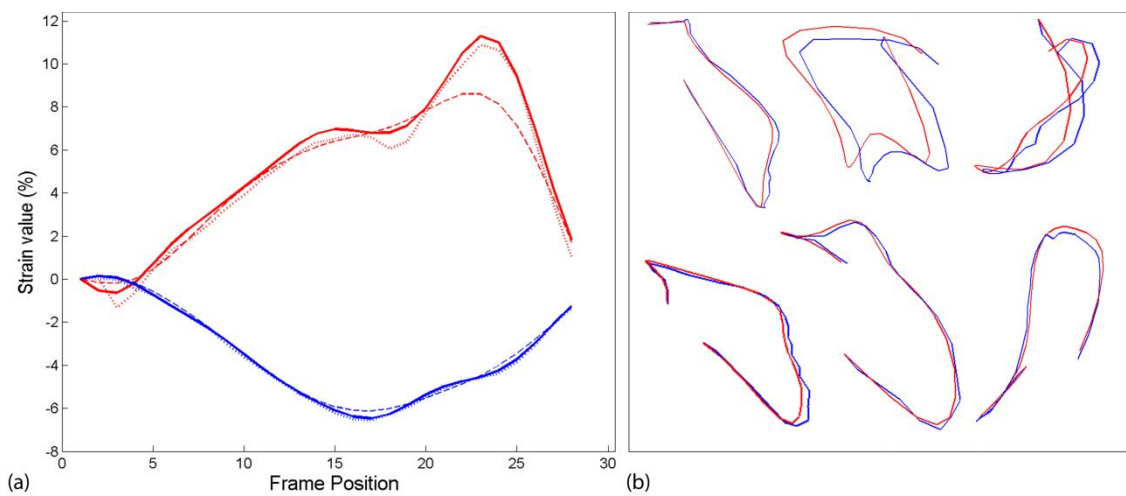


Figure 13.1 - (a) Global radial (red) and circumferential (blue) strain by using different methodologies: (solid line) the sequential 2D, (dotted line) sequential 2D+t using equation (4.7) and (dashed line) sequential 2D+t using equation (4.10) [proposed]. (b) Tag trajectory examples showing the difference between (blue) sequential 2D and (red) the sequential 2D+t approach [117].

14. Appendix V – Global strain curve obtained in proposed framework and in commercial software

Figure 14.1 presents some cases, selected randomly, available in the multi-center study with core-lab analysis. We intend to compare the global circumferential strain curve between the commercial software (red line) and the proposed 2D+t methodology (blue line).

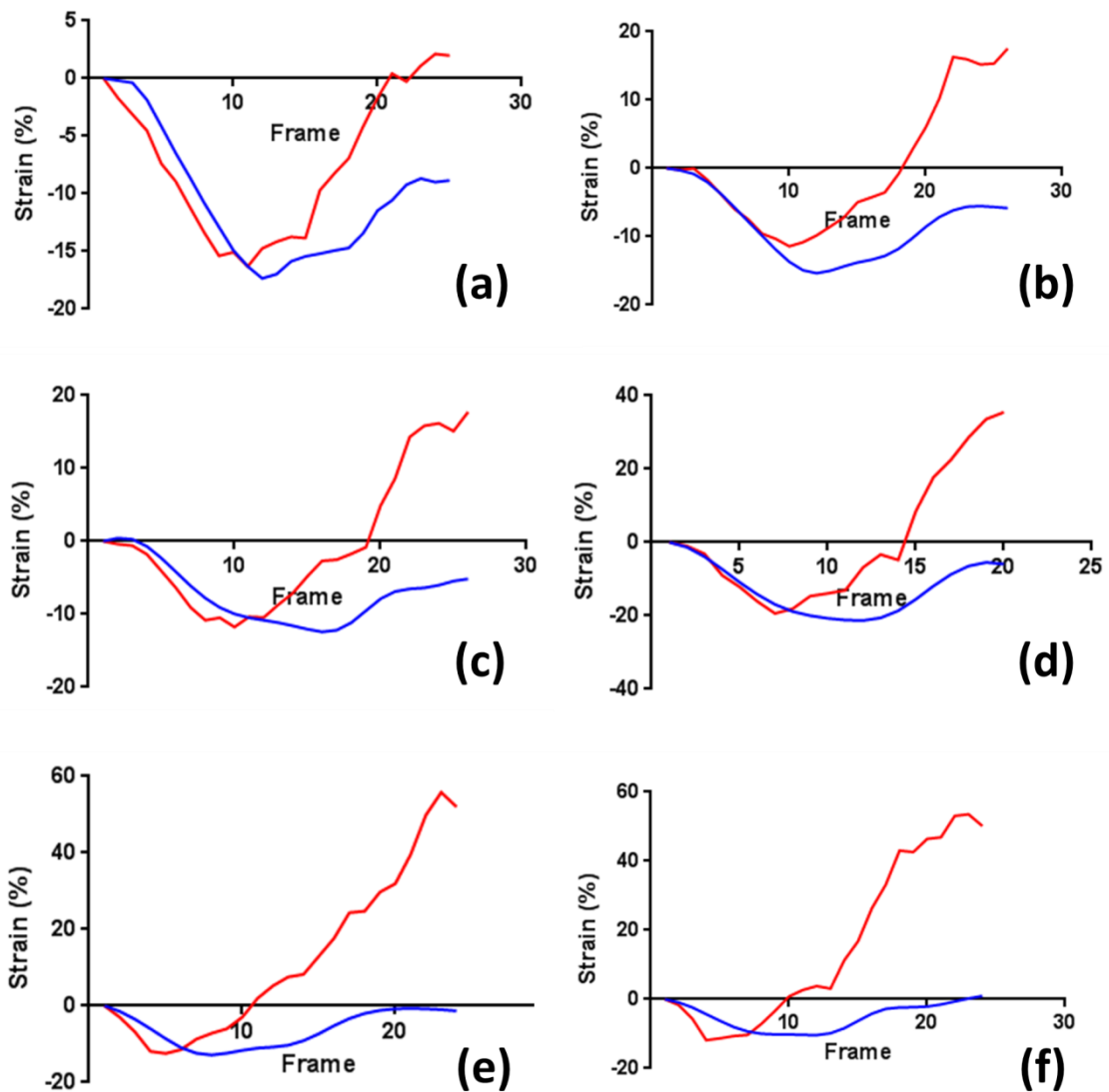


Figure 14.1 - Comparison between the software commercial (red line) with the proposed approach (blue line) in different cases.

15. Appendix VI – Results obtained in each slice for the proposed framework and commercial software

Table 15.1, Table 15.2 and Table 15.3 show the correlation coefficient and the limit of agreement for the apical, mid and base slice, respectively. All these results are based on the comparison between the strain peak value in the commercial software and the proposed methodology (NRR), based on registration.

At same time, we illustrate in Figure 15.1, Figure 15.2 and Figure 15.3 the linear regression and the Bland-Altman analysis for the best situation in each slice.

Table 15.1 - Results from Doppler CIP study, in terms of global circumferential strain in the apical slice, using different methodologies. *Statistically significant ($p < 0.05$) using a paired t-test

Study	Method	Correlation Coefficient (r)	Bland-Altman Analysis	
			Bias	LOA ($\mu \pm 1.96\sigma$)
1	Sequential 2D	0.389	3.247*	[-6.146;12.641]
2	Sequential 2D+t ($\sigma_t = 1$)	0.446	2.686*	[-5.929;11.302]
3	Sequential 2D+t ($\sigma_t = 2$)	0.436	2.631*	[-5.884;11.146]
4	Sequential 2D+t ($\sigma_t = 3$)	0.460	2.009*	[-6.978;10.995]

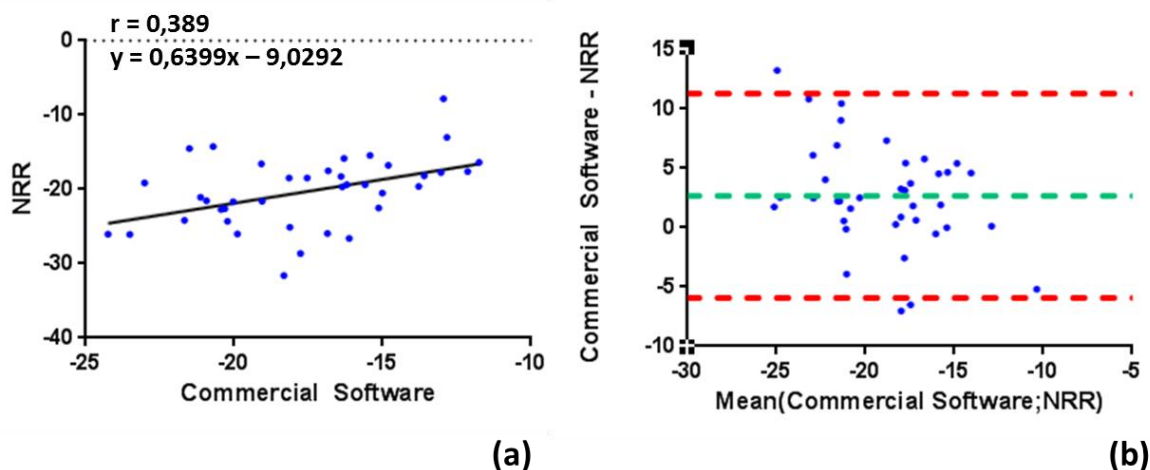


Figure 15.1 - (a) Linear regression, and (b) Bland-Altman Analysis in terms of global circumferential strain for the apical slice.

Table 15.2 - Results from Doppler CIP study, in terms of global circumferential strain in the mid slice, using different methodologies. *Statistically significant ($p < 0.05$) using a paired t-test

Study	Method	Correlation Coefficient (r)	Bland-Altman Analysis	
			Bias	LOA ($\mu \pm 1.96\sigma$)
1	Sequential 2D	0.536	2.485*	[-5.287;10.257]
2	Sequential 2D+t ($\sigma_t = 1$)	0.531	2.119*	[-6.008;10.247]
3	Sequential 2D+t ($\sigma_t = 2$)	0.530	1.867*	[-6.196;9.297]
4	Sequential 2D+t ($\sigma_t = 3$)	0.525	1.494*	[-6.526;9.515]

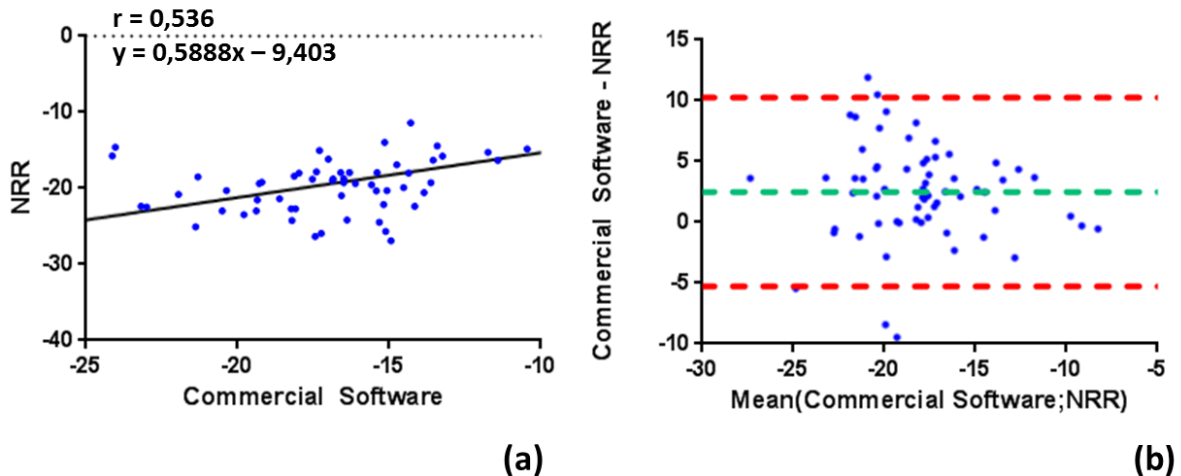


Figure 15.2 - (a) Linear regression, and (b) Bland-Altman Analysis in terms of global circumferential strain for the mid slice.

Table 15.3 - Results from Doppler CIP study, in terms of global circumferential strain in the base slice, using different methodologies. *Statistically significant ($p < 0.05$) using a paired t-test

Study	Method	Correlation Coefficient (r)	Bland-Altman Analysis	
			Bias	LOA ($\mu \pm 1.96\sigma$)
1	Sequential 2D	0.755	2.217*	[-2.780;7.234]
2	Sequential 2D+t ($\sigma_t = 1$)	0.739	1.374*	[-3.783;6.531]
3	Sequential 2D+t ($\sigma_t = 2$)	0.725	1.099*	[-4.285;6.483]
4	Sequential 2D+t ($\sigma_t = 3$)	0.725	0.447	[-4.905;5.798]

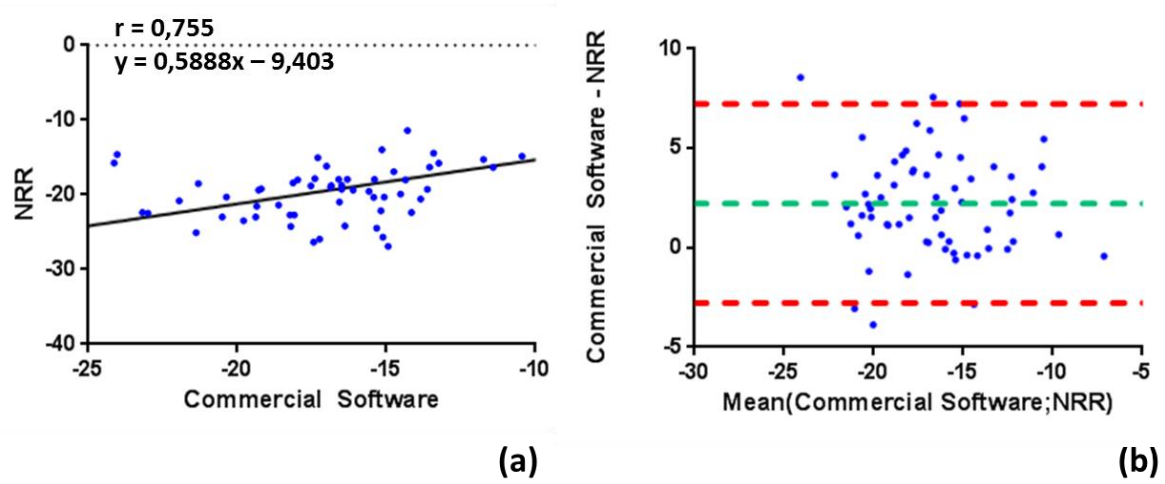


Figure 15.3 - (a) Linear regression, and (b) Bland-Altman Analysis in terms of global circumferential strain for the basal slice.

16. Appendix VII – Validation of the proposed framework using the commercial software results as ground truth

Table 16.1 and Table 16.2 present the correlation and the Bland-Altman analysis in the global and segmental strain, respectively. Since the *diagnosoft-HARP* has a clinical validation, we are using these results as a “ground truth”. The ES moment will be defined using the *HARP* results. The circumferential peak value will be used to determine the ES frame. Then, we compute in the proposed approach the circumferential strain at the ES defined by the *diagnosoft-HARP* results.

Table 16.1 - Results from Doppler CIP study, in terms of global circumferential strain, using different methodologies. *Statistically significant ($p < 0.05$) using a paired t-test

Study	Method	Correlation	Bland-Altman Analysis	
		Coefficient (r)	Bias	LOA ($\mu \pm 1.96\sigma$)
1	Sequential 2D	0.632	-0.001	[-6.319;6.312]
2	Sequential 2D+t ($\sigma_t = 1$)	0.691	-0.501	[-6.525;5.523]
3	Sequential 2D+t ($\sigma_t = 2$)	0.691	-0.629*	[-6.655;5.398]
4	Sequential 2D+t ($\sigma_t = 3$)	0.674	-0.904*	[-7.173;5.364]

Table 16.2 - Results from Doppler CIP study, in terms of segmental circumferential strain, using different methodologies. *Statistically significant ($p < 0.05$) using a paired t-test

Study	Method	Correlation	Bland-Altman Analysis	
		Coefficient (r)	Bias	LOA ($\mu \pm 1.96\sigma$)
1	Sequential 2D	0.408	-0.052	[-12.706;12.603]
2	Sequential 2D+t ($\sigma_t = 1$)	0.394	-0.594	[-12.960;11.772]
3	Sequential 2D+t ($\sigma_t = 2$)	0.392	-0.635	[-13.27;12.000]
4	Sequential 2D+t ($\sigma_t = 3$)	0.388	-1.02*	[-13.829;11.789]

Figure 16.1 and Figure 16.2 show the linear regression between the commercial software and the proposed approach (NRR) and the Bland-Altman analysis for the best result present in the Table 16.1 (sequential 2D+t with $\sigma_t = 1$) and Table 16.2 (sequential 2D).

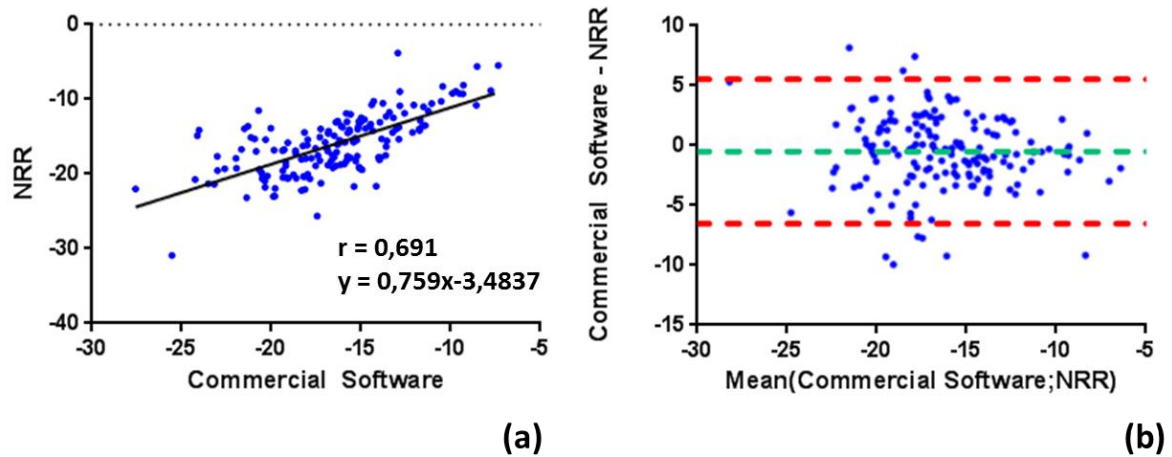


Figure 16.1 - (a) Linear regression, and (b) Bland-Altman Analysis in terms of global circumferential strain.

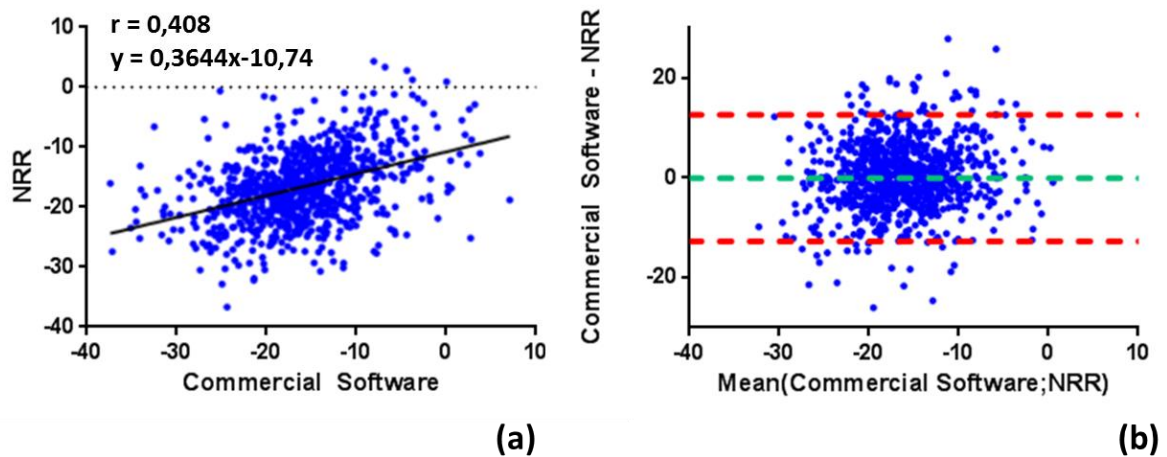


Figure 16.2- (a) Linear regression, and (b) Bland-Altman Analysis in terms of segmental circumferential strain.

17. Appendix VIII – Details about the ANOVA table

In this appendix, we prove the assumptions of the ANOVA table. Using the Levene’s test, we obtain a significant value of 0.335 which proves the homogeneity of the sample, assuming $p < 0.05$. The Table 17.1 shows the study of the residual values, where it is possible to see a mean residual value equal to zero. The Kolmogorov-Smirnov test demonstrates the normality of the study, with a significance of 0.2 (assuming $p < 0.05$). In the end, Figure 17.1 presents a boxplot with the distribution of the samples. In this boxplot, outlier’s points are not detected.

Table 17.1 - Residual values table

		Statistic	Standard Error
Residual values	Mean Value	0	0.023
	95 % Confidence Interval for mean	Lower Bound -0.0451	
		Upper Bound 0.0451	
	5% Trimmed Mean	-0.005	
	Median	-0.0309	
	Variance	1.001	
	Standard deviation	1.0003	
	Maximum	-2.41	
	Minimum	2.41	
	Range	4.82	
Interquartile Range	1.36		

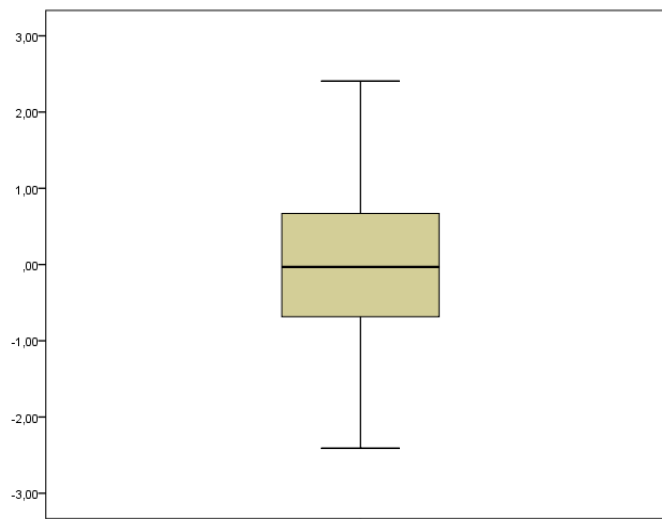


Figure 17.1 - Boxplot of samples distribution.